Deorbiting Algorithms Development for CubeSats using Propulsion and Sails

José Emmanuel Morales Robles

School of Mechanical Engineering

University of Leeds

A thesis submitted for the degree of

Doctor of Philosophy

23rd February 2020

To my parents.

Acknowledgements

PhD has been the journey of my life, one that would have been impossible without the people that surrounded and were always there for me. In first place, my primary supervisor, Dr. Jongrae Kim, not only he offered me invaluable technical guidance through this journey, but he also kept encouraging and motivating me to keep moving forward during the hardest times, and didn't stop believing in me even when I did. He was always patient and kind to me, and also very supportive. To him my endless gratitude. I would also like to thank Professor Robert Richardson, who also offered invaluable guidance during my work, always giving very insightful feedback to my manuscripts. Last but not least, Dr. Mark Wilson also offered me with very helpful feedback and encouragement during each of the yearly reviews.

Then, there is the Mexican community in Leeds, who brought a little bit of my country to me. It would be unfair to try to name everyone because I'm afraid I could forget someone, but at the same time it is impossible not to mention my dearest friend, Christian, and his beautiful wife and daughter, Vicky and Lucy. They were there for me in my darkest hours, and I'm not sure I would have been able to keep my sanity without their wise advice and warm talks.

My office mates, which kindly invited me to join their football team. Very specially I would like to thank Asmawi, we both went through rough times and tried to help each other whenever one of us was about to lose hope. I'm sure he will succeed in his own journey.

Finally, a big thank you to my family, my parents and siblings, for their support, their advice and for always caring for me.

Abstract

CubeSats are becoming increasingly popular within the scientific and commercial community, as they provide relatively cheap and quick access to space. However, as their launching rates increase rapidly, the concern that they may have a negative impact in the space debris problem also increases. This calls for the development of novel deorbiting technologies for CubeSats. In a response to this need, this thesis presents two new attitude controllers and deorbiting algorithms, which enable ionic thrusters, as well as drag sails, in order to accelerate CubeSat orbital disposal. These algorithms are designed with nanosatellites capabilities in mind, requiring minimum attitude determination and control. Their efficacy is demonstrated through numerical models in all cases.

In the first approach, a geomagnetic field tracker controller is presented. This controller aligns the thrusting carrying axis of the satellite with the local magnetic field vector. The only sensors and actuators required are magnetometers and magnetorquers respectively. A suitable deorbiting algorithm is also presented, which is activated once the CubeSat is tracking the geomagnetic vector. This algorithm determines the portions of the orbit in which thrust must be applied, and it only requires a model of Earth's magnetic field. This approach is simulated with ionic thrusters, obtaining deorbiting rates between 0.35 km/day and 50 km/day, depending on the type of engine used. Proof of stability is provided through Floquet theory, while robustness analysis is executed through Monte Carlo simulations. This approach has advantages such as minimum sensing and actuating requirements, and it doesn't require

movable parts nor deployables, minimizing the probability of failures in orbit.

In the second approach, a gyroless spin-stabilization controller is proposed. This algorithm fixes the thrusting carrying axis of the CubeSat in the inertial frame. Just as the first approach, this controller only requires magnetometers and magnetorquers. Once the satellite is stabilized, an orbit sampling algorithm is introduced. This algorithm is able to determine the portions of the orbit where to apply thrust, using only Global Positioning System inputs. This approach is simulated with electrospray thrusters, achieving deorbiting rates in the order of 45 km/day. Stability analysis is provided through Lyapunov theory, while Monte Carlo simulations are used to prove the robustness of the algorithm.

The attitude stabilization phases of both approaches are very flexible, in that they can work with a variety of thrusters, as well as non propulsive technologies. Dragsails are often proposed as means for deorbiting CubeSats, however, there is a gap in the literature when it comes to their stabilization in orbit. Therefore, the efficacy of these stabilization approaches when used in conjunction with drag sails is analysed. In the case of the geomagnetic field tracking algorithm, deorbiting rates in the order of 19 km/day are attained. In the case of the gyroless spin-stabilization algorithm, deorbiting times of up to 12.5 km/day are achieved.

These algorithms provide convenient means for CubeSat deorbiting, contributing to space debris mitigation efforts. They require minimum hardware and software capabilities, and because of this the probability of failures is low, and they provide excellent deorbiting rates.

Abbreviations

$\mathbf{A}$	Linear dynamics matrix
A	Cross sectional area
a	Orbital semi-major axis
$\mathbf{A_{CL}}$	Closed loop linear dynamics matrix
a_h	Perpendicular perturbing acceleration
a_θ	Cross-radial perturbing acceleration
a_r	Radial perturbing acceleration
$\mathbf{A_r}$	Reduced linear dynamics matrix
a_x, a_y, a_z	Acceleration components in the ECI frame
$\mathbf{B}$	Control matrix
$\mathbf{b}$	Geomagnetic field vector
$\hat{\mathbf{b}}$	Normalized magnetic vector
BC	Ballistic coefficient
$\mathbf{b^{lvlh}}$	Geomagnetic vector in LVLH coordinates
$\mathbf{B_r}$	Reduced control matrix
B_r, B_θ, B_ϕ	Components of the Earth's magnetic field in spherical coordinates
$\mathbf{C}$	Direction cosine matrix
C_D	Drag coefficient
e	Orbital eccentricity
e_1, e_2, e_3	Components of the rotation vector in quaternion notation
$\mathbf{F_D}$	Drag force
$\mathbf{F_e}$	Electrodynamic force

g_n^m, h_n^m	Gaussian coefficients provided by IAGA
h	Specific angular momentum
$\mathbf{i}$	Unit vector toward the x direction of the body frame
i	Orbital inclination
I_{ave}	Average current
$\mathbf{J}$	Inertia tensor
J_2	Zonal harmonic coefficient
$\mathbf{K_r}$	Reduced gains matrix
$\boldsymbol{\ell}$	Unit vector along the electrodynamic tether
M	Mean anomaly
$\mathbf{m}$	Magnetic dipole vector
m	Mass
$\mathbf{m_{ctrl}}$	Control magnetic dipole vector
n	Mean motion
P_n^m	Schmidt quasi-normalized associate Legendre function
$\mathbf{q}$	Quaternion vector
q_0, q_1, q_2, q_3	Components of the quaternion vector
r	Orbital radius
R_e	Mean radius of the Earth
V	Lyapunov function
$\mathbf{v_{rel}}$	Velocity vector relative to the atmosphere
$\mathbf{x}$	State vector
$\mathbf{x_r}$	Reduced state vector
x, y, z	Components of the ECI frame

θ	Latitude
θ_c	Colatitude
λ_F	Eigenvalues of $\mathbf{F}$
λ_Φ	Eigenvalues of the state transition matrix
μ	Earth's gravitational constant
ν	True anomaly
ρ	Mass density of the fluid
τ	Torque
τ_{des}	Desired torque
$\boldsymbol{\tau_{tot}}$	External torques vector
Φ	State transition matrix
ϕ	Angle of rotation in quaternion notation, or Longitude
Ω	Longitude of the ascending node
$\boldsymbol{\omega}$	Angular velocity expressed in the body frame
ω	Argument of periapsis

Contents

List of Figures

Chapter 1

Introduction

1.1 Background

Space based infrastructure plays a vital role in every aspect of our lives. From telecommunications, weather forecast, climate change monitoring, navigation, and a myriad of security, science and engineering applications, all rely on various services provided by spacecraft orbiting the limited near Earth space. It is therefore of extreme importance that Earth orbit is used in a sustainable way.

In the past two decades, a specific class of nanosatellites, called CubeSats, has revolutionized and democratized access to space. CubeSat platform provides cheaper and shorter development cycles and cheaper launch costs, due to the relative simplicity in their design and reduced volume and mass. It has allowed universities and start-ups to become space exploration actors, a role before only attainable to government agencies, specially those of a few developed countries. CubeSat has the potential to open the door for new space technologies and applications.

The advantages offered by CubeSats, in the other hand, come at the cost of worsening the risks in the near Earth orbit usages. The number of launches has been consistently increasing, and it is projected that this trend will continue. Because of their limitations, however, they usually lack means for active deorbiting. This is one of the major concerns as this could cause them to become space junk, increasing the risk of collision to launch vehicles and other satellites. Some orbital

ranges, especially Low Earth Orbit (LEO), are becoming highly populated. A plethora of modern services are inseparable from space infrastructure. A disruption to this infrastructure has potentially catastrophic consequences on our daily life.

It is of vital importance that deorbiting technologies for CubeSats are deployed, in order to allow for their sustainable use in space. There are already efforts to tackle this problem, with the main concepts being: deorbiting sails, deorbiting inflatables and electric tethers. These approaches have, however, serious design disadvantages. More effective, efficient and practical deorbiting methods are yet to be developed.

This research aims to explore new deorbiting technologies, such as ionic propulsion and improved approaches with drag sails. This includes the development of attitude stabilization algorithms that allow for the application of thrust in an efficient way, as well as to stabilize a drag sail attitude. These attitude control approaches need to take into consideration the limitations in terms of sensing and actuation faced by CubeSats.

This work is motivated by the space debris problem and the risk that it represents for space exploration in general. Space debris poses a hazard not only for Earth orbiting spacecraft, but also for interplanetary flights. The development of effective deorbiting systems is of extreme importance for a sustainable use of orbital resources. This research intends to contribute to the efforts to keep Earth orbits clean.

1.2 Aim and Objectives

1.2.1 Aim

The main aim of this research is to design robust, reliable and cost effective CubeSat deorbit systems. Based in electromagnetic attitude actuators, ionic thrusters, and drag sails, the systems must provide a seamless and easy to integrate architecture compliant with the CubeSat standard.

1.2.2 Objectives

- Perform an extensive literature review in order to better understand the space debris problem, the role that CubeSats play in it, as well as the current approaches to tackle this issue.
- Explore ionic propulsion technologies as part of the CubeSat deorbiting conversation. Understand their principles of operation, their designs and potential areas of improvement.
- Develop efficient attitude control systems that enable the application of ionic propulsion technology to the deorbit problem. These control systems must take into account the limitations in hardware and software faced by CubeSats.
- Develop deorbiting algorithms, to complement the aforementioned attitude control systems, in order to achieve the final goal of deorbiting the CubeSat. These algorithms must also take into accounts the hardware and software limitations of CubeSats.
- Explore the application of the developed attitude control systems to non-ionic type system. More specifically, explore the possibility of its application with drag sails. Study the advantages and disadvantages of this approach.
- Prove the stability and robustness of the deorbiting systems. Floquet theory as well as Lyapunov theorems can be used to prove stability. Robustness can be proved by means of Monte Carlo simulations.

1.3 Contribution to the Field

The main contributions of this research are as follows:

- A geomagnetic field tracking controller is developed. It uses minimal attitude information. This is an improvement over existing controllers and makes it ideal for CubeSat applications. The stability and robustness of this controller is provided through Floquet analysis and Monte Carlo simulations

respectively. Results show the reliability of this new approach. A deorbiting algorithm is developed to work in conjunction with the field tracking controller. It also uses minimal attitude information, requiring only magnetometers for its operation.

- A gyroless spin-stabilization controller is developed, using no attitude information. It is proven that this controller is effective as a first stage of a deorbiting operation. The stability and robustness of this controller is provided through Lyapunov theory and Monte Carlo simulations respectively, giving great confidence on the effectiveness of this approach. A deorbiting algorithm is developed to work in conjunction with the gyroless spin-stabilization controller. The algorithm is in perfect alignment with the features of CubeSats. It requires no attitude information. It only requires Global Positioning System (GPS) receiver data.

- The effectiveness of both attitude controllers is demonstrated in the drag sail scenario. It is shown that these attitude controllers are effective in the sail case. The magnetic field tracking algorithm is the one showing more potential for this scenario.

1.4 Thesis Structure

This thesis is organized as follows. Chapter 2 provides a literature review relevant to CubeSats, the space debris problem, as well as current mitigation approaches, finalizing with a review of common attitude control systems used in CubeSats. Chapter 3 gives an introduction to the mathematical background related to this work, together with a summary of the environmental models used for the numerical simulations presented here. In Chapter 4, the geomagnetic field tracker control system and respective deorbiting algorithm are discussed in detail. The gyroless spin-stabilization algorithm and sampling deorbiting algorithm are presented in Chapter 5. Chapter 6 is devoted to the application of these attitude stabilization controllers to the drag sail scenario. Finally, conclusions as well as future work are discussed in Chapter 7.

1.5 Thesis Outputs

The following journal publications were a result of the research presented in this work.

(a) Jose E. Morales, Jongrae Kim and Robert R. Richardson, *Geomagnetic Field Tracker for Deorbiting a CubeSat Using Electric Thrusters*, Journal of Guidance, Control and Dynamics, Vol. 42, Number 5, 2019, pp. 1157-1165.

(b) Jose E. Morales, Jongrae Kim and Robert R. Richardson, *Gyroless Spin-Stabilization Controller and Deorbiting Algorithm for CubeSats*, International Journal of Aeronautical and Space Sciences, 2019. Under review.

(c) Jose E. Morales, Jongrae Kim and Robert R. Richardson, *Attitude Stabilization for CubeSats for Deorbiting with Drag Sails*. In process.

Chapter 2

Literature Review

2.1 Introduction

In this chapter a literature survey is provided on a variety of aspects in order to gain an insight to the state of the art of the problem, which is the necessity and alternatives for CubeSat deorbiting. First, we put in context the CubeSat - and more generally, nanosatellites - popularity growth, and how, despite of all their benefits, this growth represents a challenge from a space debris perspective. Second, current proposed approaches that attempt to tackle this problem, and their virtues as well as areas of improvement are discussed. Third, taking into consideration these areas of improvement, we explore a new research area with the potential to provide a solution that surpasses the features of the existing approaches, namely, electric propulsion. The features and principles of operation of five main types of electric propulsion will be reviewed. Fourth, an overview of available methods for Attitude Determination and Control Systems (ADCS) for CubeSats is explored, in order to put in context the challenge that the utilization of thrusters poses. Finally, a summary and discussion section is given.

2.2 CubeSats and Space Debris

Interest in CubeSat development has been continuously growing since the standard configuration was first introduced in the late 90's. The standard is defined

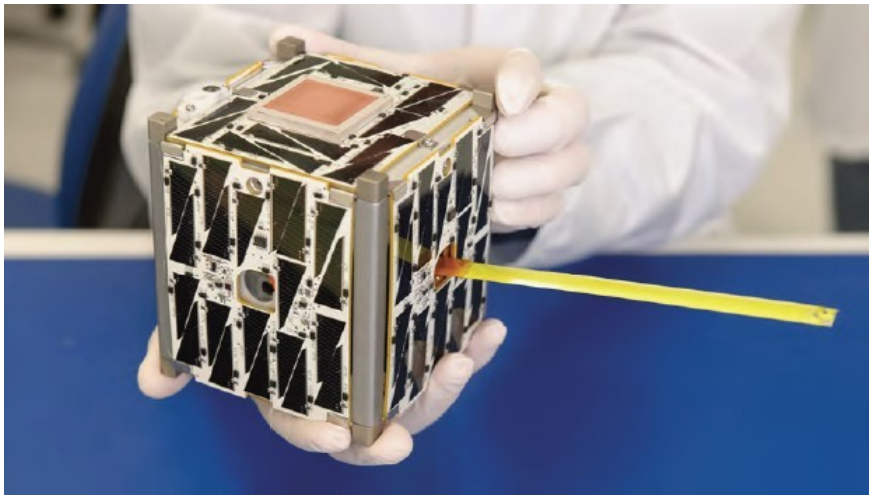

Figure 2.1: 1U CubeSat. www.nasa.gov

and maintained by the CubeSat Organization. A CubeSat unit (U) has a cubic shape of 10 cm by side, and up to 1.3kg of mass. These units can be assembled together to form satellites of 2U, 3U and beyond. Figure 2.1 shows a typical 1U CubeSat. Its geometrical shape can be seen along with the structural subsystem, solar panels, which are a standard component of these satellites, and antenna. This type of satellite was conceived for didactic purposes. They were first intended as a tool to teach the full design and development cycle of a satellite to engineering students within one semester. However, as technology evolved, and component miniaturization continued, it was soon recognized that they had a great potential for applications with scientific and technological value. Some of these applications include: Earth observation (Nascetti *et al.*, 2015), telecommunications (Hodges *et al.*, 2015), astronomy (Park *et al.*, 2016), and technology demonstrations in general, assuming the payload can fit in the CubeSat form factor.

Just to mention some examples, in the field of Earth observation, Nascetti et al. (Nascetti *et al.*, 2015) propose an S-band patch antenna being compatible with any standard CubeSat structure. Meanwhile, in their work, Hodges et al. (Hodges *et al.*, 2015) propose two deployable reflectarray antennas in order to be used for telecommunications purposes in the K/Ka and X bands. Negligible stowed volume and modest mass make this application ideal for CubeSats. Also, in the field of

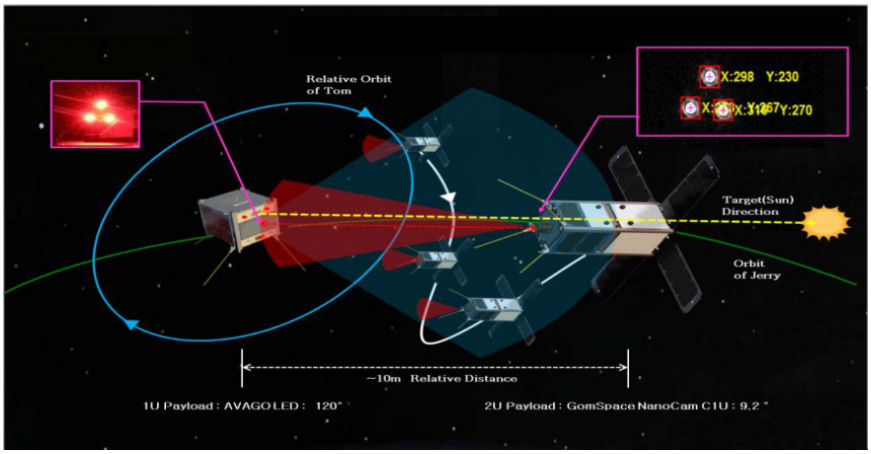

Figure 2.2: Concept of Inertial Alignment System (Park *et al.*, 2016)

astronomy, Park et al. (Park *et al.*, 2016) propose a virtual telescope system which main component blocks are two CubeSats, named Tom and Jerry. This concept is depicted in Fig. 2.2.

The success of this form factor has been such, that CubeSats are no longer confined just lo LEO. Now there is a growing interest in using them for interplanetary missions. NASA's Insight mission, included two 6U CubeSats, Mars Cube One (MarCO), with the task to relay lander data from Mars in real time (Hodges *et al.*, 2016), with the mission resulting in a success. See Fig. 2.3 for a visualization of the actual MarCO spacecraft.

According to available records, around 700 CubeSats had been deployed into orbit as of July 2017 (David, 2017). There are already some operational CubeSat constellations such as Flock 1 from Planet Labs and Spire. Flock 1 is intended for real time Earth imagery and consists of 28 operational CubeSats (Kramer, 2019). Spire is intended to improve the weather forecast with measurements of Earth's atmosphere and is comprised of 60 3U CubeSats (Kramer, 2019). If those were not enough, some mega-constellations of these nanosatellites are being conceived. Such is the case of Starlink, an initiative of the private company SpaceX, which intends to deploy 12,000 small satellites in order to provide satellite internet to the whole globe (Messier, 2017). While this constellation is not composed of CubeSats, it makes use of small satellites, and still shows how important it is to manage such

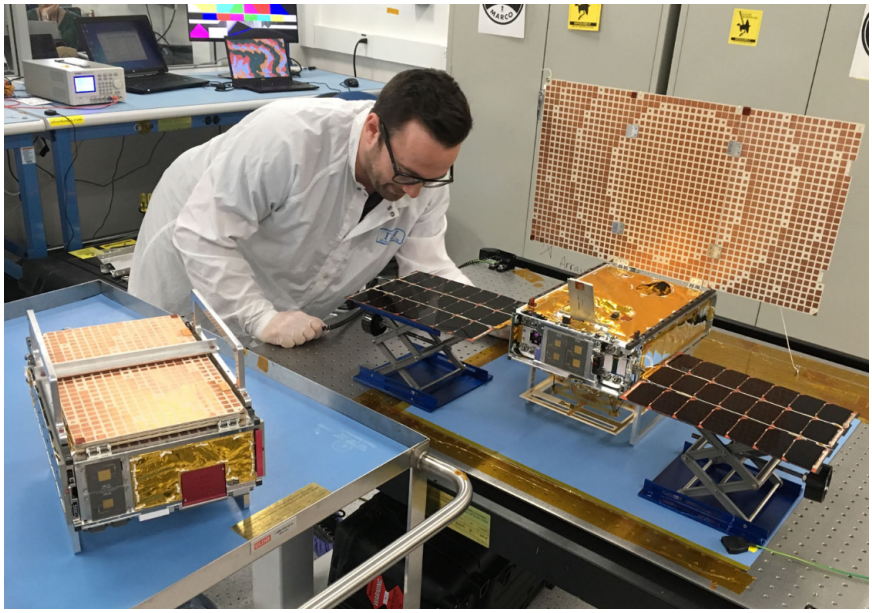

Figure 2.3: Mars Cube One MarCO in development. www.nasa.gov

vast swarms of spacecrafts. Also, there is OneWeb, mainly managed by Airbus, which aims to deploy 2,700 nanosatellites also for telecommunications purposes (Messier, 2017). Figure 2.4 depicts an artistic impression of the planned OneWeb constellation. This trend suggests that this standard came to stay, and that the number of units in orbit is going to grow exponentially.

This progress is coming at a cost, as most nanosatellites are not equipped with any deorbiting system. Depending on the orbital altitude at which it is deployed, it can take a CubeSat from a few months to even centuries before re-entering Earth's atmosphere (Klinkrad, 2004). There exists the concern that the CubeSat boom can have a negative impact in the space junk problem, an issue recognized by the scientific community. A total of 24,000 objects the size of a baseball or larger were estimated to be in Earth orbit as of 2011 (Chen, 2011), most of them without any remaining means of orbital control, which increases the chances of collisions in space. An example of such collisions already occurred in 2009, when the American communications satellite Iridium 33 and the retired Russian Kosmos-251 crashed. This resulted in the destruction of both spacecraft and the generation of a large amount of orbital debris (Oltrogge & Leveque, 2011). There have been other in-

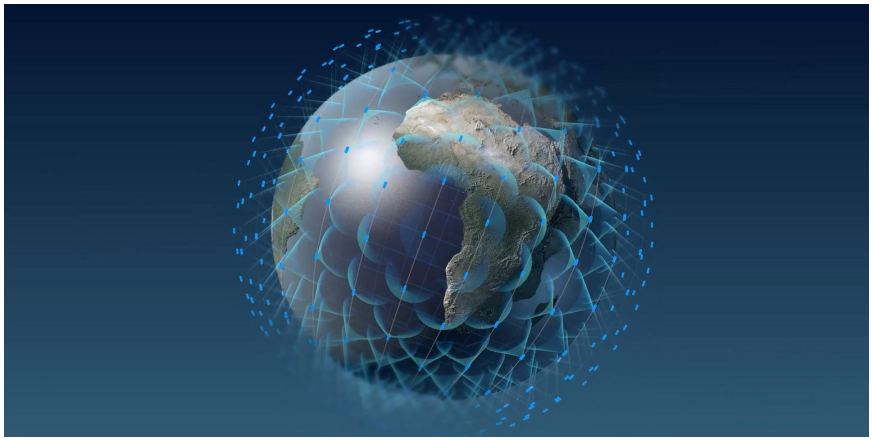

Figure 2.4: OneWeb constellation. www.airbus.com

stances were collisions were not accidental but deliberate. Such was the case of China's military test in 2007. In that case, weather forecast satellite Fengyun 1c was intentionally targeted by a missile. This action created thousands of pieces of debris. Furthermore, the Kessler syndrome predicts that a critical density of objects in LEO could be reached, and that collisions between them could cause a cascade of impacts, that would eventually create enough debris to render some orbital ranges unusable within this century (Kessler & Cour-Palais, 1978). In response to this risk, guidelines dictated by the Inter-Agency Space Debris Coordination Committee establish that any artificial satellite must be deorbited or moved to a disposal orbit within 25 years of the end of their mission. These considerations make clear the necessity to develop technologies that enable CubeSats to be deorbited in a timely manner.

2.3 Existing Deorbiting Approaches

In a response to the CubeSat deorbiting necessity, several approaches have been explored in the past few years, aimed to shorten the time a CubeSat spends in orbit after its operational mission finishes. There are four main technologies as follows: deorbiting sails, deorbiting inflatables, electrodynamic tethers, and more recently, electric thrusters. Note that these are approaches that include the deorbiting ac-

tuators within the satellite to be deorbited. There are also research on approaches which would involve the dispatch of a second satellite, which would rendezvous with the CubeSat to be deorbited, and somehow catch it - spears, nets, tugs and other means have been proposed - and bring it back to Earth's atmosphere. This second approach is beyond the scope of this thesis.

2.3.1 Sails

Deorbit sails rely on aerodynamic drag force augmentation, and the drag force is given by

$$\mathbf{F_D} = -\frac{1}{2}\rho\|\mathbf{v_{rel}}\|\mathbf{v_{rel}}C_D A \tag{2.1}$$

where $\mathbf{F_D}$ is the drag force in Newtons (N), ρ is the mass density of the fluid in kg/m^3, $\mathbf{v_{rel}}$ is the velocity vector relative to the atmosphere in m/s, $\|\cdot\|$ is the 2-norm of the vector, C_D is the drag coefficient of the object, and A is the cross sectional area of the object in m^2.

Some of the most notable missions and concepts in the field of deorbiting sails for CubeSats are as follows. NanoSail-D and NanoSail-D2, which were missions developed by NASA (Johnson *et al.*, 2011), DeorbitSail by University of Surrey, CubeSail, by Surrey Space Centre, AEOLDOS, a deorbit system developed by University of Glasgow, ERNST, a 6U CubeSat, and CNUSAIL-1, a South Korean experiment. NanoSail-D launch was unsuccessful. However, its ground spare, NanoSail-D2, shown in Fig. 2.5 made it into orbit in November 2010. The experiment was successful, since the satellite was deorbited from an initial altitude of 650 km in just 240 days. This process would have taken around 25 years if left to natural orbital decay. University of Surrey's DeorbitSail satellite (Stohlman *et al.*, 2014) was launched in 2015. However, this experiment was unsuccessful, since the sail failed to deploy, this being a typical example of how difficult deploying actuators in space can be. Another study case is CubeSail, currently being designed at the Surrey Space Centre. The main design issue the team is tackling is the folding of the sail and the deployment mechanism (Adeli & Lappas, 2010). The CubeSat is yet to be launched into orbit. The University of Glasgow developed the Aerodynamic End of Life Deorbit System for CubeSats (AEOLDOS) concept (Harkness *et al.*, 2014). To the best knowledge of the author, such system has yet

Figure 2.5: NanoSail-D2 ground deployment test. www.nasa.gov

to be demonstrated in space. ERNST, a collaboration between the Ernst-Mach Institut and the High Peerformance Space Structure Systems is a good example of the challenges posed by drag sails. In their work (Reichenbach *et al.*, 2018), they present several design iterations for the deployment mechanism, but no suitable alternative is found. Finally, CNUSAIL-1 was a CubeSat experiment intended to demonstrate drag sail technology (Yoo *et al.*, 2016). The satellite was launched and deployed successfully in January 2018. However, according to communication with the authors, the communications link was lost shortly after. It is not clear weather the satellite was able to deploy its drag sail.

There are some instances where the solar sail isn't intended to deorbit the satellite, but still demonstrates the potential of this technology. Such is the case of the work presented by Steyn & Lappas (Steyn & Lappas, 2011). In this mission, a CubeSat equipped with a 5 m by 5 m solar sail is studied. It is considered to be in a Sun synchronous orbit and its stabilization is studied. This stabilization is intended by means of panel translation and magnetic torquing. One of the main disadvantages of this concept, is that it requires Complementary Metal-Oxide Semiconductor (CMOS) cameras as attitude sensors. The paper concludes

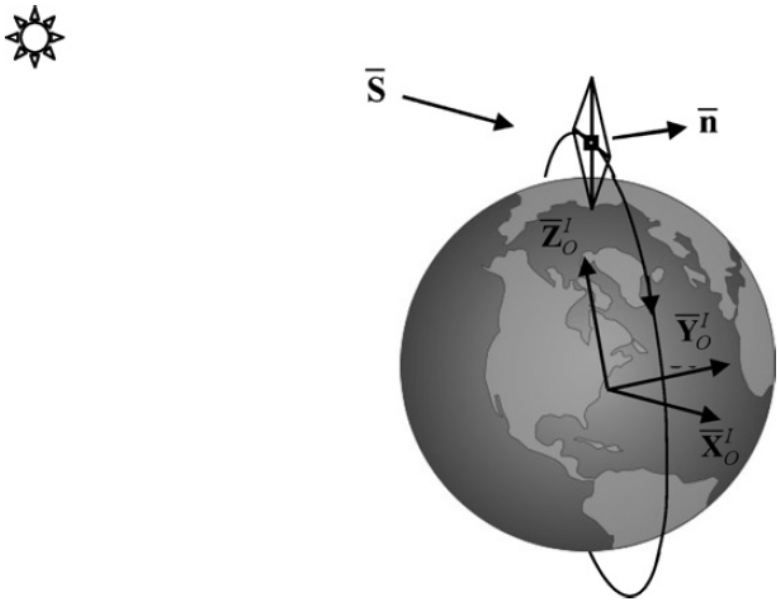

Figure 2.6: Sail navigation concept (Steyn & Lappas, 2011).

the attitude stabilization is possible. However, actual implementation in space seems not to have been carried out yet.

Finally there are also concepts using sails, but with the opposite purpose of propelling interplanetary, and even interstellar nanosatellites. Some of them have been already tested in space, such as LightSail-1 (Biddy & Svitek, 2012) and IKAROS (Tsuda *et al.*, 2013), shown in Fig. 2.7.

2.3.2 Inflatables

In the case of inflatable structures, the aim is to decrease the ballistic coefficient of the spacecraft. The ballistic coefficient, BC, of an object is given by the following formula:

$$BC = \frac{m}{C_D A} \tag{2.2}$$

where BC is in kg/m^2 and m is the mass of the object in kg.

The efficiency of different shapes of inflatable structures has also been the subject of study. For example, in their work, Maessen et al. (Maessen *et al.*,

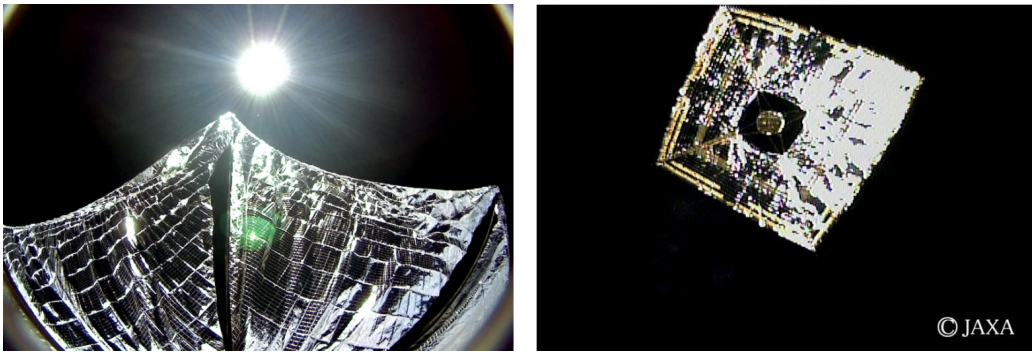

Figure 2.7: Images of LightSail-1 (left) and IKAROS (right) in space. www.planetary.org and global.jaxa.jp respectively

2007) experiment with different geometries, concluding that a pyramidal structure is optimal. With their system, they claim, a CubeSat could be deploy at an initial altitude of 900 km. In that case the satellite would still be deorbited within 25 years as suggested by guidelines. Nakasuka et al. (Nakasuka *et al.*, 2009) in the other hand, investigate the effectiveness of a spherical structure, and propose a system which is claimed to be effective at initial altitudes of up to 800 km. Lokcu and Ash (Lokcu & Ash, 2011) experimented with three different geometries, spherical, pyramidal and pillow shapes, claiming their system would be effective to deorbit CubeSats from an initial altitude of 900 km in a period of 30 years. Andrews et al. (Andrews *et al.*, 2011) propose a cone shaped system that besides deorbiting the nanosatellite, would also protect it during atmospheric re-entry, allowing payloads to be recovered as shown in Fig. 2.8. A similar concept is presented by Carandente & Savino (Carandente & Savino, 2014), proposing a conical inflatable that would also protect the payload during re-entry. A combination between inflatables and sails have also been proposed by Viquerat et al. (Viquerat *et al.*, 2014), for its InflateSail concept. In this experiment, an inflatable mast is complemented with a drag sail. In the last work they don't mention target orbits or deorbiting times, so the effectiveness of the system is not clear.

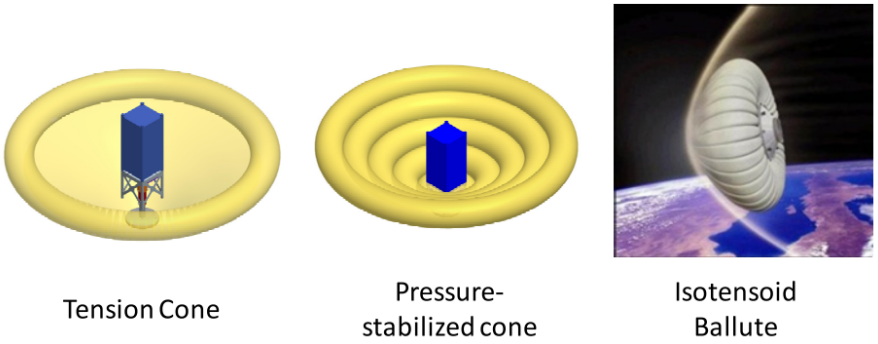

Figure 2.8: Different inflatable concepts. (Andrews *et al.*, 2011)

2.3.3 Electric Tethers

Tethers rely on the electrodynamic force created as a result of the interaction between a current carrying cable and the Earth's magnetic field. See Fig. 2.9 for a graphical description of the principle of operation. The generated electromagnetic force can be expressed as

$$\mathbf{F_e} = -I_{ave} L \mathbf{b} \times \boldsymbol{\ell} \tag{2.3}$$

where $\mathbf{F_e}$ is the electrodynamic force in Newtons (N), I_{ave} is the average current across the electrodynamic tether in Amperes (A), L is the length of the tether in m, $\mathbf{b}$ is the local geomagnetic field vector in Tesla (T), and $\boldsymbol{\ell}$ is the unit vector along the electrodynamic tether.

The concept of utilizing space tethers to accelerate spacecraft orbital decay has been investigated as early as the decade of the 90's. Authors like Cosmo & Lorenzini (Cosmo & Lorenzini, 1997), Lanoix et al. (Lanoix *et al.*, 2005), Forward et al. (Forward *et al.*, 1998), and more recently Sanmartin et al. (Sanmartin *et al.*, 2012) explore this technology applied to conventional sized spacecraft, including the Space Shuttle. In the latter case, however, the deorbiting is accomplished by means of momentum transfer between the Space Shuttle and the International Space Station, rather than through electromagnetic effects.

Hoyt et al. (Hoyt *et al.*, 2009) developed on the concept of the Terminator Tape, a tethered system that would enable CubeSats orbiting up to 1000 km to comply with space debris mitigation guidelines. No references to a mission using

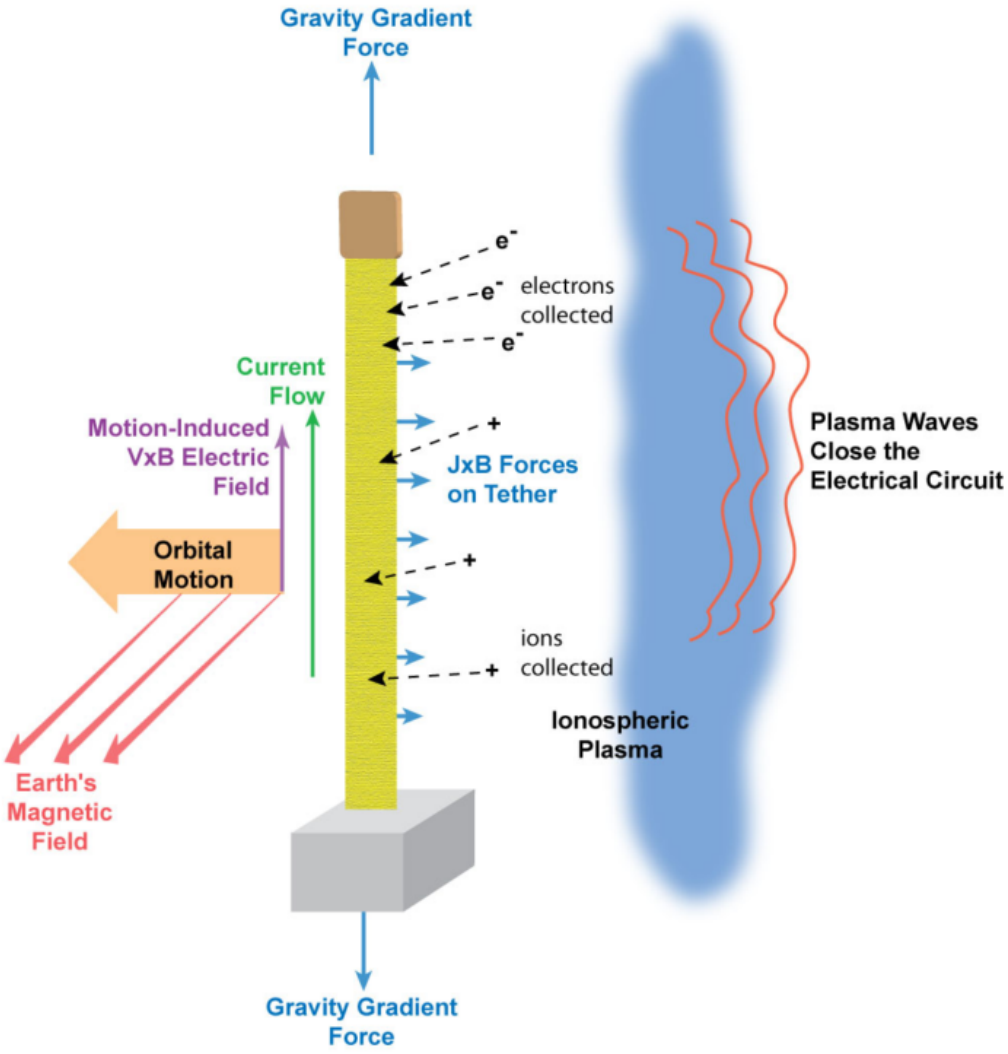

Figure 2.9: Physics of electrodynamic tether for deorbiting. (Hoyt *et al.*, 2009)

this technology have been found. Lanoix (Lanoix, 1999) and Lanoix et al. (Lanoix *et al.*, 2005) provide a detailed analysis of the dynamics of tethered satellites and its potential application to the deorbit of spacecraft larger than 100 kg. Their simulations suggest deorbiting times in the order of 20 days for equatorial orbits, as well as 100 days in the case of polar orbits, for an initial circular orbit of 1500 km of altitude.

In the specific field of CubeSats, the study by Voronka (Voronka *et al.*, 2005) claims that deorbit times of 25 years for CubeSats at an initial altitude of 1000 km can be attained deploying a 1 km long tether. Zhu & Zhong have proposed different control approaches to the deorbit problem with electrodynamic tethers. One of these approaches is an On-Off current scheme (Zhong & Zhu, 2014b), with which is claimed that a CubeSat would lose altitude at a rate of 100 km per 60 days. The second approach uses a finite receding horizon control (Zhong & Zhu, 2014a). In the latter case, the CubeSat tethered system would lose 100 km of altitude in 25 days.

There are also approaches that focus in the tether interaction with space plasma rather than the Earth's magnetic field, such is the case of the work by Janhunen (Janhunen, 2014) and Khurshid et al. (Khurshid *et al.*, 2014). Janhunen (Janhunen, 2014) claims that with this approach, a 5 km long plasma brake tether weighing 0.055 kg could produce a force of 0.43 mN, enough to reduce the orbital altitude of a 260 kg object by 100 km over a year. One can see that this result is very promising when translating to the CubeSat field. In the other hand, Khurshid et al. (Khurshid *et al.*, 2014) present a concept where a 100 m long tether will be deployed from a CubeSat. This approach is known as plasma brake experiment, and will be tested in the Aalto-1 CubeSat mission, which has already been launched, but the decommissioning phase has not yet been executed. The results of this experiment will help to further understand the efficiency of the plasma brake concept and its applications to the CubeSat deorbiting problem.

2.4 Propulsion for CubeSats

All of the three discussed approaches require the deployment of actuators in space, making the system prone to failures. They also require significant volumes for stor-

Table 2.1: Electric Engine Types

Engine	Thrust mN	Power W	Fuel	Mass g	Specific Impulse s
Electrospray	1.8	25	Ionic Salt	1400	1500
Micro Pulsed Plasma Thruster	0.04	2	Teflon	280	600
Hall Effect Thruster	0.1	3	Xenon	1000	1500
CubeSat Ambipolar Thruster (Sheehan *et al.*, 2015)	0.5	50	Xenon	<1000	400
Micro Cathode Arc Thruster (Keidar, 2016)	0.05	0.1	Solid fuel	200	2000

age of their respective actuators, and in some cases the storage of compressed gas. These are the major disadvantages of said approaches, reason why new alternatives are being investigated. One of the technologies with more potential in this area is propulsion, and more specifically, electric propulsion.

Up until now, most CubeSats have lacked any means of propulsion, and as a result, they don't have orbital manoeuvring capabilities. Amongst other things, this has prevented the development of efficient deorbiting systems for this class of satellites, and usually this process is left to natural orbital decay. While this method can be effective for CubeSats at an orbital altitude of 650 km or lower, for higher orbits it would take more than 25 years for the deorbiting to be completed.

In a response to this problem, much research has been performed in the field of electric propulsion. While there are different technologies for electric thrusters, the following ones are being developed for its application in CubeSats: Electrospray (Lozano & Martínez-sánchez, 2005), Micro Pulsed Plasma Thruster (Coletti *et al.*, 2011), Hall Effect Thruster (Dankanich *et al.*, 2013), CubeSat Ambipolar Thruster (Collard & Sheehan, 2016), and Micro Cathode Arc Thruster (Zhuang *et al.*, 2011).

Table 2.1 summarizes some of the main features for each particular type of electric engine, which provide an insight of the potential that this technology has for applications in the field of CubeSats.

Note that the mass of these engines is still somewhat prohibitive for their use

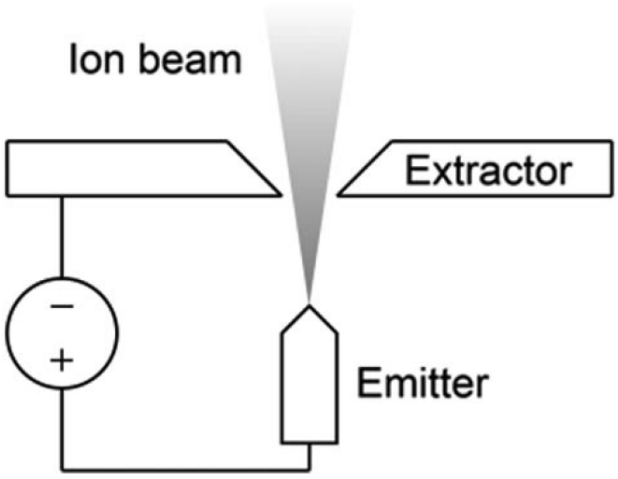

Figure 2.10: Electrospray single emitter (Mier-hicks & Lozano, 2017).

in 1U CubeSats, except in some unusual missions because little or no room would be left for the rest of the systems and payload. However, their integration in the popular 3U or larger configurations seems feasible.

These electric propulsion technologies open the possibility for nanosatellite orbital control, including the crucial phase of deorbiting. In the following subsections, the main features and working principles for each of these technologies are presented.

2.4.1 Electrospray

One of the recent developments in electric propulsion for CubeSats has been undergone in the Massachusetts Institute of Technology (Lozano *et al.*, 2015). They have introduced the concept of Ion Electrospray Propulsion System (iEPS) (Mier-hicks & Lozano, 2017). In this concept, emitters in shape of cones, known as Taylor cones and made of a porous substrate, are fed with ionic salts, which act as fuel. A high potential difference is then applied between the emitters and an extractor grid placed upstream them. This causes the generation of an ion beam that is expelled at high velocities, thus generating thrust. Fig. 2.10 shows a graphical representation of this process. The ionic salt is stored passively and is fed to the

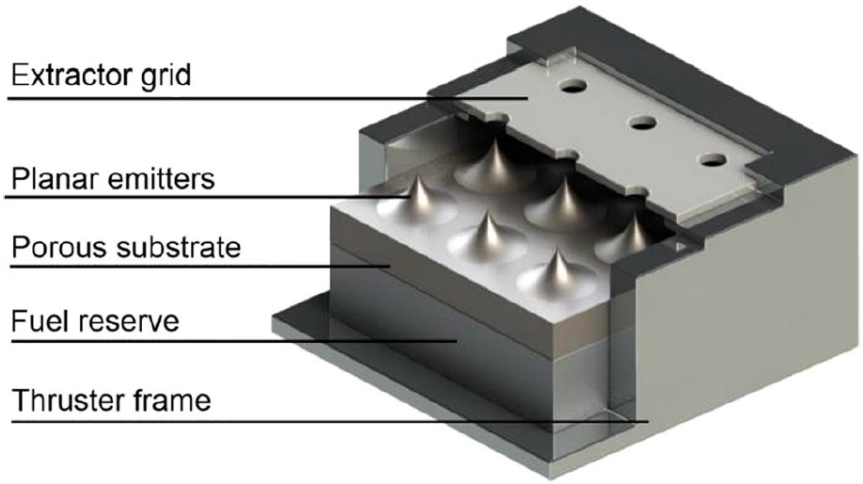

Figure 2.11: iEPS concept (Mier-hicks & Lozano, 2017).

emitters by means of capillarity effect. Fig. 2.11 depicts the components of an iEPS thruster.

Figure 2.12 shows an exploded view of the components of an iEPS emitter array (left), as well as a prototype emitter array and its relative size to a quarter coin for comparison (right). This helps to visualize the potential for the integration of this type of thrusters in CubeSat missions. Furthermore, Fig. 2.13 shows a prototype of an iEPS module board designed in a CubeSat factor, with the thrusters and the Power Processing Unit (PPU) already integrated.

Aspects of these thrusters such as its application to precise attitude control (Mier-hicks & Lozano, 2017), orbital life extension (Blandino *et al.*, 2016), its fabrication (Dandavino *et al.*, 2014), orbital maneuvers (Kolosa *et al.*, 2014) and general propulsive maneuvers (Courtney *et al.*, 2015b) have been discussed in literature. However, there exists a gap in this literature when it comes to their application to the deorbiting problem. One of the main aims of this thesis is to fill this gap and propose methods that enable this type of propulsion to be applied to the deorbiting phase of the missions.

Specific impulses for this type of thrusters is high, in the order of 1500 to 3000 s, and energy consumption in the order of 1 to 25 W (Courtney *et al.*, 2015b), allowing for a very efficient use of fuel and energy. Also, these engines are able to

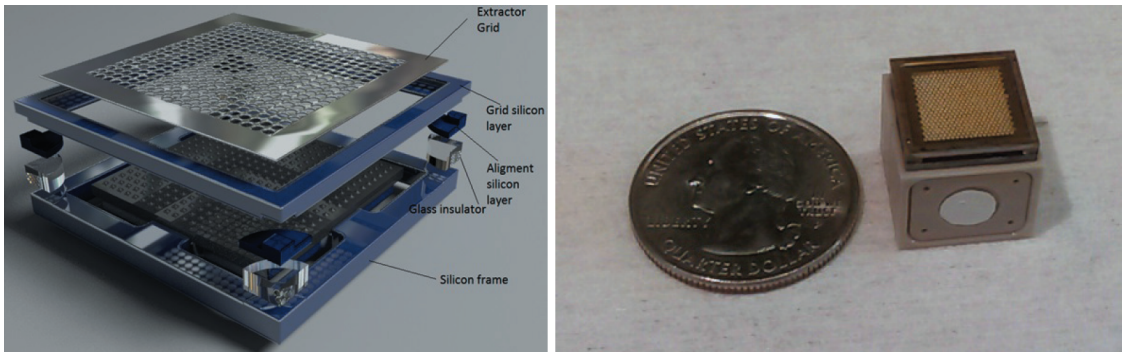

Figure 2.12: Left: Exploded view of the emitter to extractor packaging. Right: Fully packaged thruster including 480 emitter array. (Krejci *et al.*, 2015)

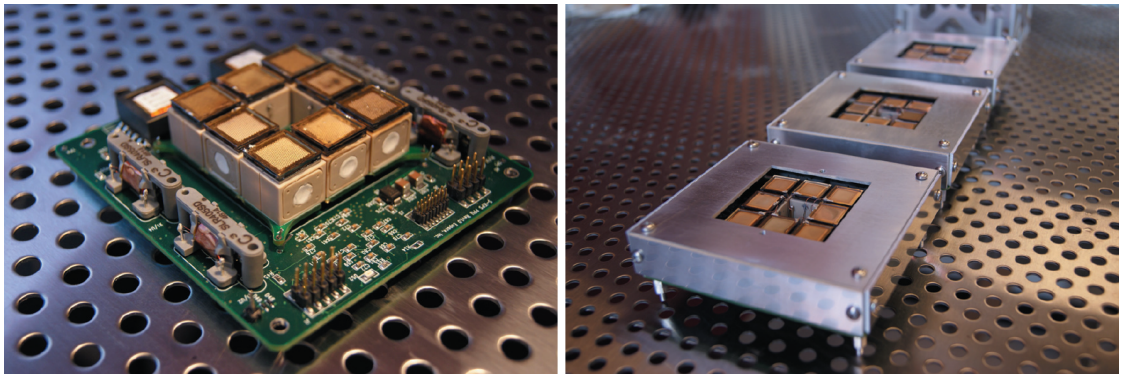

Figure 2.13: NASA MEP S-iEPS propulsion module featuring 8 thrusters and PPU, without (left) and with (right) protective enclosure for testing (Krejci *et al.*, 2015).

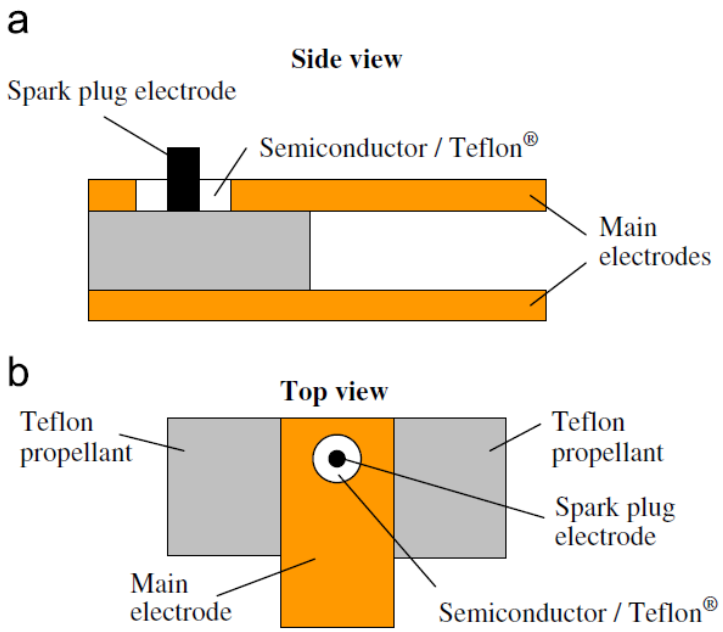

Figure 2.14: Conventional spark plug setup. a) side view and b) top view (Coletti *et al.*, 2011).

generate thrust in the order of tens of μN, or even mN when combining multiple chips (Courtney *et al.*, 2015a), which allow deorbiting times in the order of months or even weeks depending on the initial orbital altitude, as opposed to decades if left to natural orbital decay.

2.4.2 Micro Pulsed Plasma Thruster

Another promising technology that is being developed for its application in CubeSats, is the Micro Pulsed Plasma Thruster (μPPT). The schematic of this type of engine is shown in Fig. 2.14 (Coletti *et al.*, 2011), where it can be seen that the main components are the electrodes (anode and cathode), the propellant (Teflon) an the spark plug electrode.

A variation of this configuration is depicted in Fig. 2.15 (Krejci *et al.*, 2013), which consists of the same elements but in a coaxial configuration.

Figure 2.16 shows a physical prototype of a Micro Pulsed Plasma Thruster

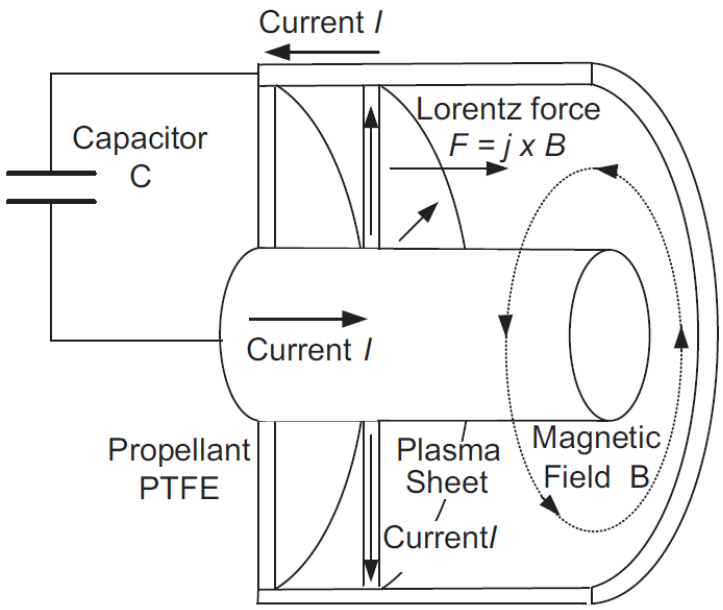

Figure 2.15: Simplified schematic of μPPTs (Krejci *et al.*, 2013).

developed by Clyde Space and Mars Space Ltd, which is already commercially available.

The principle of operation is as follows. A spark is generated by the spark plug electrode, which causes part of the Teflon propellant to be ablated, generating a cloud of plasma between the two main electrodes. A voltage is applied between the two main electrodes, which generates a magnetic field between them, and exerts a Lorentz force over the plasma cloud. As a result the ions are expelled from the engine, producing thrust in the opposite direction of the plasma beam.

The specific impulse of this type of engine lies in the range of 500 s to 2000 s (Krejci & Lozano, 2018), also allowing for a very efficient consumption of fuel. While the thrust levels achieved by this type of engine are in the range of 30 μN at 2 W of power, with a mass of around 500 g (Shaw, 2011).

2.4.3 Hall Effect Thruster

In the case of Hall Effect Thruster, a neutral gas is fed to a ionization and acceleration chamber, which is then ionized by collisions with electrons also injected in

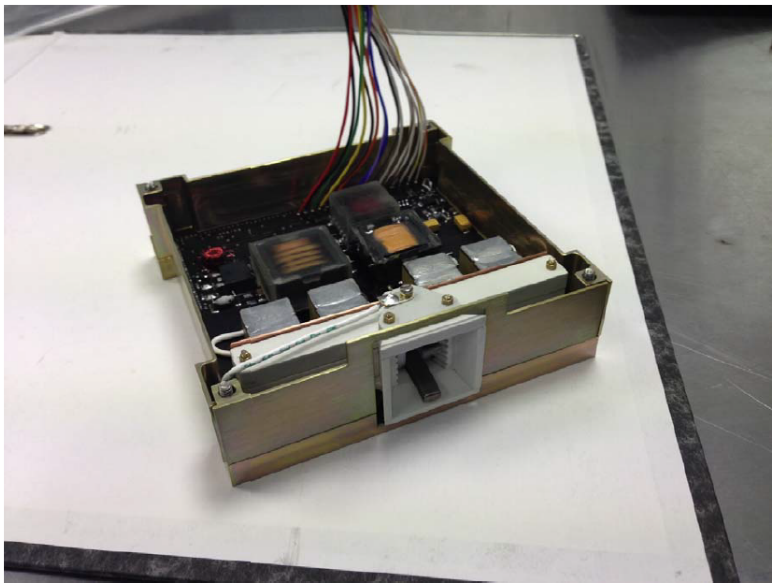

Figure 2.16: Pulsed plasma thruster developed by Clyde Space and Mars Space Ltd. Courtesy of Mars Space and Clyde Space.

this chamber, see Fig. 2.17. The chamber is composed of an anode and a cathode, and a magnetic field is generated between them. This magnetic field causes the electrons to flow along the annular chamber, increasing the probability of collision with the neutral gas. The ions, in turn, are accelerated by the potential drop between the electrodes.

Specific impulses in the order of 1500 s, can be achieved for this type of thrusters, which is somehow less than what electrospray and other ionic engines can offer. However, they offer thrust densities in the same order of magnitude, and they don't require acceleration grids, which are a lifetime limiting factor in other type of engines (Krejci & Lozano, 2018). Usual fuels for Hall Effect thrusters normally include Xenon, Krypton, Iodine, Bismuth and Argon. (Tummala & Dutta, 2017). Hall Effect Thrusters don't have flight heritage on CubeSats. However, some of them have flown in larger satellites such as SMART-1 (Krejci & Lozano, 2018).

Figure 2.18 depicts a Hall Effect Thruster being tested at NASA facilities, NASA being one of the main institutions working on the development of this tech-

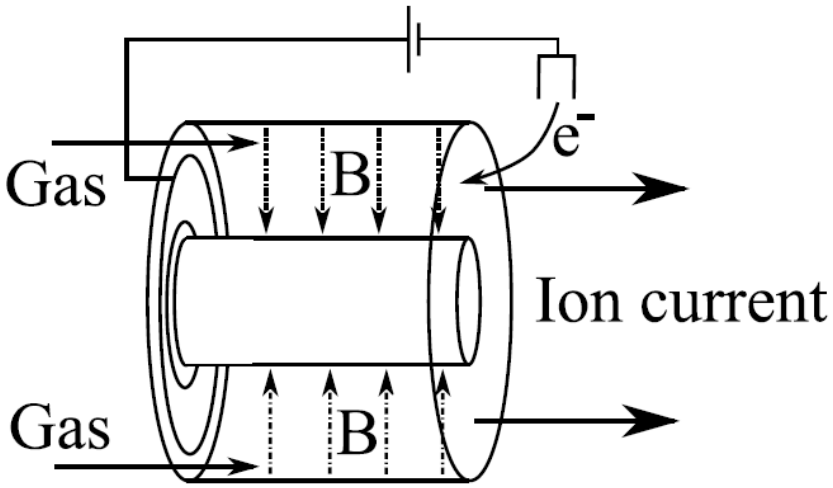

Figure 2.17: Hall Thruster schematic (Krejci & Lozano, 2018).

nology, together with the private company Busek Space Propulsion and Systems.

2.4.4 CubeSat Ambipolar Thruster

A fourth form of electric propulsion is called CubeSat Ambipolar Thruster (CAT), also known as Helicon Thruster (Collard & Sheehan, 2016). This is an electrodeless type of engine that generates thrust by expelling plasma through a magnetic nozzle, as shown in in Fig. 2.19. This figure shows how the propellant is fed into a chamber where it is ionized by means of radiofrequency. These plasma thrusters operate by using electromagnetic waves known as helicon waves, in order to heat electrons which then ionize the propellant to a 95 % ionization fraction or greater (Sheehan *et al.*, 2015). Then the plasma is accelerated by a permanent magnet around the plasma chamber, resulting in a high velocity plasma plume, generating thrust in the opposite direction. The diverging magnetic nozzle expands the plasma, both ions and electrons, producing a stream of electrons and energetic ions. This produces zero net current so no neutralizing cathode is required. Note how this type of engine doesn't require electrodes for its operation, a fact that allows to save mass and volume. The fuels that can be used for CubeSat Ambipolar Thrusters

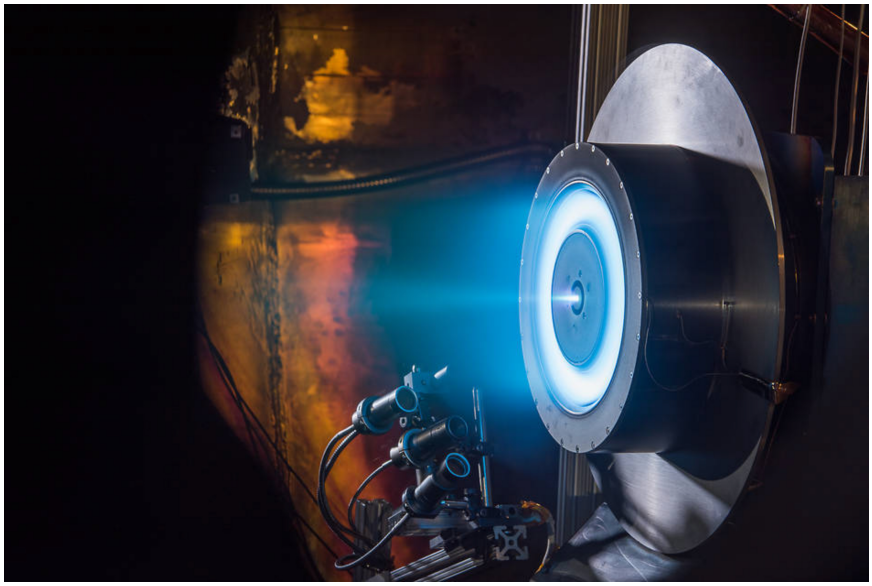

Figure 2.18: Hall Thruster test. Courtesy of NASA.

are Argon and Xenon, with radio frequency powers of 220 W at 14 MHz. CAT can provide small spacecraft with large ΔV, up to 1 km/s.

Figure 2.20 depicts an artistic impression of a CubeSat Ambipolar Thruster integrated in a 3U CubeSat operating in space. Table 2.2 shows some of the most important features for a CubeSat Ambipolar thruster with Xenon propellant, such as power, specific impulse, thrust, etc. Because of the features of this type of thruster, it has been proposed even for interplanetary missions, such the MarsCat, or Mars Array of Ionospheric Research Satellites using the CubeSat Ambipolar Thruster (Bering *et al.*, 2016), which is a mission to explore the ionosphere of Mars, investigating features such as its plasma and magnetic structure.

2.4.5 Micro Cathode Arc Thruster

Micro Cathode Arc Thrusters (μCAT) for CubeSats are composed of a couple of electrodes, an insulator material, a magnetic coil and a spring that pushes the solid fuel forward and is the only moving part of the system. Refer to figures 2.21 and 2.22 for a graphic depiction of a coaxial and a ring configurations respectively. The cathode material, which acts as fuel, is eroded through an electric discharge,

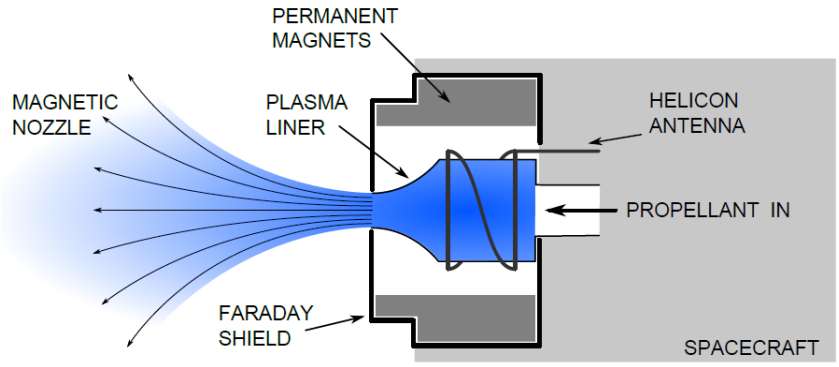

Figure 2.19: A schematic diagram of a CubeSat Ambipolar Thruster (Sheehan *et al.*, 2015).

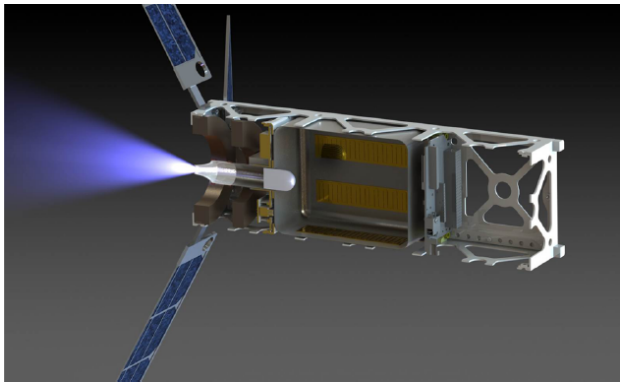

Figure 2.20: CAT thurster within 3U CubeSat (Spangelo & Longmier, 2015).

Table 2.2: CAT parameters for Xenon propellant (Sheehan *et al.*, 2015)

Power	10 - 50 W
Flow Rate	5 - 15 sccm
Isp	400 -800 s
Efficiency	10% - 40%
Thrust	0.5 - 4 mN
Thrust/Power	50 - 80 mN/kW

which generates a gas of plasma. This plasma is then accelerated by an electric field generated by the magnetic coil. This magnetic field exerts a Lorentz force in the plasma ions, expelling them from the nozzle, and generating the thrust. By varying the frequency of the electric discharges, the thrust levels can be controlled. According to the work of Keidar (Keidar, 2016), thrust levels between 1 μN and 0.05 mN can be achieved with this type of engines. According with the same source, lifetimes of over two months have been achieved during continuous operation of the engines.

This technology offers high specific impulse, in the order of 2000 to 3500 s. They use solid metal fuel such as Teflon or Xenon, consume low levels of energy, in the order of 0.1 W, and have a low mass of around 200 g, while not requiring pressure tanks, all of them features which makes them ideal for nanosatellites applications.

The exhaust speed is on the order of 10^4 m/s. Since a gas feed system is unnecessary, this simplifies the thruster design and decreases the thruster mass, while also avoiding the possibility of gas leakage that could decrease the thruster efficiency (Keidar, 2016).

The μCAT is a simple electric propulsion device that combined with a magnetic coil and an inductive energy storage Power Processing Unit (PPU) results in a low mass - <100 g - system. A picture of a μCAT prototype system is shown in 2.23, while Fig. 2.24 depicts a μCAT thruster board, in order to have a feeling of their dimensions and their potential for application in CubeSats.

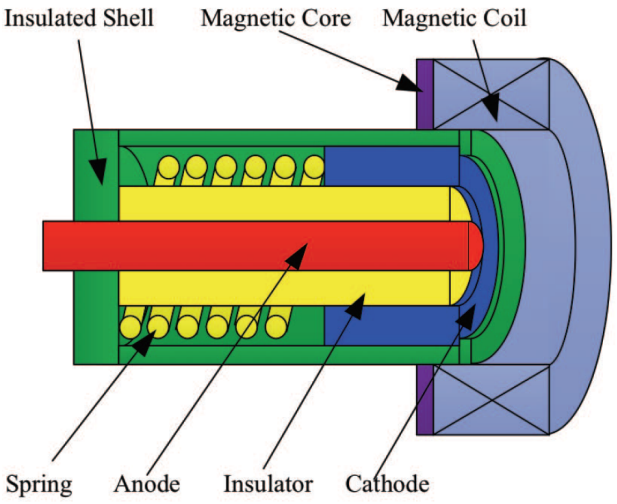

Figure 2.21: Schematic design of coaxial electrode μCAT (Keidar, 2016).

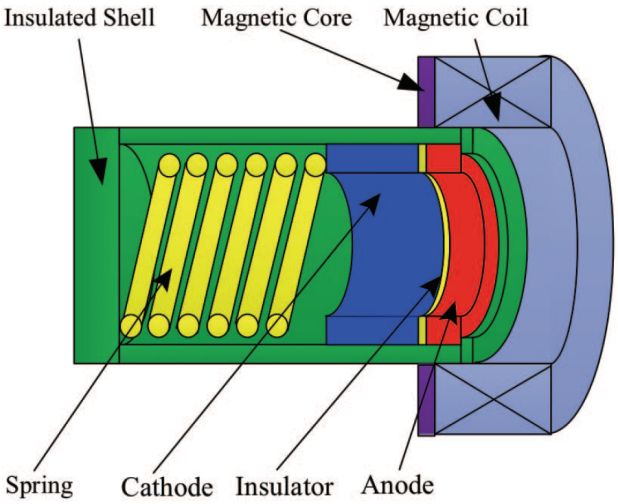

Figure 2.22: Schematic design of ring electrode μCAT (Keidar, 2016).

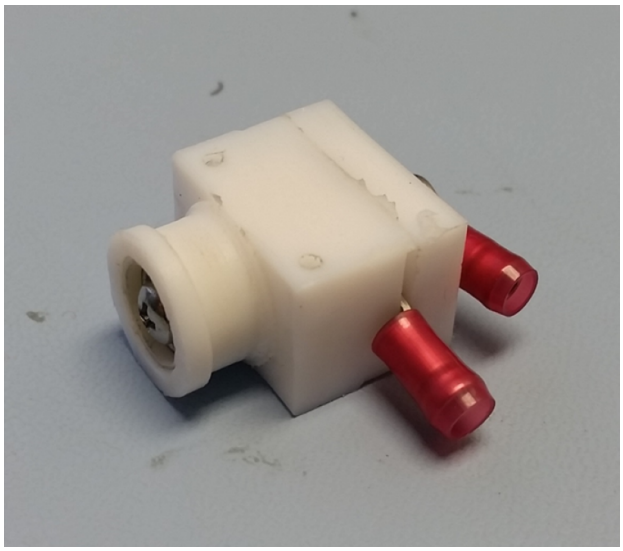

Figure 2.23: μCAT thruster (Wenberg *et al.*, 2017).

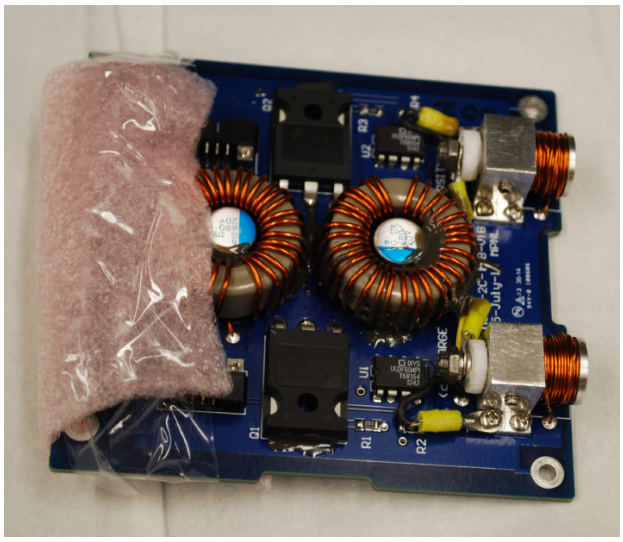

Figure 2.24: μCAT thruster board (Wenberg *et al.*, 2017).

2.4.6 Deorbiting Methods Comparison

In order to provide a better insight of the advantage and disadvantages of each of the deorbiting methods presented in sections 2.3 and 2.4, Table 2.3 is provided. All of the approaches have their own merits, and furthermore they possess inherent features that work both in their favour as well as against them. While the choice of the approach to select will be dependant on the design and necessities of each mission, it can be seen that novel electric propulsion provide important advantages over the existing approaches. Thus the importance of studying this approach, mainly in the light that this is a relatively new technology, and there exists a significant literature gap when it comes to its application to the deorbiting problem.

2.5 Attitude Determination and Control Systems for CubeSats

2.5.1 Attitude Sensors

ADCS systems require a minimum of two sensors in order to determine the full attitude information of the satellite. There are a number of sensors that are used for this purpose, namely, the following ones: magnetometers, Sun sensors, Earth sensors, gyroscopes, and star trackers.

Magnetometers are in charge of providing readings of the local geomagnetic field. They are lightweight, have no moving parts and consume low levels of energy, besides being able to operate in a wide range of temperatures. One disadvantage of magnetometers its is sensitivity to magnetic dipoles generated by magnetorquers, a type of actuators commonly used in conjunction with magnetometers. There are two approaches to overcome this disadvantage. The first one is to operate both components in a time shared scheme, activating one element while turning off the other. The second approach is to deploy the magnetometers away from the magnetometers, in which case both devices can be operated at the same time.

Sun sensors provide the Sun vector. In some early CubeSats the solar panels were used in order to obtain a coarse sun vector. As miniaturization has progressed,

Table 2.3: Deorbiting approaches comparison

Technology	Advantages	Disadvantages
Drag Sail	No fuel consumption. No energy consumption.	Elaborated stowage and deployment mechanisms. Performance dependant on initial orbital altitude. Long deorbiting times, increasing the probability of collisions. Once doployed, cannot be deactivated.
Inflatables	No fuel consumption. No energy consumption.	Elaborated stowage and deployment mechanisms. Performance dependant on initial orbital altitude. Susceptible to deflation by impact with orbiting particles. Long deorbiting times, increasing the probability of collisions. Once doployed, cannot be deactivated.
Tethers	No fuel consumption. Can also be used for orbital housekeeping.	Elaborated stowage and deployment mechanisms. Long deorbiting times, increasing the probability of collisions. Require a libration dynamics control system. Can get easily entangled or even broken.
Propulsion	Easily integration in CubeSats. In general, absence of movable parts, reducing the probability of failures. Can also be used for orbital housekeeping. Can be turned on and off, allowing for leeway during the deorbiting operation. Performance independent on initial orbital altitude. Short deorbiting times, which decreases the probability of collisions.	Fuel consumption. Energy consumption. Requires at least some degree of attitude control.

it is now possible to integrate proper Sun sensors into the body of CubeSats, thus being able to obtain more precise measurements of the Sun vector.

Earth sensor can be grouped in two categories: sensors with CMOS camera, and the Earth horizon sensors. The CMOS Earth sensor could image the Earth only in sunlit and the output pointing knowledge is around 0.5 deg. In the other hand, the Earth horizon sensors can work even in eclipse (Xia *et al.*, 2017).

Gyroscopes, in the other hand, are inertial sensors, and are in charge of providing the angular velocity vector of the satellite. They come handy in conditions of eclipse, since they can generate a mock Sun vector, or also in the case the magnetometers fail, as the can also generate a mock geomagnetic field vector (Xia *et al.*, 2017).

Finally, we have the star trackers, which can actually solve the full attitude information by themselves. The main disadvantage is that they still tend to be more expensive than the sensors previously discussed. Star trackers can have a form factor of 10 cm $\times$ 5 cm $\times$ 5 cm, a mass less than 300 g and power consumption less than 1 W (Xia *et al.*, 2017).

2.5.2 Attitude Actuators

Attitude sensors have to be complemented with attitude actuators in order to provide control over the pointing of the satellite in space. Some of the most common attitude actuators are: magnetorquers, gravity gradient booms, reaction and momentum wheels, as well as thrusters.

Magnetorquers are electromagnets that can generate magnetic dipoles, which then interact with Earth's magnetic field and generate torques that can be used to control the orientation of the satellite in space. They are light, their construction is simple, cheap, and have no movable parts, features that makes them ideal for their application in space systems, especially in low budget nanosatellites. The main disadvantage of this type of actuators is that they cannot generate torques in any arbitrary direction, they can only generate torques perpendicular to the local magnetic field.

Gravity gradient booms consist of a deployable tether with the satellite in one end and a mock mass in the other end. Because of the gravity gradient experienced

by bodies in orbit, this configuration will align the system passively with the nadir. The main advantage of this approach is that it doesn't require energy consumption. One disadvantage is that the only attitude that can be attained is nadir pointing. Also, it involves the deployment of actuators in space, making the system prone to failures.

One of the most popular attitude actuators in the past few years, especially in the field of CubeSats, are the reaction and momentum wheels. Reaction wheels are spun up and down in order to change the attitude of the satellite. Momentum wheels are always spinning, creating resistance to the change of attitude of the satellite (Xia *et al.*, 2017). The usual pointing accuracy of this actuators is of 1°. One of the main disadvantages of this approach is the inclusion of movable parts, which can limit the lifetime of the system.

Thrusters are also an option as attitude actuators. Up until now, the thrusters more popular within the CubeSat community used cold gas technology, as they are simple in construction, provide a high specific impulse, low power consumption, small volume and mass (Xia *et al.*, 2017). However, in the past few years, electric thrusters have been gaining ever more popularity.

2.5.3 Attitude Determination Algorithms

Common attitude determination algorithms, such as TRIAD and QUEST (quaternion estimation), require a minimum of two independent vector measurements. In one hand, the TRIAD algorithm provides a non-optimal solution for the attitude based on two vector measurements. In the other hand, the QUEST algorithm achieves the best attitude estimation from an arbitrary number of measurement vectors (Shuster & Oh, 1981).

Because CubeSats face tight constraints in terms of volume, mass, and budget, it is not always possible to equip them with enough sensors and actuators, and therefore no full attitude determination is available. Also, even in the case when enough sensors are available at the beginning of the mission, there is the possibility that some of the components experience failures during the execution of the mission, and no full attitude information is available when it is time for the deorbiting phase. This fact is critical, since for a propulsive deorbiting of a satellite,

the spacecraft need to point its thrusters in a suitable direction in order to lose orbital energy. Therefore, it would be useful to develop methods with minimum requirements in terms of sensors, actuators, and processing capabilities.

2.5.4 Survey of ADCS in CubeSats

The survey from Xia et al. (Xia *et al.*, 2017) shows that, from 2013 until the end of 2016, more than 552 nanosatellites, including 500 CubeSats, were launched. This study is interesting since it shows us the ADCS capabilities available to this realm of satellites. According to this article, ADCS information for a total of 357 nanosatellites was available and analysed.

This study claims that 16 out of 357 CubeSats launched into orbit were not equipped with any means of attitude determination and control. This is depicted in Fig. 2.25. This implies that these satellites would have no means for a propulsive deorbiting maneuver, since there is no control at all over the attitude of the spacecraft. The study doesn't include the respective information but it is reasonable to assume they also don't count with some passive way of deorbiting. This is worrying from the space debris point of view, since it means that these CubeSats are left to natural orbital decay, which, depending on their initial orbits, can range from a few weeks to several decades.

Similarly, 9 CubeSats were spin-stabilized, which is a simple and common way to control the attitude of some satellites that don't require three axis stabilization. This is shown in Fig. 2.26. Spin-stabilization offers the possibility for propulsive CubeSat deorbiting. However, it can be seen that the fraction of spin-stabilized CubeSats is very low.

Figure 2.27 show how 64 CubeSats were equipped with passive magnetic attitude control. While this type of attitude control offers poor accuracy, it may open the door for some propulsive manoeuvres for deorbiting purposes.

Meanwhile, a total of 9 CubeSats were stabilized through the means of gravity gradient, as shown in Fig. 2.28. This approach to attitude control leaves little room for propulsive deorbiting manoeuvres, and is not further explored within this thesis.

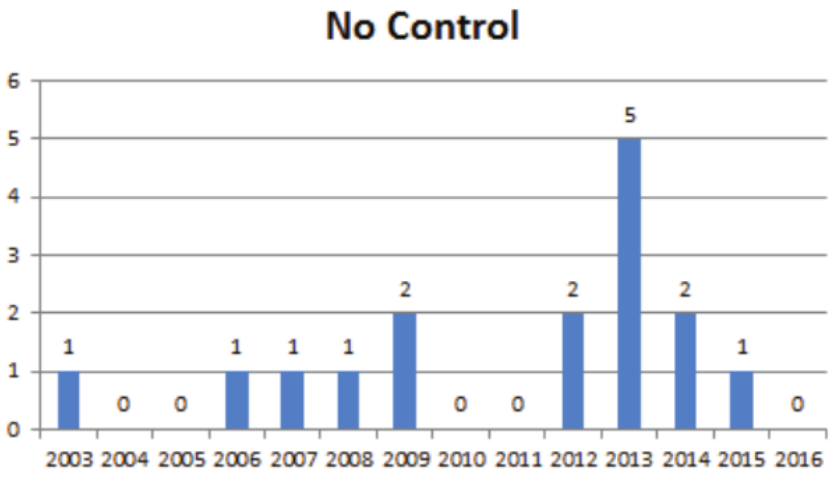

Figure 2.25: Survey of NanoSats/CubeSats without ADCS (Xia *et al.*, 2017).

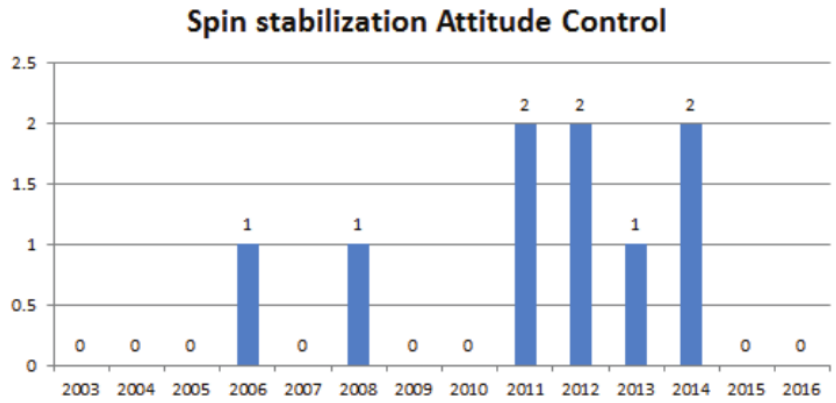

Figure 2.26: Survey of Spin-Stabilization Attitude Control Scheme (Xia *et al.*, 2017).

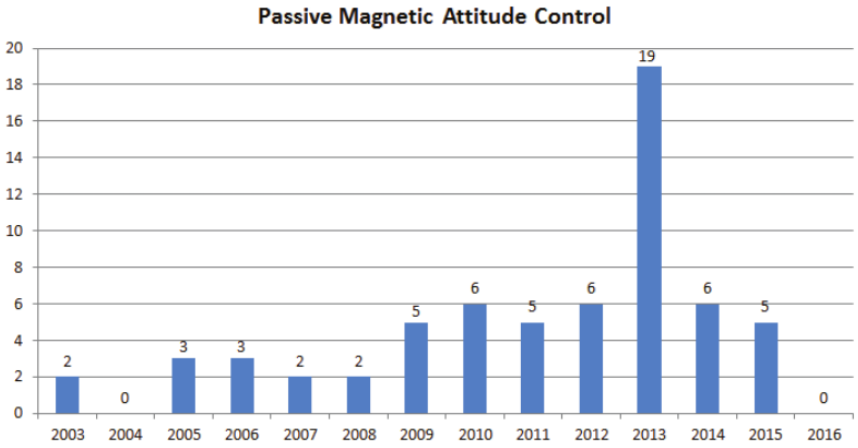

Figure 2.27: Survey of Passive Magnetic Attitude Control Scheme (Xia *et al.*, 2017).

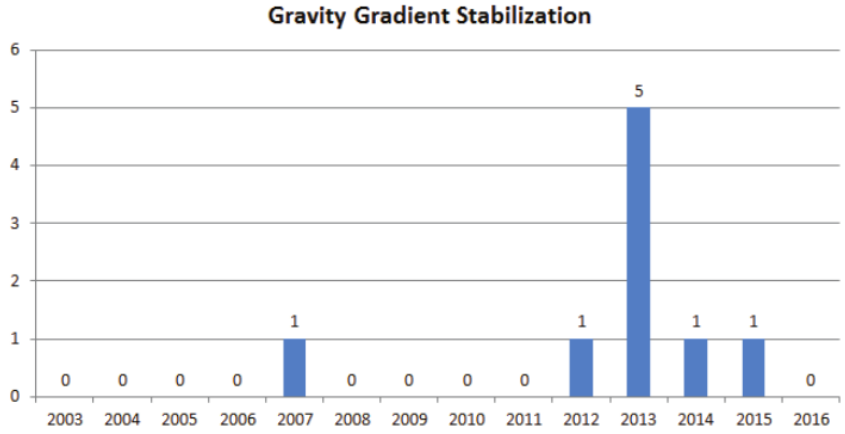

Figure 2.28: Survey of Gravity Gradient Attitude Control Scheme (Xia *et al.*, 2017).

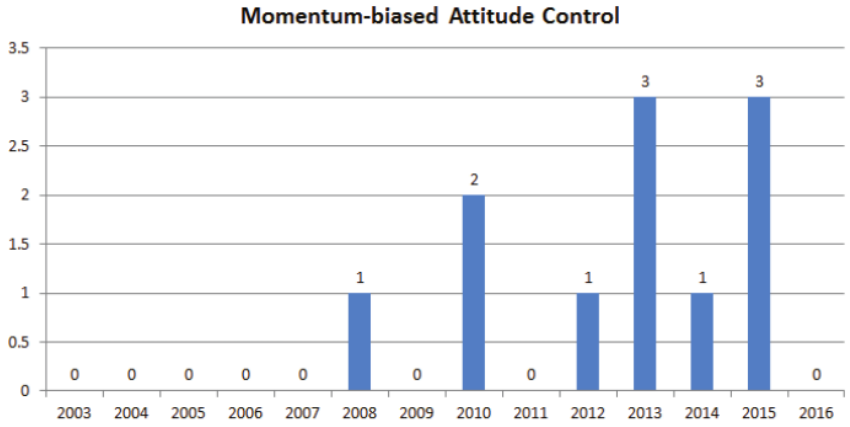

Figure 2.29: Survey of Momentum-biased Attitude Control Scheme (Xia *et al.*, 2017).

A total of 11 of these CubeSats were stabilized by means of momentum wheels for attitude control, as depicted in Fig. 2.29. As discussed earlier, momentum wheels spin continuously and oppose to the change in the satellite's attitude. Therefore, the CubeSat will be stabilized in the inertial frame. This fact also opens the possibility for a deorbiting maneuver using thrusters.

Reaction wheels have become very popular within the CubeSat community. This can be seen clearly in Fig. 2.30, where a total of 201 CubeSats were provided with this type of actuators. Usually reaction wheels offer three axes attitude control, and are present when full attitude information is available. Therefore, in these cases, the deorbiting operation using thrusters may become trivial.

Another very popular method for CubeSat stabilization are magnetorquers. Figure 2.31 shows a total of 39 CubeSats equiped with these actuators. It is because of the popularity of this type of actuators, that this thesis is focused in their use as attitude control means.

2.6 Stability Analysis

In this section, an overview on stability is given. Stability refers to the capability of a control system to remain at an equilibrium point even in the presence of

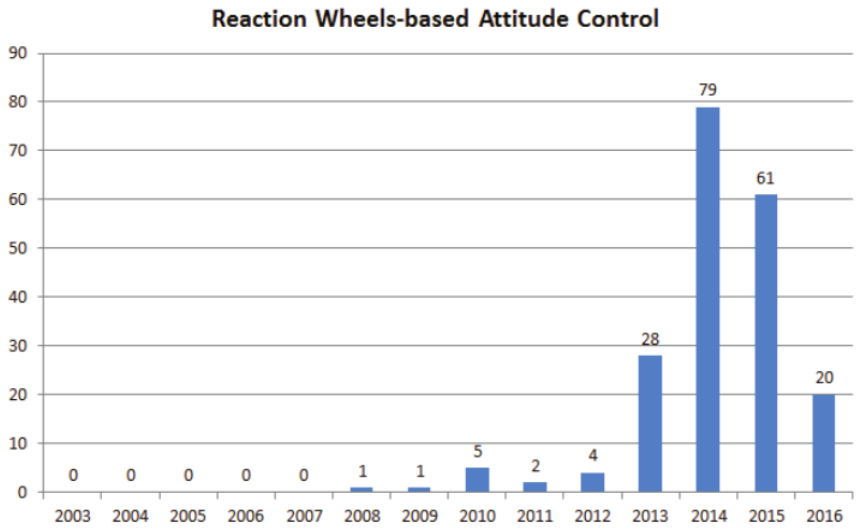

Figure 2.30: Survey of Reaction Wheels-based Attitude Control Scheme (Xia *et al.*, 2017).

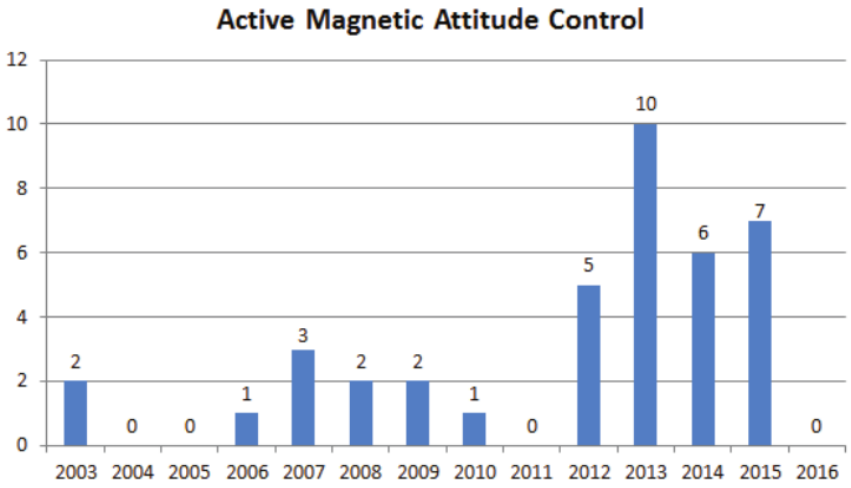

Figure 2.31: Survey of Active Magnetic Attitude Control Scheme (Xia *et al.*, 2017).

disturbances. An equilibrium point is said to be stable if all possible solutions that start at nearby points stay nearby; otherwise, it is said to be unstable. It is said to be asypmtotically stable if all possible solutions starting at nearby points not only stay nearby, but also tend to the euilibrium point as time approaches infinity (Khalil, 1996).

The analysis of stability of mechanical systems has affected a number of mathematical and engineering disciplines. We can begin with Lagrange (Lagrange, 1788), who investigated the stability of mechanical systems at local minima of the potential function. In one of the first works on control theory, Maxwell (Maxwell, 1868) analyses the stability of mechanical governors using linearisation. On their work, Thomson & Tait (Thomson & Tait, 1867) study the asymptotic stability of mechanical systems when subject to dissipative forces also by linearisation. Lyapunov (Lyapunov, 1892) developes the elements of a stability notion and of stability criteria that are applicable to a broad class of non-linear systems. The so-called invariance principles were developed to in order establish stability properties of dynamical systems by weaker requirements than those required by Lyapunov's criteria. Work on invariance principles can be credited to Barbashin & Krasovskii (Barbashin & Krasovskii, 1952); LaSalle presented his Invariance Principle in (Lasalle, 1968). More recent work on stability includes (Lasalle & Lefschetz, 1962), (Hahn, 1963) and (Chetaev, 1961). More treatments in nonlinear control include (Khalil, 1996) and (Sastry, 1999).

2.7 Monte Carlo Simulations

Monte Carlo simulations are used in order to test the robustness of control algorithms, in the presence of model uncertainties. Monte Carlo simulations make use of numerical models to predict the probability of certain outcomes, when the model is subject to a variety of initial conditions. A brief history of the development of this method is as follows. Comte de Buffon (Comte de Buffon, 1777) suggested the use of random sampling in order to find the solution to an integral. Laplace (Laplace, 1886) developed on that idea and suggested to use the method to compute π. Lord Kelvin (Kelvin, 1901) applied the Monte Carlo method to the kinetic theory of gases. Courant et al. (Courant *et al.*, 1928) showed the relation

that exists between random walks and the solution of partial differential equations. Literature on Monte Carlo and its use to solve problems in statistical mechanics, economics and other fields include (Metropolis & Ulam, 1949), (Donkster & Kac, 1950) and (Householder *et al.*, 1951). Two landscape papers are (Kahn, 1950) and the algorithm of Metropolis et al. (Metropolis *et al.*, 1953).

2.8 Linear Periodic Time Varying Systems

Linear Periodic Time Varying Systems (LPTV) are relevant to this work since the orbit of a satellite can be expressed in this way. This fact allows the use of Floquet Theory in order to assess the stability of some systems. An LPTV system is a linear time-varying system with the coefficients changuing periodically (Yin, 2009). LPTV systems are important in a variety of fields. One of these fields is electronics, where they are used in the design of filters, such as presented in (Vaidyanathan, 1988) and (Gandhi & Mitra, 1997). They also find a place in network coding, such is the case of (Rajawat *et al.*, 2009), where they present a polyphase approach to the wireless linear network coding problem. The robustness of this type of systems is also the subject of study, as in (Zhang *et al.*, 1996), (Hagiwara & Umeda, 2007) and (Kim *et al.*, 2006). The problem of aliasing is analysed using LPTV theory such as in the case of the following works (Chen & Qiu, 1997) and (Chen, 2006).

2.9 Summary and Discussions

In this chapter, the literature review regarding CubeSats, their current applications, and rate of launching has been discussed. Because these rates are ever increasing, their potential negative impact on the space debris problem is also examined, especially considering oncoming mega-constellations such as StarLink and OneWeb, in addition to existing ones such as Planet Lab's and Spire. It is especially concerning that most of these nanosatellites don't possess any means of deorbiting or decommissioning system to remove them from orbit at the end of their operational lifetimes. This make many of these satellites not compliant

with the accepted international guidelines that recommend any satellite to be decommissioned no later that 25 years after the end of their missions. This poses a threat to operational satellites that share orbital ranges with these spacecrafts.

Some current approaches to tackle this problem are then discussed. There are four main approaches: drag sails, inflatables, electric tethers, and the most recently developed technology of electric propulsion. It is shown that the first three technologies have some inherent disadvantages over the fourth one, namely, they have movable parts, require the deployment of actuators in space, some of them include pressure tanks, and their masses and volumes may be restrictive for this type of satellites. In the case of electric propulsion, engines are being developed that offer high specific impulse, most of them don't have movable parts, and don't require the deployment of actuators in space, which makes them very attractive for applications in nanosatellites, especially CubeSats. While sails, inflatables or tethers might be an appropriate choice depending on some missions design and requirements, it is clear that propulsion engines have significant advantages that can be exploited. Furthermore, since this technology is relatively new in the field of CubeSats, there is an important literature gap regarding its application to the deorbiting problem. Hence the importance of study approaches to achieve this objective.

Five electric technologies are the focus of analysis: Electrospray, Micro Pulsed Plasma Thruster, Hall Effect Thruster, CubeSat Ambipolar Thruster, and Micro Cathode Arc Thruster. The principle of operations of each one of them, as well as their main features, such as specific impulse, mass, volume, fuels, etc., are presented, wherever this information is available.

In order to apply this propulsion technology to the deorbit problem, a way to point the spacecraft in space is needed, such that thrust is used to deorbit the CubeSat. This is especially challenging since in many cases these satellites are not equipped with full attitude determination capabilities. Therefore, an analysis is performed on the type of sensors that are usually present in CubeSats, as well as a survey of the types of ADCS system that are normally on board them. This gives a feeling that, in order to apply these thrusters to the deorbiting problem, it is necessary to come up with ways to control the attitude of the satellite with minimum sensing and actuating capabilities. It must be noted that such attitude

control systems have the potential to be useful also in the drag sail scenario, and an analysis on this is also performed in this thesis.

Finally, a literature review regarding stability and robustness analysis, as well as LPTV systems is given.

Chapter 3

Mathematical Background and Environment

3.1 Introduction

Theoretical backgrounds are introduced, including 1) equations of motion and 2) environmental models. Firstly, the mathematical foundations which govern the motion of a satellite orbiting the Earth, such as orbital dynamics and attitude kinematics, are established. This provides the ground for the control laws and algorithms that are later developed. Secondly, the Earth's magnetic field and atmospheric models adopted in the numerical simulations are introduced.

3.2 Reference Frames

Three different coordinate systems are used to describe the motion of a satellite, which are: the Earth-centered inertial (ECI) frame, the local-vertical/local-horizon (LVLH) frame, and the body (B) frame. The ECI frame, with the unit vectors $\{\mathbf{x_{ECI}}\ \mathbf{y_{ECI}}\ \mathbf{z_{ECI}}\}$, has its origin at the center of the Earth. The unit vector $\mathbf{x_{ECI}}$ points towards the point of the vernal equinox, also known as the First Point of Aries. This is the direction from the Sun to the ascending node of the intersection between the terrestrial equatorial plane and the ecliptic, which equals the direction in which the Sun is seen from Earth at vernal equinox (Walter, 2012)

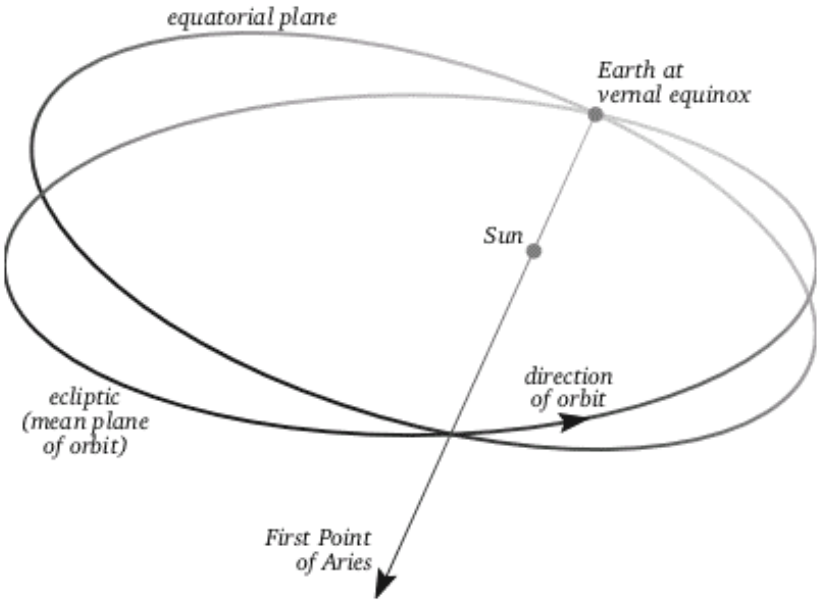

Figure 3.1: Definition of the direction of the First Point of Aries or point of vernal equinox. www.earthsky.org

as shown in Fig. 3.1. The unit vector $\mathbf{z_{ECI}}$ is aligned with the Earth rotation axis. The unit vector $\mathbf{y_{ECI}}$ completes the right-handed frame. The ECI frame is presented graphically in Fig. 3.2. The LVLH frame, with the unit vectors $\{\mathbf{x_{LVLH}}\ \mathbf{y_{LVLH}}\ \mathbf{z_{LVLH}}\}$, has its origin at the center of mass of the CubeSat. The unit vector $\mathbf{z_{LVLH}}$ points along the negative position vector of the CubeSat. The unit vector $\mathbf{y_{LVLH}}$ points along the negative orbit normal. The unit vector $\mathbf{x_{LVLH}}$ is defined by the cross product of $\mathbf{y_{LVLH}}$ and $\mathbf{z_{LVLH}}$ vectors, as shown in Fig. 3.3. And finally, the B frame, with the unit vectors $\{\mathbf{x_B}\ \mathbf{y_B}\ \mathbf{z_B}\}$, has its origin at the center of mass of the satellite, and its unit vectors are assumed to be aligned with the principal axes of the satellite, as shown in Figure 3.4.

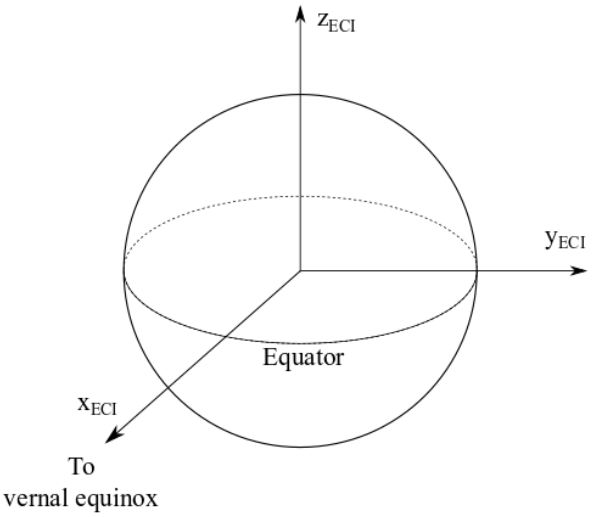

Figure 3.2: Earth-centered inertial (ECI) frame.

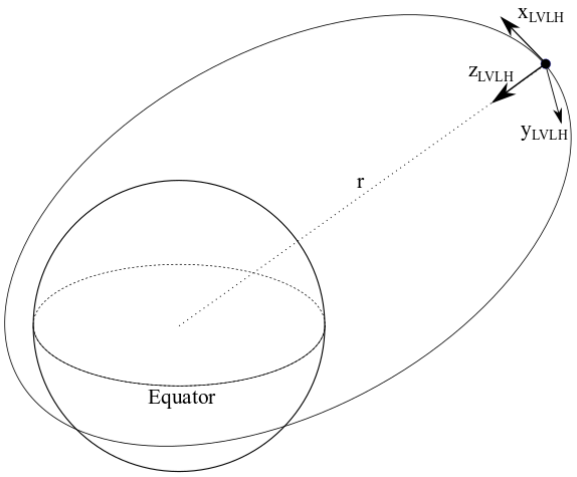

Figure 3.3: Local-vertical/local-horizon (LVLH) frame.

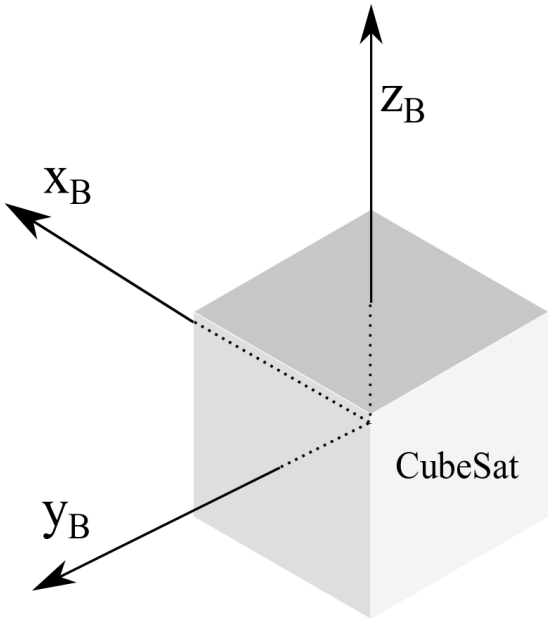

Figure 3.4: Body (B) frame.

3.3 Equations of Motion

3.3.1 Gauss's Variational Equations

In order to be able to develop any deorbiting algorithm, first it is necessary to define the equations that govern the motion of a body orbiting the Earth. This motion can be described using Gauss's Variational Equations (GVE's). GVE's are not the only way to describe the orbital motion of a body, however, they are very practical since they allow for orbital perturbations to be accounted for easily. They are expressed in the ECI frame and describe the evolution in time of six Keplerian orbital elements, as presented next (Walter, 2012):

$$\dot{a} = \frac{2a^2}{h}[e\sin\nu \cdot a_r + (1 + e\cos\nu)a_\theta] \tag{3.1a}$$

$$\dot{e} = \frac{h}{\mu}[\sin\nu \cdot a_r + (\frac{e + \cos\nu}{1 + e\cos\nu} + \cos\nu)a_\theta] \tag{3.1b}$$

$$\dot{i} = \frac{r\cos(\nu + \omega)}{h}a_h \tag{3.1c}$$

$$\dot{\omega} = \frac{h}{e\mu}[-\cos\nu \cdot a_r + \frac{2 + e\cos\nu}{1 + e\cos\nu}\sin\nu \cdot a_\theta] - \frac{r\sin(\nu + \omega)\cos i}{h\sin i} \cdot a_h \tag{3.1d}$$

$$\dot{\Omega} = \frac{r\sin(\nu + \omega)}{h\sin i}a_h \tag{3.1e}$$

$$\dot{M} = -\sqrt{1 - e^2}(\frac{2r}{h}a_r + \dot{\omega} + \dot{\Omega}\cos i) + n \tag{3.1f}$$

where a is the semi-major axis in meters, e is the eccentricity, i is the inclination in radians, ω is the argument of periapsis in radians, Ω is the longitude of ascending node in radians, M is the mean anomaly in radians, ν is the true anomaly in radians, h is the specific angular momentum in m^2/s, μ is Earth's gravitational constant equal to 3.986×10^{14} m^3/s^2, r is the orbit radius in m, n is the mean motion in rad/s, a_r is a radial perturbing acceleration, that is, acting along the position $\mathbf{r}$ vector, in m/s^2, a_θ is a cross-radial perturbing acceleration, that is, acting in the direction of travel, in m/s^2, and a_h is a perturbing acceleration perpendicular to the orbital plane, in m/s^2. Figures 3.5 and 3.6 show a graphical description of the Keplerian elements and the perturbing accelerations unit vectors respectively.

There are a number of different perturbation accelerations that affect the orbit of a body around the Earth. Examples of these accelerations are: lunar and solar gravitational pulls, solar pressure, accelerations caused by Earth's oblateness, of which J_2 term is the most significant one, and atmospheric drag. In the LEO environment, however, gravitational pulls and solar pressure can often be neglected, and the J_2 term and atmospheric drag are the perturbations which dominates over the rest. When the J_2 acceleration is plugged into the equations of motion, we obtain the following set of expressions, in the ECI frame, defining the accelerations

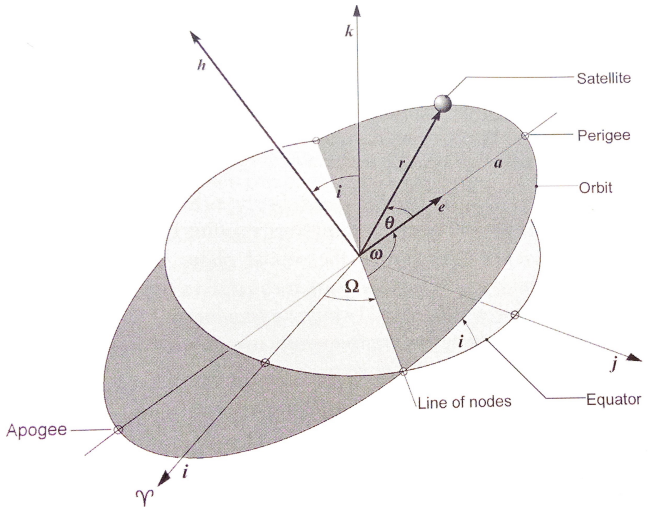

Figure 3.5: Keplerian elements. Modified from (Walter, 2012).

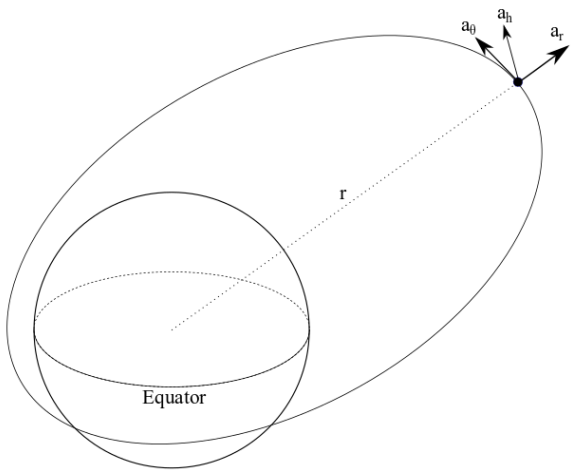

Figure 3.6: Perturbing accelerations a_θ, a_r, and a_h.

that describe the motion of the satellite (Sidi, 1997):

$$a_x = \mu \left[-\frac{x}{r^3} + A_{J2} \left(15\frac{xz^2}{r^7} - 3\frac{x}{r^5} \right) \right] \tag{3.2}$$

$$a_y = \mu \left[-\frac{y}{r^3} + A_{J2} \left(15\frac{yz^2}{r^7} - 3\frac{y}{r^5} \right) \right] \tag{3.3}$$

$$a_z = \mu \left[-\frac{z}{r^3} + A_{J2} \left(15\frac{z^3}{r^7} - 9\frac{z}{r^5} \right) \right] \tag{3.4}$$

where $A_{J2} = \frac{1}{2} J_2 R_e^2$ in m^2, the coefficient J_2 being equal to 1.08263×10^{-3} and R_e is the mean radius of the Earth, being equal to 6371.2×10^3 meters.

3.3.2 Attitude Kinematics

Attitude kinematics express the orientation in space of a satellite relative to some reference frame, regardless of the forces that affect it. This orientation can be described in a number of ways, such as Euler angles, rotation matrices and quaternions. Each one of these notations has certain advantages as well as disadvantages. From (Junkins & Schaub, 2001), there are four facts regarding attitude representations as follows:

1. A minimum of three coordinates is required to describe the relative attitude between two reference frames.

2. Any minimal set of three attitude coordinates will contain at least one geometrical orientation where the coordinates are singular, namely at least two coordinates are undefined or not unique.

3. At or near such a geometric singularity, the corresponding kinematic differential equations are also singular.

4. The geometric singularities and associated numerical difficulties can be avoided altogether through a regularization. Redundant sets of four or more coordinates exist which are universally determined and contain no geometric singularities.

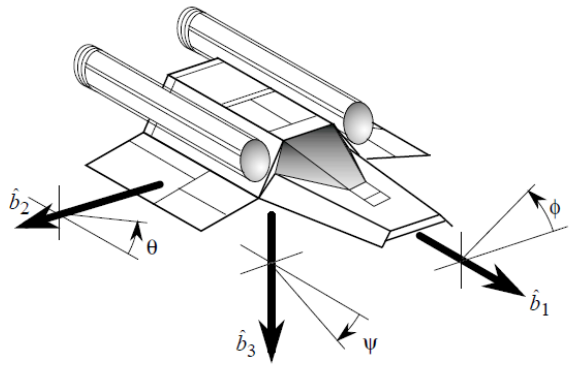

Figure 3.7: Yaw, Pitch and Roll Euler Angles (Junkins & Schaub, 2001).

Firstly, Euler angles describe the orientation of a body using three coordinates, this is to say, three rotations around three axes. Note that the order in which the rotations are executed is important in this case, rotating around the axes x-y-z, in that order, does not yield the same resultant orientation as rotating around the axes in the order z-y-x. The orientation of aircraft and spacecraft is commonly expressed in Euler angles of yaw, pitch and roll (ψ,θ,ϕ), as shown in Fig. 3.7. Euler angles have the advantages of being intuitive and only requiring three parameters, that is to say, they are computationally cheap, however, they may present geometric singularities where two angles are not uniquely defined.

In Fig. 3.8, there are two reference frames, N and B, with their respective unit vectors $\{\hat{\mathbf{n}}\} = \{\hat{\mathbf{n}}_\mathbf{1}, \hat{\mathbf{n}}_\mathbf{2}, \hat{\mathbf{n}}_\mathbf{3}\}$ and $\{\hat{\mathbf{b}}\} = \{\hat{\mathbf{b}}_\mathbf{1}, \hat{\mathbf{b}}_\mathbf{2}, \hat{\mathbf{b}}_\mathbf{3}\}$. To express the attitude of frame B with respect to frame N, we can define the angles α_{1i} as the angles between the unit vector $\hat{\mathbf{b}}_\mathbf{1}$ and the three unit vectors of the frame N. The cosine of these angles are known as the direction cosines with respect to the frame N. In this manner we can project $\hat{\mathbf{b}}_\mathbf{1}$ onto $\{\hat{\mathbf{n}}\}$ as follows (Junkins & Schaub, 2001):

$$\hat{\mathbf{b}}_\mathbf{1} = \cos\alpha_{11}\hat{\mathbf{n}}_\mathbf{1} + \cos\alpha_{12}\hat{\mathbf{n}}_\mathbf{2} + \cos\alpha_{13}\hat{\mathbf{n}}_\mathbf{3} \tag{3.5}$$

likewise, the vectors $\hat{\mathbf{b}}_\mathbf{2}$ and $\hat{\mathbf{b}}_\mathbf{3}$ can be expressed as:

$$\hat{\mathbf{b}}_\mathbf{2} = \cos\alpha_{21}\hat{\mathbf{n}}_\mathbf{1} + \cos\alpha_{22}\hat{\mathbf{n}}_\mathbf{2} + \cos\alpha_{23}\hat{\mathbf{n}}_\mathbf{3} \tag{3.6}$$

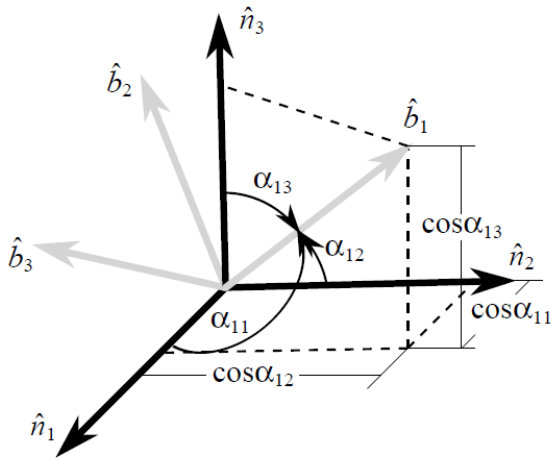

Figure 3.8: Direction Cosines (Junkins & Schaub, 2001).

$$\hat{\mathbf{b}}_\mathbf{3} = \cos\alpha_{31}\hat{\mathbf{n}}_\mathbf{1} + \cos\alpha_{32}\hat{\mathbf{n}}_\mathbf{2} + \cos\alpha_{33}\hat{\mathbf{n}}_\mathbf{3} \tag{3.7}$$

we can finally express the set of vectors $\{\hat{\mathbf{b}}\}$ in terms of the base vectors $\{\hat{\mathbf{n}}\}$ as:

$$\{\hat{\mathbf{b}}\} = \begin{bmatrix} \cos\alpha_{11} & \cos\alpha_{12} & \cos\alpha_{13} \\ \cos\alpha_{21} & \cos\alpha_{22} & \cos\alpha_{23} \\ \cos\alpha_{31} & \cos\alpha_{32} & \cos\alpha_{33} \end{bmatrix} \{\hat{\mathbf{n}}\} = [C]\{\hat{\mathbf{n}}\} \tag{3.8}$$

As it can be seen, the Direction Cosine Matrix (DCM) represents the orientation of a body using nine parameters. This mere use of nine parameters is one of their main disadvantages, DCMS's are computationally expensive, while also not being intuitive. Instead of being used to keep track of the orientation of a body, it is more common to use DCM's to transform vectors between different reference frames.

Finally, another tool to represent bodies attitudes, are the so called quaternions. The idea in this representation, is to express the rotation of one reference frame with respect to another one, using just one rotation axis and an angle of rotation. In Fig. 3.9 it can be seen how the orientation of reference frame B with respect to reference frame N can be expressed as a rotation of ϕ degrees around the rotation axis $\hat{\mathbf{e}}$.

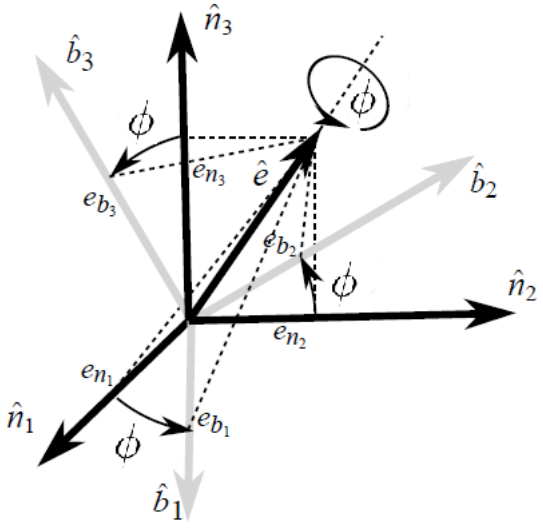

Figure 3.9: Illustration of Euler's Principal Rotation Theorem (Junkins & Schaub, 2001).

The quaternion vector can be expressed as follows:

$$q_0 = \cos(\phi/2) \tag{3.9a}$$
$$q_1 = e_1 \sin(\phi/2) \tag{3.9b}$$
$$q_2 = e_2 \sin(\phi/2) \tag{3.9c}$$
$$q_3 = e_3 \sin(\phi/2) \tag{3.9d}$$

While quaternions may not be quite intuitive, they don't present the phenomenon of indetermination, they require only four parameters, being less redundant than the DCM, and describe the attitude by means of just one rotation as opposed to three rotations as in the case of Euler angles and rotation matrices.

Thus, the attitude kinematics of a satellite can be described by the following quaternion equation:

$$\dot{\mathbf{q}} = \frac{1}{2} \begin{bmatrix} -[\boldsymbol{\omega}\times] & \boldsymbol{\omega} \\ -\boldsymbol{\omega}^{\boldsymbol{T}} & 0 \end{bmatrix} \mathbf{q} \tag{3.10}$$

where $\mathbf{q}$ is the 4x1 quaternion representing the relative attitude of the B frame with respect to the ECI frame, $\dot{\mathbf{q}}$ is the time derivative of the quaternion, $\boldsymbol{\omega}$ is the

3x1 angular velocity vector of the body frame with respect to the inertial frame expressed in the body frame, in rad/s, and $[\boldsymbol{\omega}\times]$ is the 3x3 matrix defined as follows

$$[\boldsymbol{\omega}\times] = \begin{bmatrix} 0 & -\omega_3 & \omega_2 \\ \omega_3 & 0 & -\omega_1 \\ -\omega_2 & \omega_1 & 0 \end{bmatrix} \tag{3.11}$$

One important property of attitude quaternions, is that they are of unit length. Therefore, it is important in simulations to ensure that the initial quaternion is unitary. It is common practice to keep normalizing the quaternions during the numerical integration in order to compensate for small deviations from this unit length. However, within this work it was observed that such deviation was negligible, hence, the normalization was not necessary after the initialization.

3.3.3 Attitude Dynamics

Attitude dynamics, as opposed to attitude kinematics, describe the orientation of the satellite, taking into account the forces and torques that affect it, and can be expressed through the Euler's Rotation Equation as follows:

$$\dot{\boldsymbol{\omega}} = \mathbf{J}^{-1}(-\boldsymbol{\omega} \times \mathbf{J}\boldsymbol{\omega} + \boldsymbol{\tau_{tot}}) \tag{3.12}$$

where $\mathbf{J}$ is the 3x3 inertia tensor of the satellite in kg·m^2, and $\boldsymbol{\tau_{tot}}$ is the 3x1 vector representing the sum of all external torques in N·m, which includes control torques as well as perturbation torques caused by the environment such as solar radiation pressure, gravity gradient, and atmospheric drag.

3.4 Environmental Models

Two environmental models are required for the simulations executed in this thesis: 1) Earth's magnetic field model and 2) atmospheric model. Earth's magnetic field model is required in order to simulate the control torques generated by the magnetorquers, for attitude control. The atmospheric model is required in order

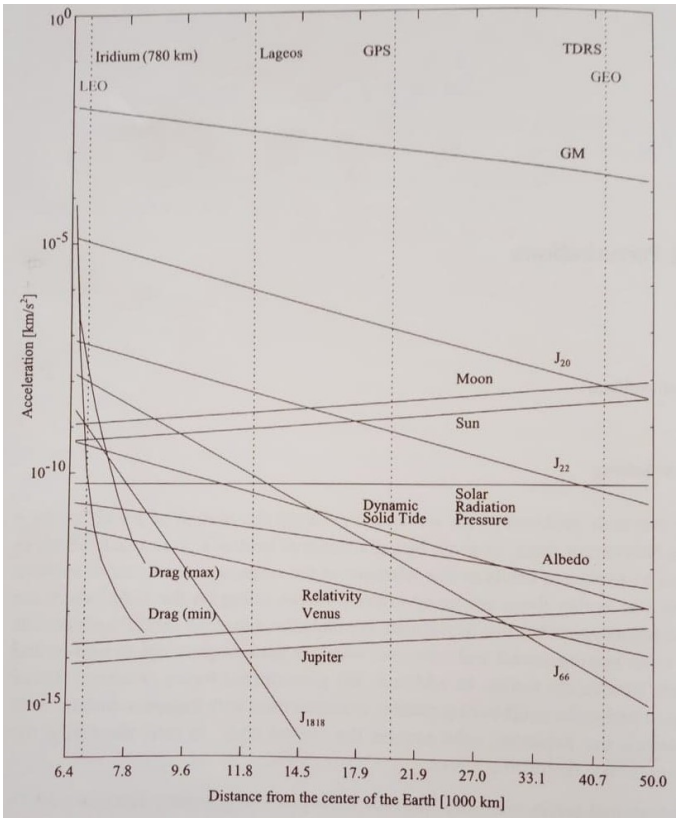

Figure 3.10: Magnitudes of different perturbations of a satellite orbit: GM = regular gravitational force of the Earth; J_{nm} = zonal harmonics; relativity = relativistic deviations. (Walter, 2012).

to simulate the aerodynamic drag and torque forces experienced by the CubeSat during the deorbiting process.

As already mentioned, there are a few other perturbations that can affect the orbit of a satellite around the Earth, such as: solar radiation pressure, the gravitational pulls from the Moon, the Sun, and other planets, and the Albedo effect. However, in LEO environment, where all simulations in this thesis take place, all of these perturbations are orders of magnitude lower than the atmospheric drag, as can be seen in Fig. 3.10, extracted from (Walter, 2012).

While these minor perturbations could be taken into account for even more accurate simulations, Fig. 3.10 suggest their effects can be neglected without any

major impact to the results of our numerical analysis.

It is worth noting that the equations for the other significant accelerations, such as the regular gravitational force of the Earth and the zonal harmonics effect, are already described in Section 3.3.

3.4.1 Earth's Magnetic Field

Earth has a stable and steady magnetic field which, amongst other effects, protects it from solar charged particles. This magnetic field is generated by the iron core at the center of the Earth. Although it presents variations with time, these variations are negligible as compared to the usual time length of a satellite mission. This magnetic field forms what is called a magnetosphere around the Earth. The magnetosphere poses both advantages and disadvantages for satellites around Earth. In one side, it is responsible for trapping Sun's energetic particle in what are called the Van Allen belts. These belts are dangerous in that they represent a risk for the electronics on board unmanned spacecraft, in addition to health risks for astronauts in manned missions. In the other hand, engineers can take advantage of Earth's magnetic field. Actuators can be designed such that they interact with this field, and are capable of generating useful torques, used to control spacecraft orientation in space. While there are a number of magnetic field models, as shown in Table 3.1, the International Geomagnetic Reference Field (IGRF-12) model provided by the International Association of Geomagnetism and Aeronomy (Davis & Tech, 2004) is used in the numerical simulations presented in this work. This model is continuously updated and is the widely accepted standard used to model Earth's magnetic field for aerospace applications. This model is expressed with the following set of equations:

$$B_r = \sum_{n=1}^{\infty}(\frac{R_e}{r})^{n+2}(n+1)\sum_{m=0}^{n}[g_n^m\cos(m\phi)+h_n^m\sin(m\phi)]P_n^m(\theta_c) \tag{3.13a}$$

$$B_\theta = \sum_{n=1}^{\infty}(\frac{R_e}{r})^{n+2}\sum_{m=0}^{n}[g_n^m\cos(m\phi)+h_n^m\sin(m\phi)]\frac{\partial P_n^m(\theta_c)}{\partial\theta c} \tag{3.13b}$$

$$B_\phi = \frac{1}{\sin\theta}\sum_{n=1}^{\infty}(\frac{R_e}{r})^{n+2}\sum_{m=0}^{n}m[g_n^m\sin(m\phi)-h_n^m\cos(m\phi)]P_n^m(\theta_c) \tag{3.13c}$$

Table 3.1: Current geomagnetic models

MODEL	DESCRIPTION
WMM2015v2	The current World Magnetic Model (WMM) is a degree and order 12 core field model based on satellite observations and forecasting the field until Dec 31, 2019
HDGM2019	The High Definition Geomagnetic Model (HDGM) is a global, high resolution model of the Earth's geomagnetic main and crustal field, providing magnetic field values at any point above or below the Earth's surface.
EMM2017	The Enhanced Magnetic Model (EMM) is a degree and order 720 internal field model, resolving magnetic anomalies down to 565 km wavelength.
POMME-10	The Postdam Magnetic Model of the Earth (POMME) is a research model that describes both the internal and the external (magnetospheric) fields, taking into account the variability of the space weather.
IGRF-12	The International Geomagnetic Reference Field (IGRF) is a model describing the core field from 1900 to 2020. It is produced under the auspices of the International Association of Geomagnetism and Aeronomy (IAGA).
MF7	CHAMP satellite based model of Earth's crustal magnetic anomaly resolved to degree 133, wavelengths of 300 km.
NGDC-720	The NGDC-720 model provides a description of the crustal field from ellipsoidal harmonic degree 16 to 719, corresponding to the waveband of 2500 km to 56 km.
EEFM1	The Equatorial Electric Field Model (EEFM) is a satellite based EEF model at 108 km altitude as a function of longitude, local-time, season, solar flux, and lunar local time.
PPEEFM	The Prompt Penetration Equatorial Electric Field Model (PPEEFM) describes how the electric field in the equatorial ionosphere varies as a response to solar wind fluctuations.
EEJM2	The Equatorial Electrojet Model (EEJM) is a satellite derived model of the EEJ magnetic signature as a function of longitude, local-time, season, solar flux, and lunar local-time.

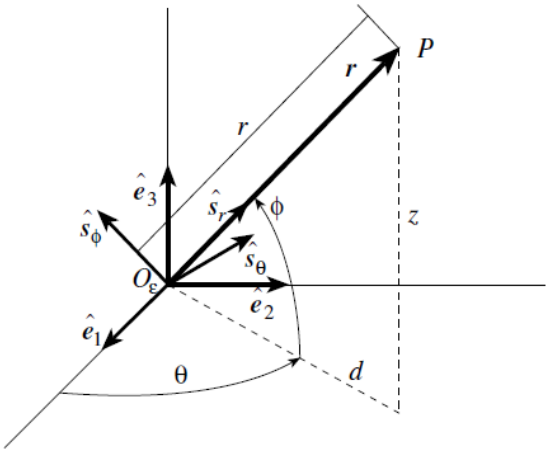

Figure 3.11: Spherical coordinate system (Junkins & Schaub, 2001).

where B_r, B_θ, and B_ϕ are the components of the Earth's magnetic field in spherical coordinates (r,θ,ϕ), see Figure 3.11, in Tesla (T), R_e is the reference radius of the Earth, already defined, g_n^m and h_n^m are the Gaussian coefficients provided by the International Association of Geomagnetism and Aeronomy in Tesla, θ is the latitude in radians, θ_c is the colatitude $(\pi/2 - \theta)$ in radians, ϕ is the longitude in radians, and $P_n^m()$ is a Schmidt quasi-normalized associate Legendre function of degree n and order m.

3.4.2 Atmospheric Model

In order to perform high fidelity deorbiting simulations, it is imperative to count with an accurate atmospheric model in order to account for the atmospheric drag experienced by the CubeSat. Atmospheric conditions vary with different factors such as solar winds, solar cycles, day and night conditions, temperature, etc. All of these conditions would be extremely difficult to account for in simulations. However, similar to geomagnetic models, there are models of the atmosphere that provide a good degree of accuracy. Popular atmospheric models are: US Standard Atmosphere 1976 (NASA, 1976), the International Standard Atmosphere, the Jet standard atmosphere, the NRLMSISE-00 and the Jacchia Reference Atmosphere. Each one of these models are fit for some specific applications. The U.S. Standard

Atmosphere 1976 is the model of choice for space applications. This is due to the fact that it comprises altitudes of up to 1000 km, while the rest of the models are in the range of 100 km. Because of this, it is used to account for the atmospheric drag in the simulations presented in this thesis. This model, amongst other things, provides air densities (ρ) up to 1000 km of altitude, which can be interpolated and plugged into equation 2.1, in order to obtain the aerodynamic forces acting upon the satellite at any given time. Table 3.2 provides an extract of the coefficients provided by this model.

3.5 Summary and Discussions

In this chapter, the theoretical foundations for the development of this work have been introduced. Physical laws that govern both the orbital as well as the rotational motion of an artificial satellite have been presented in the form of Ordinary Differential Equations (ODEs). These ODE's will be key while developing and analysing the algorithms introduced in this thesis, as well as being the tool which allows the numerical simulations used in order to assess the effectiveness and efficiency of said algorithms.

Different Earth's magnetic field models and atmospheric models are also discussed, and IGRF-12 and U.S. Standard Model 1976 are chosen respectively for this work. Earth's magnetic field model plays a primary role in the development of this thesis. First of all, it provides the medium by which control torques can be applied to the CubeSat, being this the only mechanism for attitude control considered in this work. In the case of the atmospheric model, it is also paramount in order to evaluate to a great accuracy the rate of orbital decay through numerical analysis, since in LEO, this is one of the main orbital perturbations experienced by a satellite.

Table 3.2: Extract of the U.S. Standard Atmosphere 1976 (NASA, 1976)

Altitude, km	Temperature, °C	Pressure, mb	Density, kg/m^3
0	15	1013.25	1.225
1	8.5	898.746	1.11164
2	2	794.952	1.00649
3	-4.5	701.085	9.09122×10^{-1}
4	-11	616.402	8.19129×10^{-1}
5	-17.5	540.199	7.36116×10^{-1}
6	-24	471.810	6.59697×10^{-1}
7	-30.5	410.607	5.89501×10^{-1}
8	-37	355.998	5.25168×10^{-1}
9	-43.5	307.425	4.66348×10^{-1}
10	-50	264.363	4.12707×10^{-1}
15	-56.5	120.446	1.93674×10^{-1}
20	-56.5	54.7489	8.80349×10^{-2}
25	-51.5	25.1102	3.94658×10^{-2}
30	-46.5	11.7187	1.80119×10^{-2}
40	-22.1	2.77522	3.85101×10^{-3}
50	-2.5	7.59448×10^{-1}	9.77525×10^{-4}
60	-27.7	2.03143×10^{-1}	2.88321×10^{-4}
70	-55.7	4.63422×10^{-2}	7.42430×10^{-5}
80	-76.5	8.86280×10^{-3}	1.57005×10^{-5}
90	-86.28	1.8359×10^{-3}	3.416×10^{-6}
100	-78.07	3.2011×10^{-4}	5.604×10^{-7}
200	581.41	8.4736×10^{-7}	2.541×10^{-10}
300	702.86	8.7704×10^{-8}	1.916×10^{-11}
400	722.68	1.4518×10^{-8}	2.803×10^{-12}
500	726.09	3.0236×10^{-9}	5.215×10^{-13}
600	726.70	8.2130×10^{-10}	1.137×10^{-13}
700	726.82	3.1908×10^{-10}	3.070×10^{-14}
800	726.84	1.7036×10^{-10}	1.136×10^{-14}
900	726.85	1.0873×10^{-10}	5.759×10^{-15}
1000	726.85	5.138×10^{-11}	3.561×10^{-15}

Chapter 4

Magnetic Field Tracker

4.1 Introduction

In this chapter, a new attitude control law, and a corresponding algorithm for deorbiting a CubeSat are presented. The controller's operation is based in tracking the instantaneous geomagnetic field vector. It must be noted that a similar algorithm was proposed by (Jan & Tsai, 2005), in the sense that it tracks the local magnetic field. However, it was only proposed for initial attitude stabilization purposes. Further differences exist in the fact that the algorithm proposed in this chapter relies on scalar gains, as opposed to vector gains. Also, this algorithm relies on a normalized magnetic field vector, as opposed to the one proposed in (Jan & Tsai, 2005). Also, here we propose the use of three magnetorquers, as opposed to two magnetorquers. And finally, the stability and robustness of our controller are proven in this chapter, aspects that were not studied in the aforementioned work.

The algorithm relies on a model of the Earth's magnetic field. The tracking action is enabled by a combination of magnetometers, in order to sense the magnetic field vector $\mathbf{b}$ in the B frame, and magnetorquers, which provide the required torques in order to control the attitude of the CubeSat. The Earth's magnetic field model is IGRF-12, discussed in Chapter 3. Even though there is no full attitude determination, a relationship can be established between the direction of the thrust vector, and the orbital velocity vector. This relationship allows enough

knowledge in order to determine when the thrusters can be turned on and off such that orbital energy is decreased continuously.

The control law is derived together with an explanation of the thrusting algorithm. A deorbiting scenario is designed in order to execute full non-linear simulations in MATLAB/Simulink, and in this way demonstrate the effectiveness and performance of the proposed system. The performance of the five electric engines discussed in Chapter 2 is explored, and deorbit times for each one are presented. Results allow for a comparison between this algorithm and alternative technologies such as sails, inflatables, and electric tethers.

The closed-loop system with the geomagnetic field tracker is derived, which is given by a linear periodically time-varying system. Since the system turns into a linear periodically time varying its stability analysis can be performed using the Floquet theorem (Khalil, 1996).

Finally, the robustness analysis is provided through the means of Monte Carlo simulations. One thousand scenarios are executed, and the algorithm is successful in deorbiting the CubeSat each time, which demonstrates the effectiveness of the algorithm even in the presence of model uncertainties. For the robustness analysis, only electrospray engines are considered, since that suffices for the purposes of the test. A range of deorbit times using electrospray engines is thus obtained.

4.2 Attitude Control Law

In order to deorbit a satellite using a thruster, it first needs to be oriented in a proper direction. This ensures that the thrust vector opposes the direction of the orbital velocity, effectively decreasing the satellite's orbital energy. The control algorithm here described aligns the thruster carrying axis of the satellite with the geomagnetic field vector, using magnetorquers. Once aligned, the thruster can dissipate the kinetic energy of the CubeSat during half of its orbit. Only one attitude sensor - the magnetometer - is required, which is relatively small, compact, and cheap; and it is integrated in many CubeSats missions. This will provide the magnetic field vector reading in the B frame. The orbital position and velocity vectors in the ECI frame are provided by a GPS receiver. The GPS receiver is

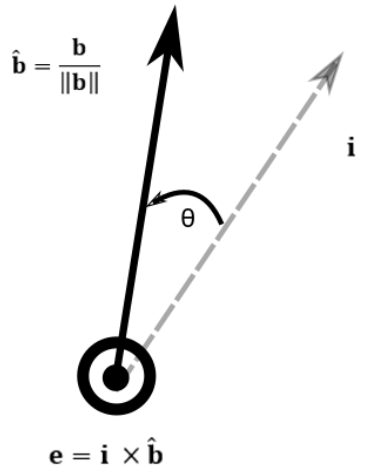

Figure 4.1: The objective of the torque is to align the **i** axis of the CubeSat with the normalized magnetic field vector $\hat{\mathbf{b}}$

needed to determine when the thruster must be activated and deactivated in order to deorbit the satellite. The control law is derived next.

The objective of the attitude control algorithm is to align the x body axis with the local magnetic vector. To accomplish this, the desired torque is given by

$$\boldsymbol{\tau_{des}} = k_1' \mathbf{e} \tag{4.1}$$

where k_1' is a control gain, and:

$$\mathbf{e} = \mathbf{i} \times \hat{\mathbf{b}} \tag{4.2}$$

i is the unit vector toward the x direction of the B frame; and $\hat{\mathbf{b}}$ is the normalized magnetic field in the B frame, which is equal to $\mathbf{b}/\|\mathbf{b}\|$, where $\|\mathbf{b}\|$ is the magnitude of **b**. Figure 4.1 offers a graphical depiction of the desired torque.

From Fig. 4.2, the control magnetic dipole can be derived geometrically. First note that:

$$\mathbf{e} = (\hat{\mathbf{b}} \times \mathbf{e}) \times \hat{\mathbf{b}} \tag{4.3}$$

substituting Eq. (4.3) into Eq. (4.1) we then have:

$$\boldsymbol{\tau_{des}} = k_1' \mathbf{e} = k_1' (\mathbf{i} \times \hat{\mathbf{b}}) \tag{4.4}$$

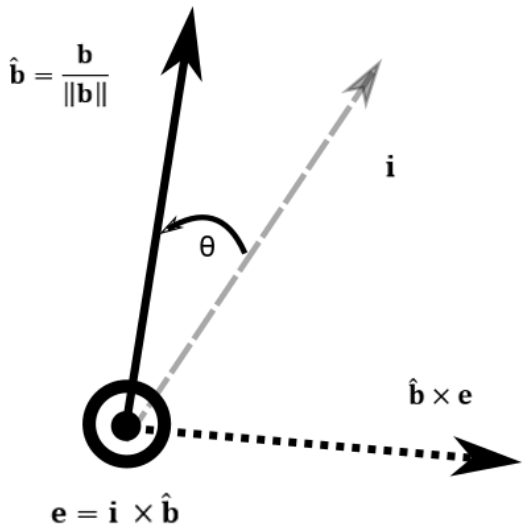

Figure 4.2: Geometrical derivation of the control magnetic dipole.

defining $k_1 = k_1'\|\mathbf{b}\|$ we have:

$$\boldsymbol{\tau_{des}} = k_1\|\mathbf{b}\|(\hat{\mathbf{b}} \times \mathbf{e}) \times \hat{\mathbf{b}} \tag{4.5}$$

and finally:

$$\boldsymbol{\tau_{des}} = k_1(\hat{\mathbf{b}} \times \mathbf{e}) \times \mathbf{b} \tag{4.6}$$

The torque generated by magnetorquers is given by

$$\boldsymbol{\tau} = \mathbf{m} \times \mathbf{b} \tag{4.7}$$

where $\boldsymbol{\tau}$ is the torque in N $\cdot$ m, $\mathbf{m}$ is the 3×1 magnetic dipole vector produced by the magnetic torquers in A·m^2, and $\mathbf{b}$ represents the 3×1 Earth's magnetic field vector in Tesla.

By comparison of Eq. (4.6) and Eq. (4.7) we can derive that the control magnetic dipole takes the form of:

$$\mathbf{m_{ctrl}} = k_1[\hat{\mathbf{b}}\times]\mathbf{e} \tag{4.8}$$

Including additional damping effect, the geomagnetic field tracker dipole becomes

$$\mathbf{m_{ctrl}} = k_1[\hat{\mathbf{b}}\times]\mathbf{e} - k_2\frac{d^B}{dt}\hat{\mathbf{b}} \tag{4.9}$$

where k_1 and k_2 are the control gains to be designed; and d^B/dt is the time derivative in the B frame, which could be implemented using the finite difference approximation the same way that the B-dot controller is implemented (Stickler & Alfriend, 1974).

Equation (4.9) can be directly implemented with a numerical differentiator to approximate the time derivative of the geomagnetic field vector measurement. If a rate gyroscope sensor is available, then $d^B(\hat{\mathbf{b}})/dt$ can be replaced by $[\hat{\mathbf{b}}\times]\boldsymbol{\omega}$. Hence,

$$\mathbf{m_{ctrl}} = k_1[\hat{\mathbf{b}}\times]\mathbf{e} - k_2[\hat{\mathbf{b}}\times]\boldsymbol{\omega} \tag{4.10}$$

The attitude control portion of the deorbiting system has now been described. Now, in the next section, we shall see how this controller can be harnessed by a simple algorithm, in order to deorbit a satellite, more specifically, a CubeSat.

4.3 Deorbiting Algorithm

Once the CubeSat's x face is tracking the magnetic field vector, it can be determined when to activate the thrusters in order to cause the loss of orbital energy. This knowledge comes from the fact that the magnetic field vector is available in the LVLH frame in the form $\mathbf{b^{lvlh}} = (b_x^{lvlh}\ b_y^{lvlh}\ b_z^{lvlh})^T$, where $(\cdot)^T$ is the transpose. The relationship between the orbital velocity vector $\mathbf{v}$ and the x axis in the LVLH frame, gives knowledge of when the thrust vector opposes the direction of travel, at least at some degree. When the component b_x^{lvlh} is positive, it implies the thruster points in the direction of travel as shown in Fig. 4.3. In this scenario, the thrusters should be fired. Otherwise, the thrusters should be turned off. In Fig. 4.3, it is important to clarify that the x axis of the LVLH frame does not necessarily coincide with the velocity vector; however, in a quasi-circular orbit, this is a reasonable simplification.

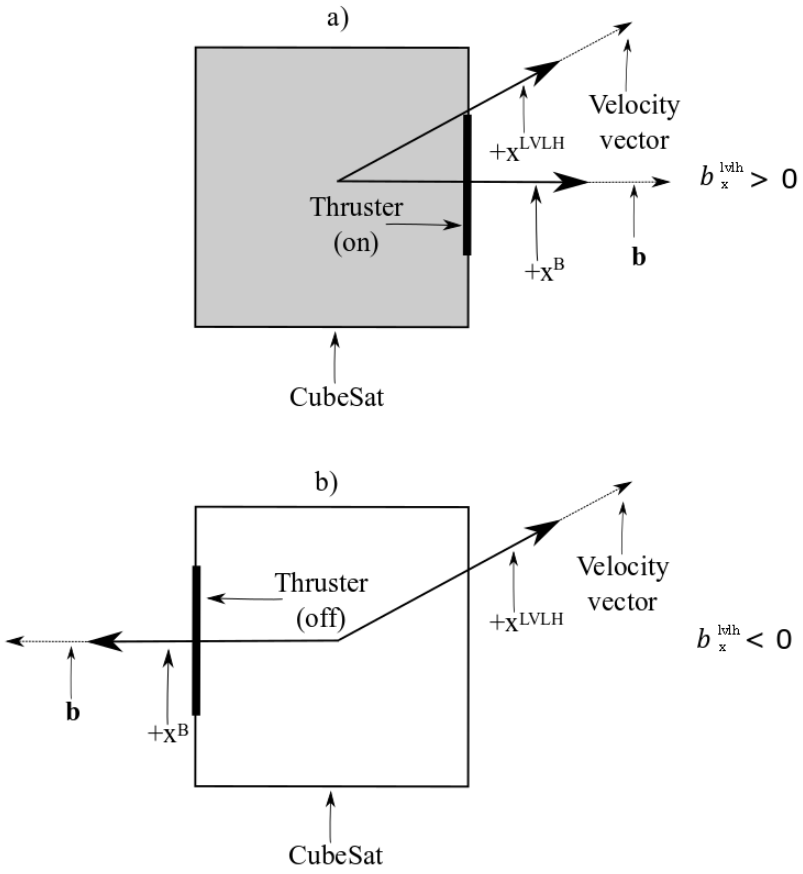

Figure 4.3: CubeSat attitude scenarios, showing attitudes at which the thruster is a) on or b) off.

This deorbiting algorithm can also be expressed very easily by the following equation:

$$\text{thrust} = \begin{cases} \text{on}, & \text{if } b_x^{lvlh} > 0 \\ \text{off}, & \text{otherwise} \end{cases} \tag{4.11}$$

Figure 4.4 shows the CubeSat alignment with the geomagnetic field vector, as well as the relative attitude to the spacecraft velocity vector, which determines when the thrusters - mounted in the x face of the satellite - can be fired and when they should be turned off. An interesting instance is observed in Fig. 4.4

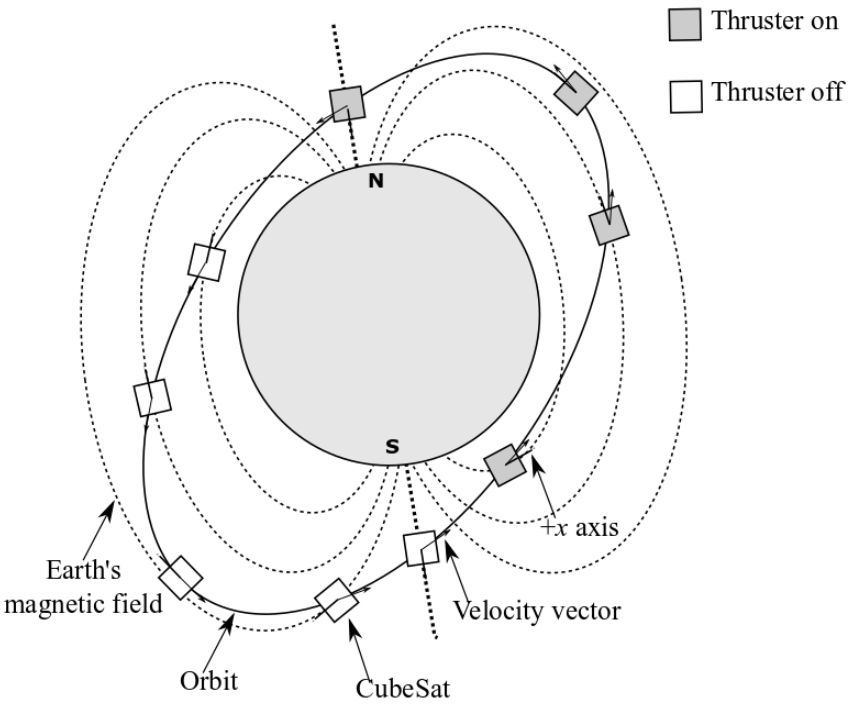

Figure 4.4: CubeSat x axis aligned with magnetic field and the relative attitude with respect to the velocity vector.

when the satellite is above the North Pole. Intuitively, it might seem that having the thruster activated over the North Pole would push the satellite upward, i.e., gaining altitude. However, the objective of the deorbiting algorithm is to dissipate the kinetic energy of the satellite. This is achieved whenever the thrust vector has a component that opposes the velocity vector.

4.4 Deorbiting Scenario

Both the attitude control law and the deorbiting algorithm have now been explained. Let us define an scenario such that the effectiveness and performance of this approach can be put to test by means of numerical simulations. The first variable to be tested is the tracking error of the magnetic field tracking algorithm,

which is a critical measurement for the effectiveness of the deorbiting algorithm. The deorbiting rates are also evaluated.

Non-linear simulations were performed to evaluate the tracking error of the algorithm, which is the angle difference between the magnetic field vector and the x body axis of the satellite. In all the simulations within this chapter, we consider a realistic and standard nanosatellite mission configuration. It consists of a 3U CubeSat equipped with three orthogonal magnetorquers; a three-axis magnetometer; a three-axis rate gyroscope; a GPS receiver; and an electric engine for propulsion. The thruster vector direction is assumed to be aligned with the x face of the satellite. The CubeSat has a mass of 3.5 kg, and the diagonal terms of the inertia tensor are diag[0.01, 0.0506, 0.0506] kg $\cdot$ m^2. No deployable solar panels are considered, and differential aerodynamic torques are neglected. For the sake of simplicity, the drag force is computed assuming the minimal area face pointing in the direction of travel. This is the worst case scenario, as it will generate the minimum amount of drag. It has an initial orbital altitude of 900 km, in a near-circular orbit. The inclination is set to 65°. The control gains are tuned such that $k_1 = 0.5$ and $k_2 = 25$ through multiple trial-and-error procedures. Initially, the gains are varied to identify a coarse range of the feasible gains, and a fine tuning is performed to determine the final gains in aligning the body axis to the magnetic field vector. It is also important to mention that, in practice, magnetometers and magnetorquers cannot be activated at the same time, because the magnetometers measurements would be affected by the magnetorquers' dipole. Therefore, a duty cycle is implemented in which, during a period of 5 s, magnetorquers are active for the first 4 s and magnetometers are active for the remaining 1 s. All simulations were performed using MATLAB/Simulink with the default numerical integration algorithm ODE4 and the relative tolerance of 0.001.

These models do not take into account aerodynamic torques, gravitational pulls from celestial bodies other than the Earth, or solar pressure, as these forcers are orders of magnitude smaller than the dominating aerodynamic drag, as discussed in Chapter 3. Thus it is not expected that these factors can have a major impact in the performance of the algorithms. It is assumed that there are no failures in the sensors and actuators. It is also assumed that there is enough fuel during

Table 4.1: Electric Engine Types

Engine	Thrust mN	Power W	Fuel	Mass g	Specific Impulse s
Electrospray	1.8	25	Ionic Salt	1400	1500
Micro Pulsed Plasma Thruster	0.04	2	Teflon	280	600
Hall Effect Thruster	0.1	3	Xenon	1000	1500
CubeSat Ambipolar Thruster (Sheehan *et al.*, 2015)	0.5	50	Xenon	<1000	400
Micro Cathode Arc Thruster (Keidar, 2016)	0.05	0.1	Solid fuel	200	2000

the deorbiting operation, as well as that the batteries are able to provide enough energy during eclipses.

This scenario was also simulated in order to test the performance of the proposed deorbiting algorithm. Aerodynamic drag accelerations are taken into account for this numerical analysis using the U.S. Standard Atmosphere, 1976 model (NASA, 2009). Gaussian variational equations were used in order to compute the evolution of the orbital parameters (Walter, 2012). The deorbit process was simulated for the five different types of electric engines shown in Table 4.1. The time span for each simulation scenario is 20 days, unless the deorbiting operation is achieved in less time.

The relevant results of this deorbiting scenarios are presented in the next section.

4.5 Simulation Results

4.5.1 Results without J_2 Term Effects

Figure 4.5 shows the evolution of the tracking angle error through the whole deorbiting process with the electrospray thruster. It can be seen that, after an initial error of about 100°, the CubeSat is able to track the magnetic vector within an accuracy of roughly 5 deg. This small tracking error is attributed to two factors; 1)

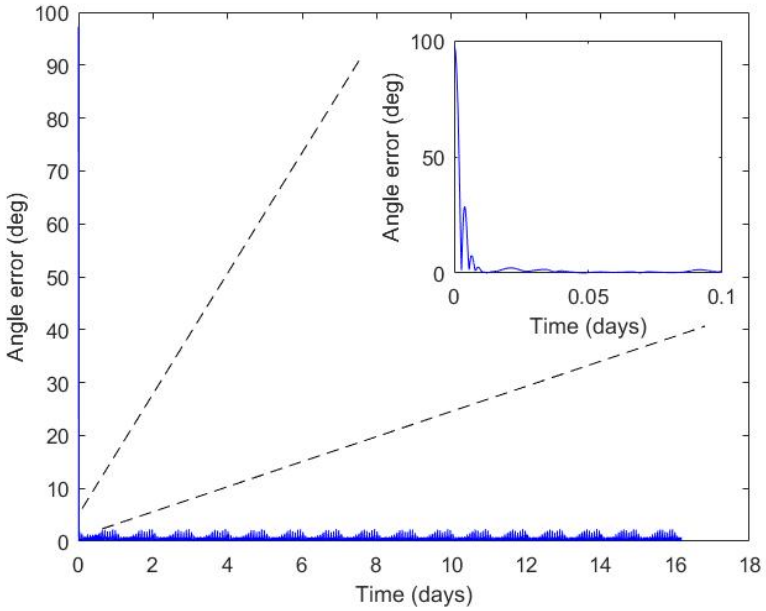

Figure 4.5: Magnetic vector tracking error.

the CubeSat is underactuated, since the magnetorquers cannot generate control torques in any arbitrary direction and, 2) the duty cycle that has to be implemented, which implies that the action of the magnetorquers cannot be continuous. High pointing accuracy is however not critical for the deorbit phase of the mission; therefore, this performance is acceptable.

Figure 4.6 shows the evolution of the orbital altitudes for each of the five engine scenarios. The first effect that is apparent from these charts is that the eccentricity of the orbit is gradually increased. This comes from the fact that the thrust is applied during only one-half of the orbit. It also can be seen from Fig. 4.6, in the electrospray case, that once the perigee of the orbit reaches denser layers of the atmosphere, the orbit quickly falls into a critical altitude of around 100 km, which is when the CubeSat can be considered to be deorbited.

The deorbit times are inversely proportional to the thrust that the engines can provide. The better performance is obtained with electrospray engines, with a deorbit time of roughly 16 days. It is followed by the CubeSat ambipolar thruster that decreases the perigee of the satellite by about 250 km in 20 days. An im-

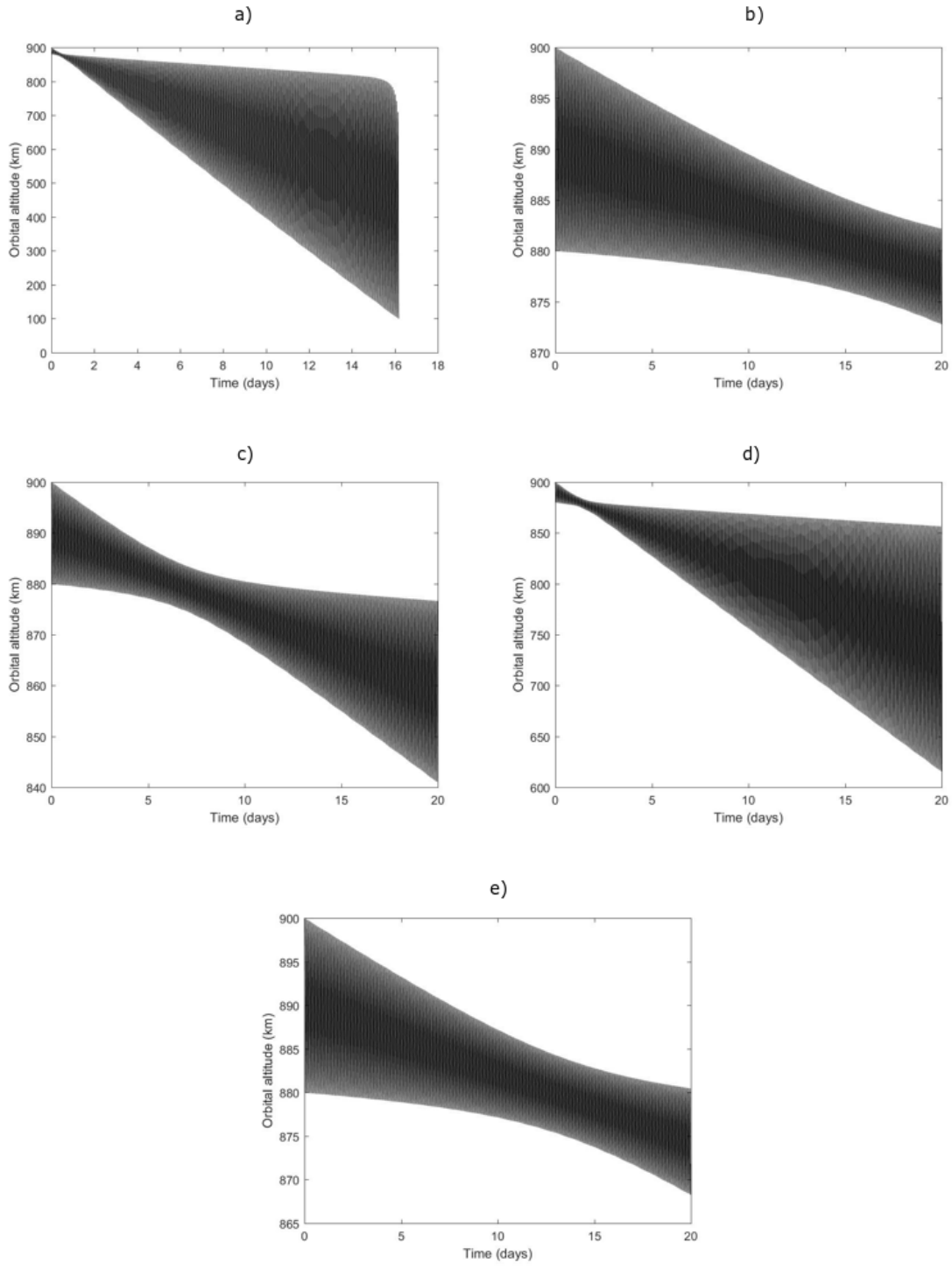

Figure 4.6: Deorbiting rates a) Electrospray thruster; b) Micro Pulsed Plasma Thruster; c) Hall Effect thruster; d) CubeSat Ambipolar thruster; and e) Micro Cathode Arc thruster.

portant aspect to take into account here is the operational lifetime of each engine. This will determine if the engine can be active during the whole deorbit operation. Otherwise, it can only be used to lower the perigee to an altitude at which aerodynamic drag can speed up the deorbiting the satellite. According to the references in Table 4.1, the electrospray engine has a lifetime of about 650 h, which would be enough to carry the entire deorbit operation. In the case of the micropulsed plasma thruster, only state-of-the-art technology would allow a decrease in the perigee of a 3U CubeSat by about 40 km. Further advancements in this specific technology are necessary for their practical use in deorbit operations. Finally, for Hall effect thrusters, it is claimed that they are expected to be able to deorbit a 3U CubeSat from an initial orbit of 750 km. Although no mention of an algorithm is made, this gives confidence that the application of this type of engine to the deorbit problem is practical. No information regarding the lifetime of the CubeSat ambipolar thruster and microcathode arc thruster was found.

Another interesting aspect to look at is the evolution of the semi-major axis. Figure 4.7 depicts this metric for the electrospray scenario, where a step pattern can be observed. This is also an effect of the thrust being applied during only half of the orbit. It is important to notice that during the periods where the thrusters are turned off, the semi-major axis presents a flat behaviour. This is due to the fact that J_2 orbital perturbation was not taken into account for these simulations. The addition of this term would simply add a sinusoidal component to the semi-major axis. It would not affect the deorbit times in a sensitive way, as will be seen in the next section.

The system state and control inputs for the electrospray scenario case are shown Figs 4.8-4.12. Figure 4.8 shows the quaternion evolution. As shown in Fig. 4.9, the angular rates are kept at low values, including ω_x, which is an axis where little or no control torques can be applied. Figure 4.10 depicts the control magnetic dipoles, it can be seen that, after an initial saturation (± 0.2 A $\cdot$ m^2) in m_x and m_z, the control action is very small during the rest of the process: on the order of 0.02 A $\cdot$ m^2. As expected, m_x control action is virtually zero once the satellite is tracking the magnetic vector, as it would be unable to produce useful torque. Figure 4.11 shows a magnification of the control dipole such that the initial saturations can

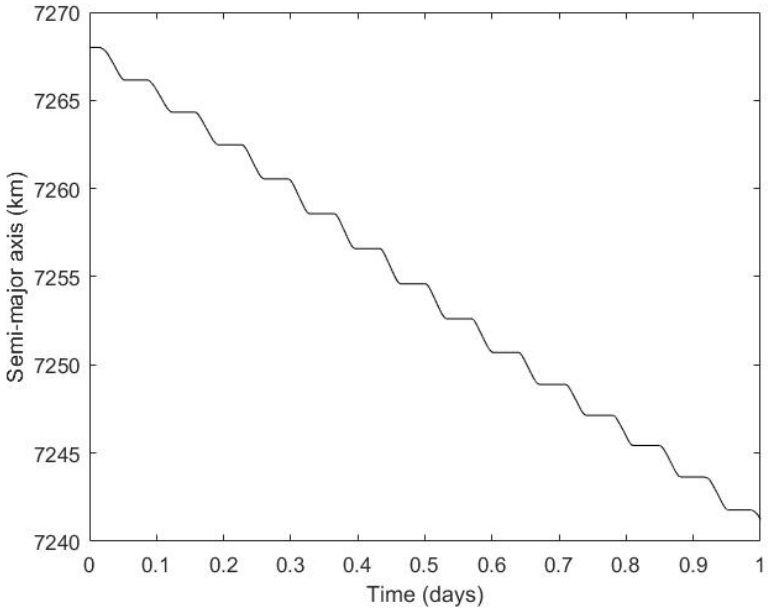

Figure 4.7: Semi-major axis evolution using electrospray thruster.

be better observed. Finally, Fig. 4.12 shows the action of the thruster, in which the thrusters are only active during half the orbital period.

4.5.2 Results with J_2 Term Effects

The performance of the algorithm is evaluated with the effect of taking into account the accelerations caused by Earth's oblateness, specifically the term J_2. Experimental scenario described in Section 4.4 was executed again, but now introducing the effects of the J_2 term. Figures 4.13 to 4.19 show the results of this experiment, where it can be concluded that these accelerations have no noticeable impact over the effectiveness and performance of the geomagnetic field tracking algorithm.

Firstly, let us focus our attention in Fig. 4.13. There is no perceptible difference to the results shown in Fig. 4.5. The pointing error is still maintained within 5°. This behaviour is also expected, as one would predict that the J_2 term would have an effect on the translational dynamics, but not so much in the rotational dynamics of the satellite. This same observation goes for Fig. 4.15 and Fig. 4.16.

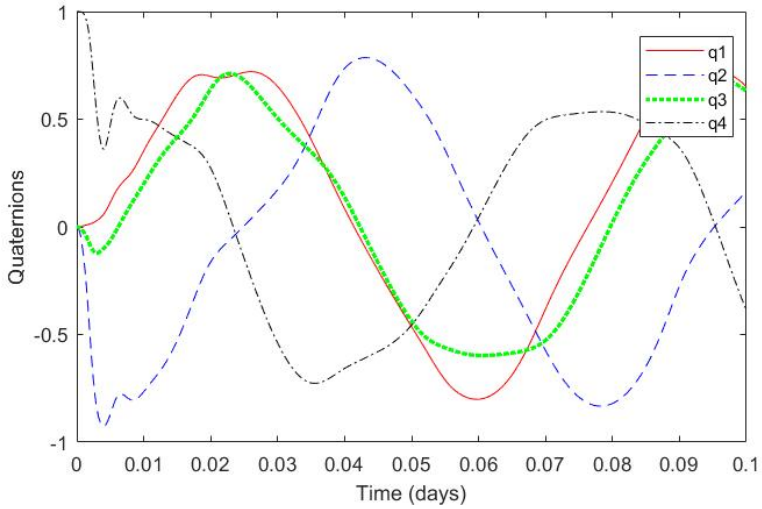

Figure 4.8: CubeSat attitude in quaternions.

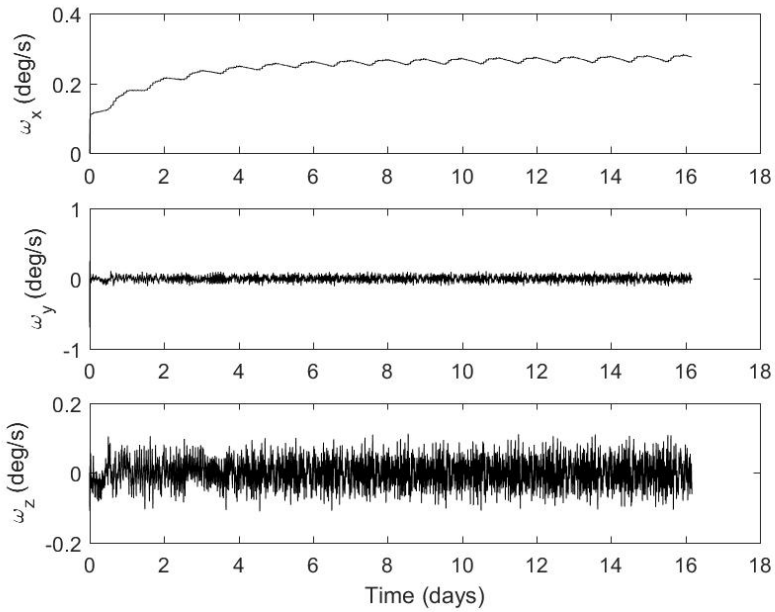

Figure 4.9: CubeSat angular velocities.

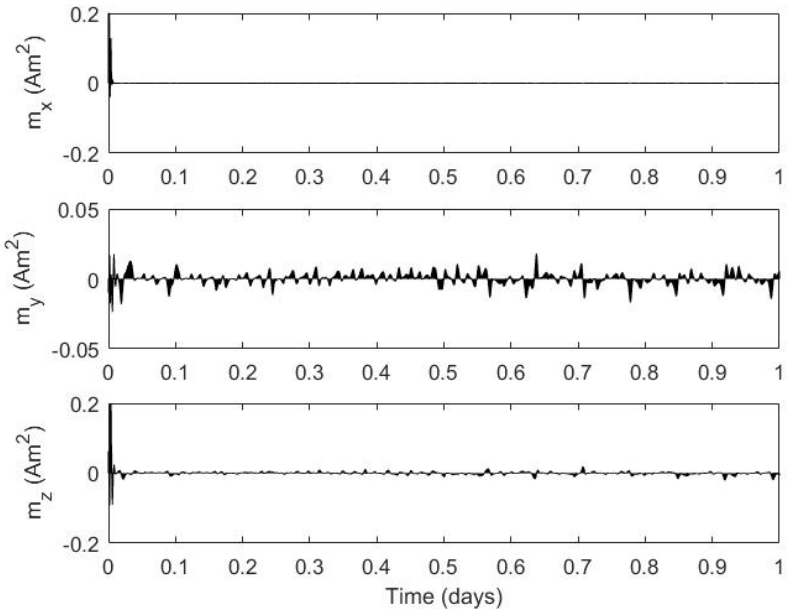

Figure 4.10: Control magnetic dipoles.

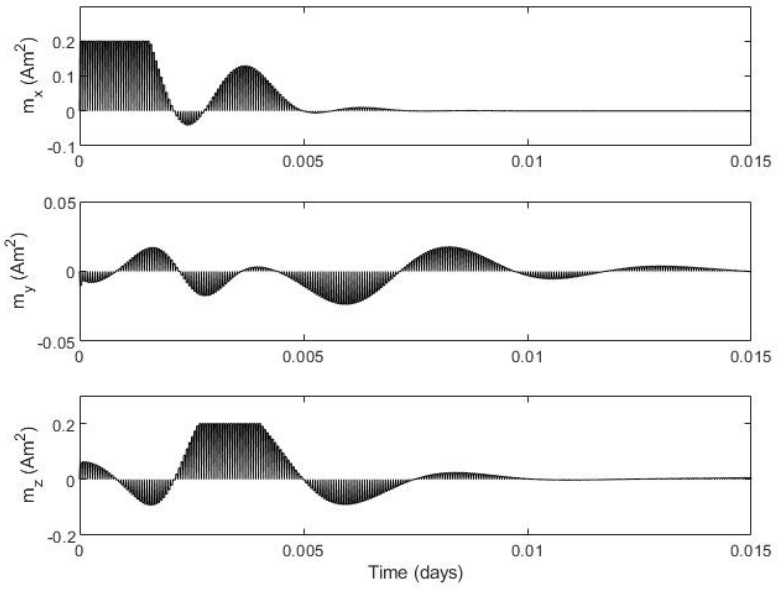

Figure 4.11: Control magnetic dipoles zoom.

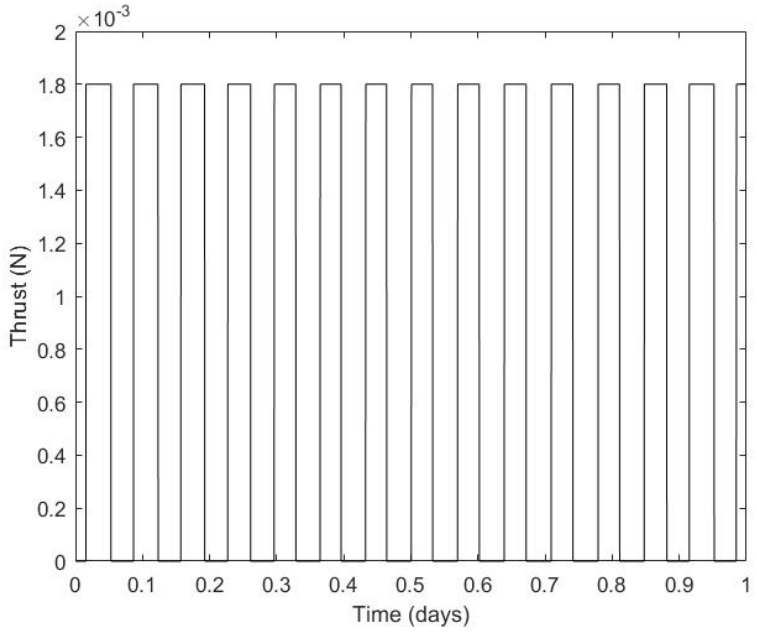

Figure 4.12: Thruster activation.

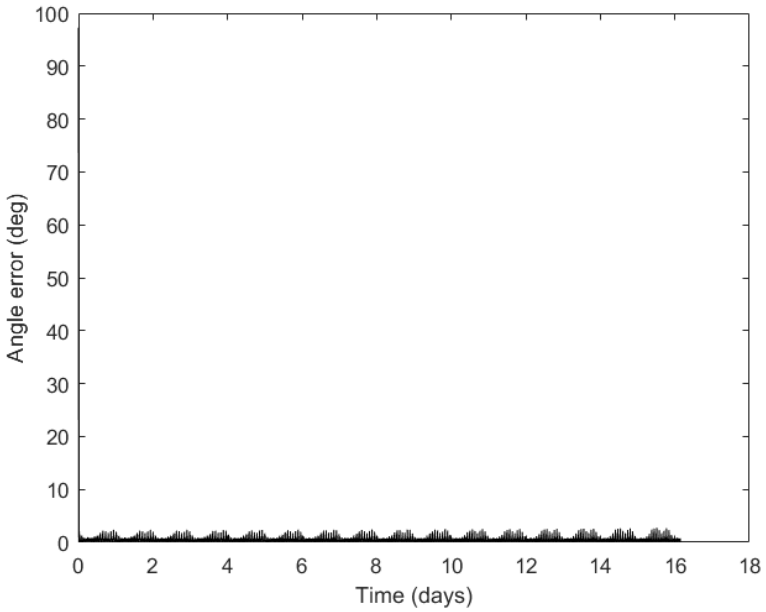

Figure 4.13: Angle error with J2 term effects.

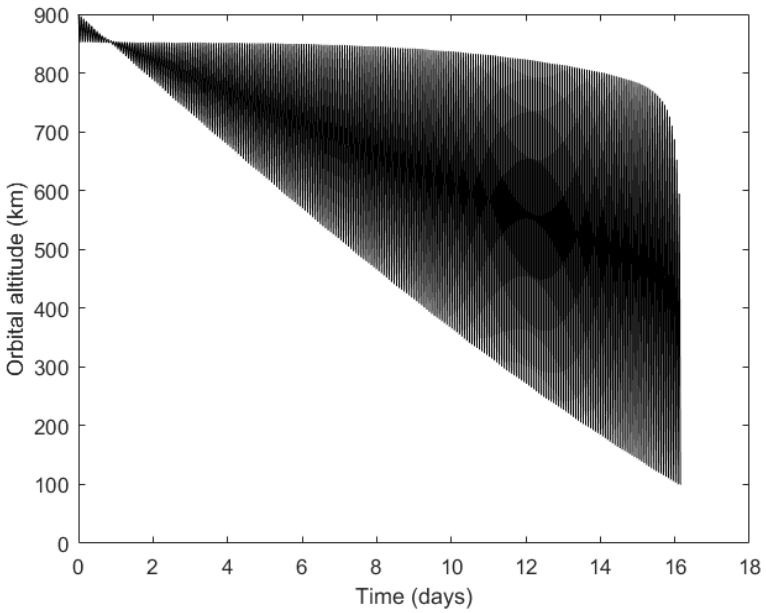

Figure 4.14: Orbital altitude with J2 term effects.

In Fig. 4.14 the effects of the J_2 can be observed more clearly, when compared to Fig. 4.6, as the perigee and apogee have variations from one case to the other. However, in terms of deorbiting time, the effects are negligible. In the case of angular velocities, when comparing Fig. 4.9 and 4.15 no significant differences can be observed. Likewise, it can be seen how Fig. 4.8 and 4.16 are practically identical. Again, the orbital acceleration play little to no role in the rotational dynamics of the CubeSat. In the case of the control magnetic dipoles, they are found to be also practically identical when looking at Fig. 4.10 and 4.17.

As expected, the semi-major axis orbital parameter is the one more affected by the J_2 term, since it introduces a sinusoidal component to this parameter, with half the orbital period. This effect can be seen in Figure 4.18, and more clearly, in the zoom of shown in Figure 4.19. While the sinusoidal effect is noticeable, it is clearly seen that this has no perceptible effect over the effectiveness and performance of the algorithm, in terms of deorbiting time.

After analysing these results, it is clear that the algorithm is robust enough to overcome the effects of the J_2 term induced accelerations, and this gives more

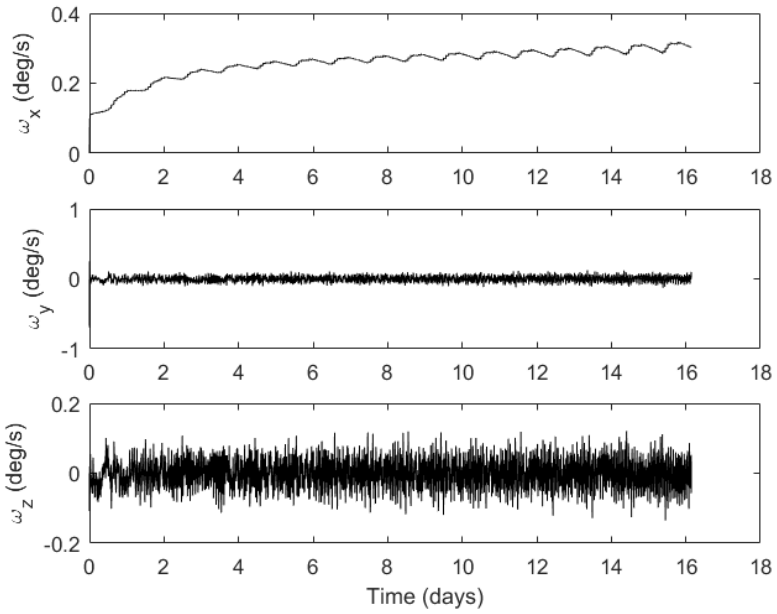

Figure 4.15: Angular velocities with J2 term effects.

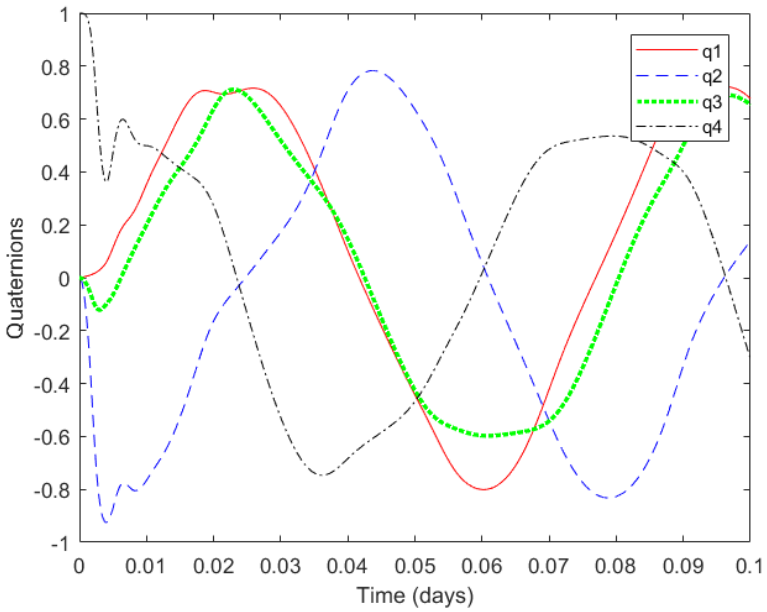

Figure 4.16: Attitude with J2 term effects.

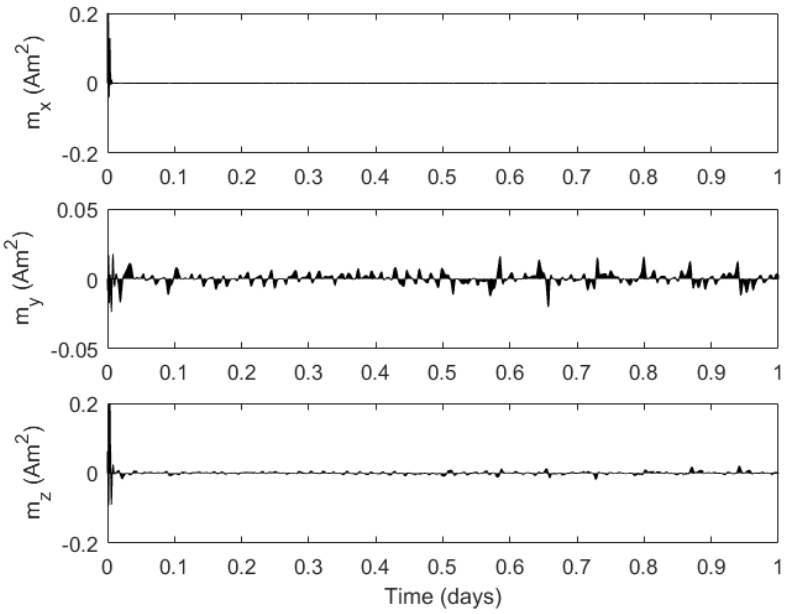

Figure 4.17: Magnetic dipoles with J2 term effects.

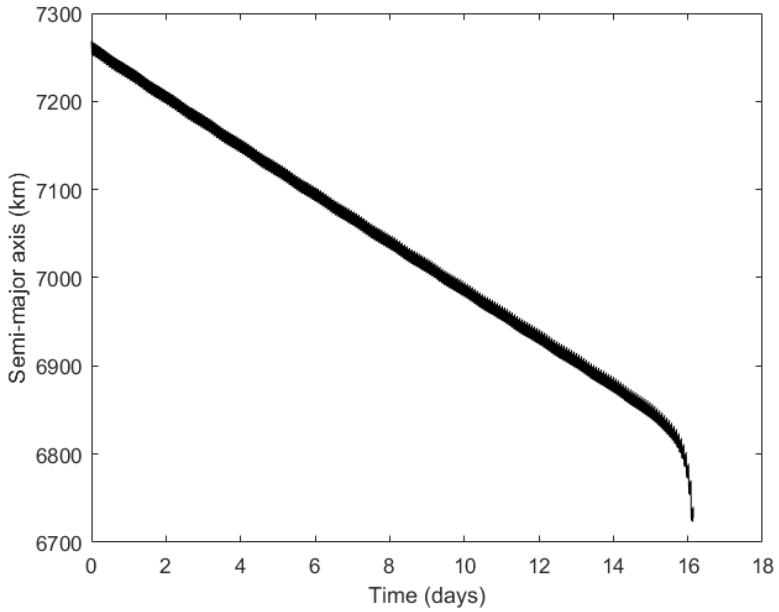

Figure 4.18: Semi-major axis with J2 term effects.

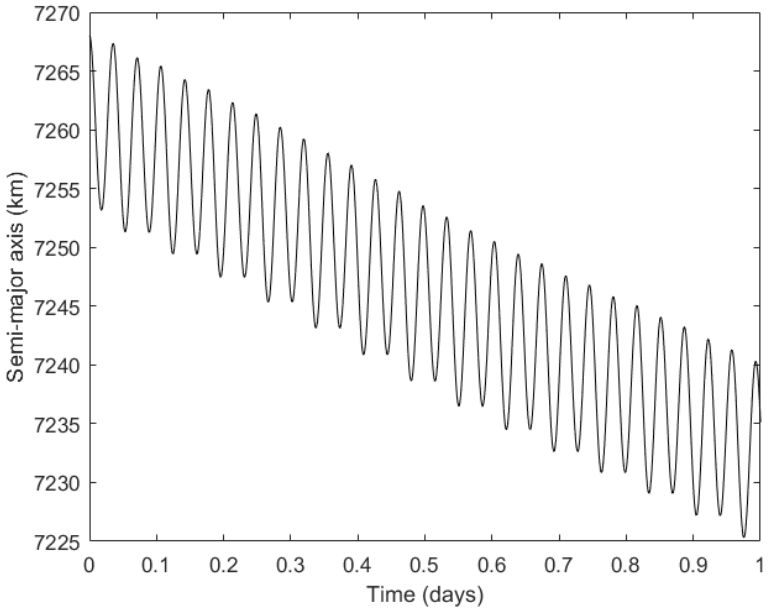

Figure 4.19: Semi-major axis zoom with J2 term effects zoom.

confidence in its practicality to be implemented in real life missions.

4.6 Energy

One of the important aspects to look at when evaluating this algorithm, is the energy consumption, since CubeSats are usually in a budget when it comes to this aspect. According to Table 4.1, electrospray engines are in the middle range regarding power consumption, of the five electric engines considered in this work. Therefore it is taken as a reference in order to evaluate the feasibility of real life implementations of this algorithm in terms of energy consumption.

In this section, the energy consumption of magnetorquers as well as the engine itself is evaluated. The electric consumption of the rest of the CubeSat subsystem such as, on board computer, communications, data handling, etc., are not considered. Most of these subsystems are expected to be inactive during the deorbiting phase, therefore, it is not expected that they could have a major impact in energy consumption during this stage of the mission.

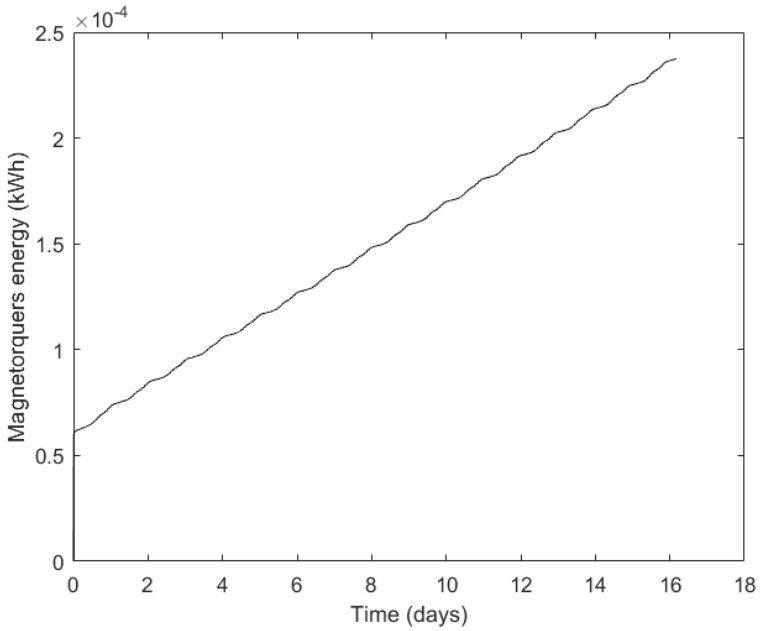

Figure 4.20: Magnetorquer energy consumption.

Magnetorquer energy consumption for the whole deorbiting phase in the electrospray scenario is depicted in Fig. 4.20. It can be seen that the energy consumption is in the order of 2.5×10^{-4} kWh. It experiences a period of rapid energy consumption when the algorithm is first activated, since this is the period when the major deviation in attitude has to be corrected. After this stage is surpassed, the magnetorquers consume a steady amount of energy, until the re-entry of the CubeSat to the atmosphere.

Figure 4.21 shows that the energy consumed by the thrusters much more considerable, reaching a value of around 5 kWh. Figure 4.22 shows a zoom of the engine energy consumption. It is clearly seen how the thrusters only consume energy during half of each orbit, being turned off for the rest of it. This consumption is considered feasible for a real life application since 3U CubeSats can usually cover this demand of power generation (20-30 W) (Poghosyan & Golkar, 2017).

Finally, Figure 4.23 shows the total energy consumption, where naturally the energy consumption of the engines dominates.

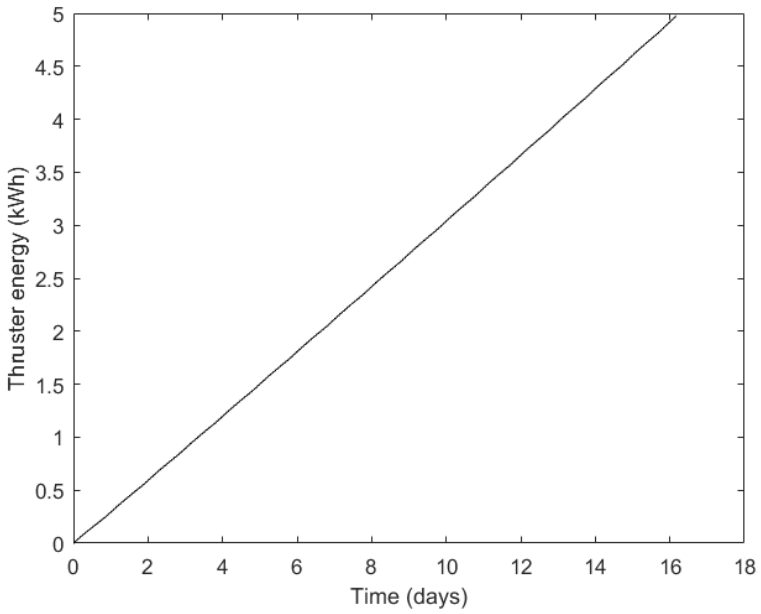

Figure 4.21: Thruster energy consumption.

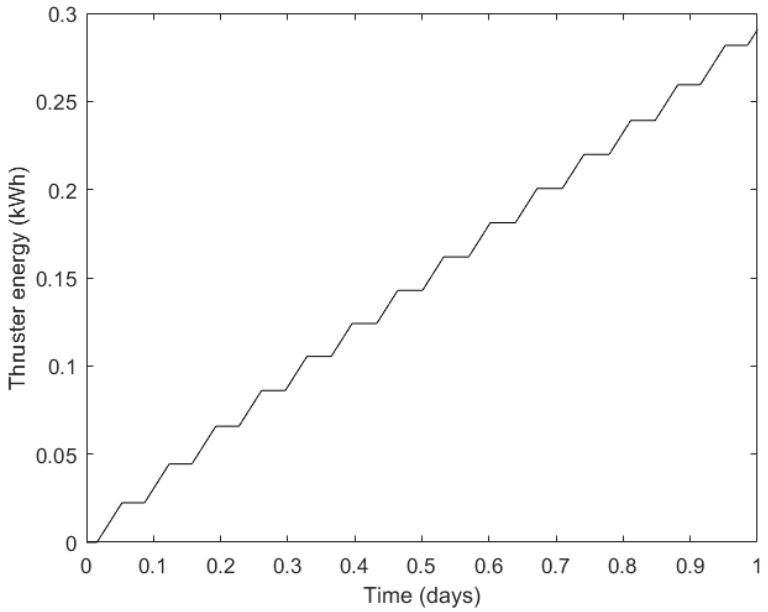

Figure 4.22: Thruster energy consumption zoom.

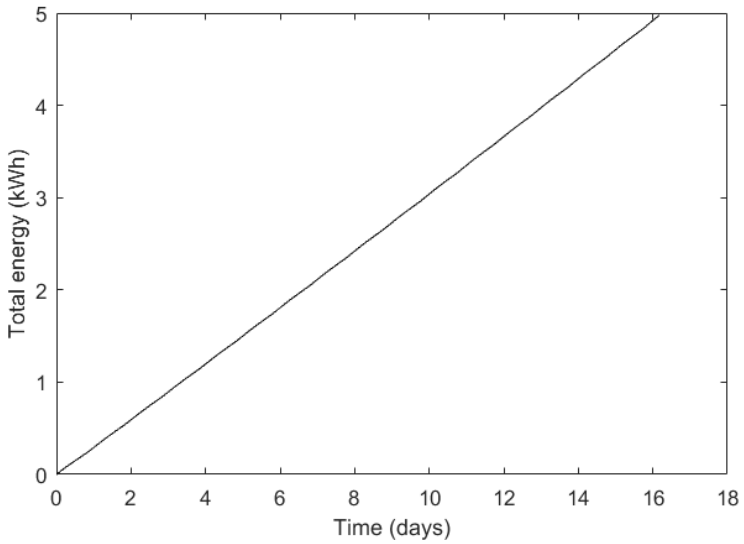

Figure 4.23: Total energy consumption.

4.7 Stability Analysis

The equations that describe attitude control law presented in section 4.2, as well as all of the rest of the equations that govern the simulations executed and results presented in this chapter are non linear. This provides highly accurate predictions of the behaviour of the controller and deorbiting algorithms. However, there are situations where in order to analyse certain features of the controller, it is necessary to perform a linearisation of the system. Such is the case of the stability analysis, where in order to inspect the system, we first need to express the system in a Linear Periodic Time-Varying form, to then be able to apply Floquet theory, explained later in this chapter. Therefore, in order to provide a stability analysis of the geomagnetic field tracking mode of a CubeSat, a linearisation needs to be performed. This process is described next.

First, we take the time derivative of Eq. (4.2) as follows:

$$\dot{\mathbf{e}} = (\boldsymbol{\omega} \times \mathbf{i}) \times \hat{\mathbf{b}} = -[\hat{\mathbf{b}}\times][\boldsymbol{\omega}\times]\mathbf{i} = \mathbf{f}(\hat{\mathbf{b}}, \boldsymbol{\omega}) \tag{4.12}$$

Also, Equation (3.12) is replicated here for convenience:

$$\dot{\boldsymbol{\omega}} = \mathbf{J}^{-1}(-\boldsymbol{\omega} \times \mathbf{J}\boldsymbol{\omega} + \boldsymbol{\tau_{tot}}) = \mathbf{g}(\boldsymbol{\omega}, \boldsymbol{\tau_{tot}}) \tag{4.13}$$

Note that the desired equilibrium states are $\mathbf{e} = (0\ 0\ 0)^T$ and $\boldsymbol{\omega} = (\omega_x\ 0\ 0)^T$, where ω_x is a rotation rate allowed in the x axis of the satellite, which is not required to be zero. The equilibrium point also implies that the nominal normalized magnetic field vector in the B frame is given by $\hat{\mathbf{b}} = (1\ 0\ 0)^T$. The linearised system is expressed as follows:

$$\dot{\mathbf{x}} = \begin{bmatrix} \dfrac{\partial \mathbf{f}(\hat{\mathbf{b}}, \boldsymbol{\omega})}{\partial \mathbf{e}} & \dfrac{\partial \mathbf{f}(\hat{\mathbf{b}}, \boldsymbol{\omega})}{\partial \boldsymbol{\omega}} \\ \dfrac{\partial \mathbf{g}(\boldsymbol{\omega}, \boldsymbol{\tau_{tot}})}{\partial \mathbf{e}} & \dfrac{\partial \mathbf{g}(\boldsymbol{\omega}, \boldsymbol{\tau_{tot}})}{\partial \boldsymbol{\omega}} \end{bmatrix} \mathbf{x} + \begin{bmatrix} \dfrac{\partial \mathbf{f}(\hat{\mathbf{b}}, \boldsymbol{\omega})}{\partial \mathbf{m_{ctrl}}} \\ \dfrac{\partial \mathbf{g}(\boldsymbol{\omega}, \boldsymbol{\tau_{tot}})}{\partial \mathbf{m_{ctrl}}} \end{bmatrix} \mathbf{m_{ctrl}} \tag{4.14}$$

in order to solve the Jacobian equations we execute the following procedure.

Equation (4.2) can be rewritten as:

$$\mathbf{e} = -[\hat{\mathbf{b}}\times]\mathbf{i} \tag{4.15}$$

making use of small perturbation theory, and for the equilibrium point already described, we can define the following expressions:

$$\hat{\mathbf{b}} \approx \frac{1}{\sqrt{1 + 2\delta b_1}} \begin{bmatrix} 1 + \delta b_1 \\ \delta b_2 \\ \delta b_3 \end{bmatrix} \tag{4.16}$$

$$\mathbf{i} \approx \frac{1}{\sqrt{1 + 2\delta i_1}} \begin{bmatrix} 1 + \delta i_1 \\ \delta i_2 \\ \delta i_3 \end{bmatrix} \tag{4.17}$$

substituting this expressions into Eq. (4.2) we have the following result:

$$\hat{\mathbf{e}} \approx \frac{1}{\sqrt{(1 + 2\delta b_1)(1 + 2\delta i_1)}} \begin{bmatrix} 1 + \delta i_1 \\ \delta i_2 \\ \delta i_3 \end{bmatrix} \times \begin{bmatrix} 1 + \delta b_1 \\ \delta b_2 \\ \delta b_3 \end{bmatrix} \tag{4.18}$$

developing this expression we can reach the following simplification:

$$\hat{\mathbf{e}} \approx \frac{1}{\sqrt{1 + 2(\delta b_1 + \delta i_1)}} \begin{bmatrix} 0 \\ \delta i_3 - \delta b_3 \\ \delta b_2 - \delta i_2 \end{bmatrix} \tag{4.19}$$

taking the partial derivative of Equation (4.12) we obtain :

$$\frac{\partial \dot{\mathbf{e}}}{\partial \mathbf{i}} = -[\hat{\mathbf{b}}\times][\boldsymbol{\omega}\times] \tag{4.20}$$

likewise, taking the partial derivative of Equation (4.15), the following expression can be obtained:

$$\frac{\partial \mathbf{e}}{\partial \mathbf{i}} = -[\hat{\mathbf{b}}\times] \tag{4.21}$$

Looking at Equation (4.14), we first need to find $\partial\dot{\mathbf{e}}/\partial\mathbf{e}$, so we have:

$$\frac{\partial \dot{\mathbf{e}}}{\partial \mathbf{e}} = \frac{\partial \dot{\mathbf{e}}}{\partial \mathbf{i}}\frac{\partial \mathbf{i}}{\partial \mathbf{e}} \tag{4.22}$$

substituting Equation (4.20) into Equation (4.22) we end up with the following expression:

$$\frac{\partial \dot{\mathbf{e}}}{\partial \mathbf{e}} = -[\hat{\mathbf{b}}\times][\boldsymbol{\omega}\times]\frac{\partial \mathbf{i}}{\partial \mathbf{e}} \tag{4.23}$$

substituting the nominal values into this expression we have the following form:

$$\frac{\partial \dot{\mathbf{e}}}{\partial \mathbf{e}} = \begin{bmatrix} 0 & 0 & 0 \\ 0 & 0 & 1 \\ 0 & -1 & 0 \end{bmatrix} \begin{bmatrix} 0 & 0 & 0 \\ 0 & 0 & -\omega_x \\ 0 & \omega_x & 0 \end{bmatrix} \begin{bmatrix} \frac{\partial \mathbf{i_i}}{\partial \mathbf{e_j}} \end{bmatrix} \tag{4.24}$$

applying some algebra we can arrive at the following results:

$$\frac{\partial \dot{\mathbf{e}}}{\partial \mathbf{e}} = \begin{bmatrix} 0 & 0 & 0 \\ 0 & \omega_x & 0 \\ 0 & 0 & \omega_x \end{bmatrix} \begin{bmatrix} \frac{\partial \mathbf{i_i}}{\partial \mathbf{e_j}} \end{bmatrix} \tag{4.25}$$

$$\frac{\partial \dot{\mathbf{e}}}{\partial \mathbf{e}} = \begin{bmatrix} 0 & 0 & 0 \\ \omega_x \frac{\partial \mathbf{i_2}}{\partial \mathbf{e_1}} & \omega_x \frac{\partial \mathbf{i_2}}{\partial \mathbf{e_2}} & \omega_x \frac{\partial \mathbf{i_2}}{\partial \mathbf{e_3}} \\ \omega_x \frac{\partial \mathbf{i_3}}{\partial \mathbf{e_1}} & \omega_x \frac{\partial \mathbf{i_3}}{\partial \mathbf{e_2}} & \omega_x \frac{\partial \mathbf{i_3}}{\partial \mathbf{e_3}} \end{bmatrix} \tag{4.26}$$

Since magnetorquers can only generate torques perpendicular to the magnetic field, it must be noted that in Equation (4.19), the values of δb_1 and δi_1 can be set to 0, since perturbations in this plane can't contribute to the torque generated by magnetorquers. In this way, we have the following expressions:

$$e_1 = 0 \tag{4.27}$$

$$e_2 = (\delta x_3 - \delta b_3) \tag{4.28}$$

$$e_3 = (\delta b_2 - \delta x_2) \tag{4.29}$$

solving for δx_2 and δx_3 we have:

$$\delta x_2 = -(e_3^* + \delta e_3) + \delta b_2 = -\delta e_3 + \delta b_2 \tag{4.30}$$

$$\delta x_3 = (e_2^* + \delta e_2) + \delta b_3 = \delta e_2 + \delta b_3 \tag{4.31}$$

where the superscript, *, denotes the nominal values. Then we have:

$$\frac{\partial \delta x_2}{\partial \delta e_3} = -1 \tag{4.32}$$

$$\frac{\partial \delta x_3}{\partial \delta e_2} = 1 \tag{4.33}$$

and finally we arrive at the result we were looking for in Equation 4.22:

$$\frac{\partial \dot{\mathbf{e}}}{\partial \mathbf{e}} = \begin{bmatrix} 0 & 0 & 0 \\ 0 & 0 & -\omega_x \\ 0 & \omega_x & 0 \end{bmatrix} \tag{4.34}$$

Next, we need to obtain $\partial \dot{\mathbf{e}}/\partial \boldsymbol{\omega}$. Rearranging Equation (4.12), we can express it as:

$$\dot{\mathbf{e}} = [\hat{\mathbf{b}}\times][\mathbf{i}\times]\boldsymbol{\omega} \tag{4.35}$$

then we have the partial derivative:

$$\frac{\partial \dot{\mathbf{e}}}{\partial \boldsymbol{\omega}} = [\hat{\mathbf{b}}\times][\mathbf{i}\times] \tag{4.36}$$

substituting for nominal values:

$$\frac{\partial \dot{\mathbf{e}}}{\partial \boldsymbol{\omega}} = \begin{bmatrix} 0 & 0 & 0 \\ 0 & 0 & -1 \\ 0 & 1 & 0 \end{bmatrix} \begin{bmatrix} 0 & 0 & 0 \\ 0 & 0 & -1 \\ 0 & 1 & 0 \end{bmatrix} \tag{4.37}$$

finally, after executing the required algebra, we have:

$$\frac{\partial \dot{\mathbf{e}}}{\partial \boldsymbol{\omega}} = \begin{bmatrix} 0 & 0 & 0 \\ 0 & -1 & 0 \\ 0 & 0 & -1 \end{bmatrix} \tag{4.38}$$

Looking at Equation 4.13 the following result is clear:

$$\frac{\partial \mathbf{g}(\boldsymbol{\omega}, \boldsymbol{\tau_{tot}})}{\partial \mathbf{e}} = \mathbf{0_3} \tag{4.39}$$

then we have to solve for $\partial \mathbf{g}(\boldsymbol{\omega}, \boldsymbol{\tau_{tot}})/\partial \boldsymbol{\omega}$

Equation (4.13) can be expressed in extended form as:

$$\dot{\boldsymbol{\omega}}_{\boldsymbol{x}} = \frac{(J_{yy} - J_{zz})}{J_{xx}} \omega_y \omega_z + \tau_{totx} \tag{4.40}$$

$$\dot{\boldsymbol{\omega}}_{\boldsymbol{y}} = \frac{(J_{zz} - J_{xx})}{J_{yy}} \omega_z \omega_x + \tau_{toty} \tag{4.41}$$

$$\dot{\boldsymbol{\omega}}_{\boldsymbol{z}} = \frac{(J_{xx} - J_{yy})}{J_{zz}} \omega_x \omega_y + \tau_{totz} \tag{4.42}$$

then we have to solve for $\partial \mathbf{g}(\boldsymbol{\omega}, \boldsymbol{\tau_{tot}})/\partial \boldsymbol{\omega}$ as:

$$\frac{\partial \mathbf{g}(\boldsymbol{\omega}, \boldsymbol{\tau_{tot}})}{\partial \boldsymbol{\omega}} = \begin{bmatrix} \frac{\partial \dot{\boldsymbol{\omega}}_{\boldsymbol{x}}}{\partial \boldsymbol{\omega}_{\boldsymbol{x}}} & \frac{\partial \dot{\boldsymbol{\omega}}_{\boldsymbol{x}}}{\partial \boldsymbol{\omega}_{\boldsymbol{y}}} & \frac{\partial \dot{\boldsymbol{\omega}}_{\boldsymbol{x}}}{\partial \boldsymbol{\omega}_{\boldsymbol{z}}} \\ \frac{\partial \dot{\boldsymbol{\omega}}_{\boldsymbol{y}}}{\partial \boldsymbol{\omega}_{\boldsymbol{x}}} & \frac{\partial \dot{\boldsymbol{\omega}}_{\boldsymbol{y}}}{\partial \boldsymbol{\omega}_{\boldsymbol{y}}} & \frac{\partial \dot{\boldsymbol{\omega}}_{\boldsymbol{y}}}{\partial \boldsymbol{\omega}_{\boldsymbol{z}}} \\ \frac{\partial \dot{\boldsymbol{\omega}}_{\boldsymbol{z}}}{\partial \boldsymbol{\omega}_{\boldsymbol{x}}} & \frac{\partial \dot{\boldsymbol{\omega}}_{\boldsymbol{z}}}{\partial \boldsymbol{\omega}_{\boldsymbol{y}}} & \frac{\partial \dot{\boldsymbol{\omega}}_{\boldsymbol{z}}}{\partial \boldsymbol{\omega}_{\boldsymbol{z}}} \end{bmatrix} \tag{4.43}$$

solving for nominal values we then obtain:

$$\frac{\partial \mathbf{g}(\boldsymbol{\omega}, \boldsymbol{\tau_{tot}})}{\partial \boldsymbol{\omega}} = \begin{bmatrix} 0 & 0 & 0 \\ 0 & 0 & \sigma_2 \omega_x \\ 0 & \sigma_3 \omega_x & 0 \end{bmatrix} \tag{4.44}$$

where ω_x is assumed to be a constant, $\sigma_2 = (-J_{xx} + J_{zz})/J_{yy}$, and $\sigma_3 = (J_{xx} - J_{yy})/J_{zz}$.

Now we have all the elements of matrix **A**:

$$\mathbf{A} = \begin{bmatrix} 0 & 0 & 0 & 0 & 0 & 0 \\ 0 & 0 & -\omega_x & 0 & -1 & 0 \\ 0 & \omega_x & 0 & 0 & 0 & -1 \\ 0 & 0 & 0 & 0 & 0 & 0 \\ 0 & 0 & 0 & 0 & 0 & \sigma_2\omega_x \\ 0 & 0 & 0 & 0 & \sigma_3\omega_x & 0 \end{bmatrix} \tag{4.45}$$

by observation of Equation 4.12 it can also be seen that:

$$\frac{\partial \mathbf{f}(\hat{\mathbf{b}}, \boldsymbol{\omega})}{\partial \mathbf{m_{ctrl}}} = \mathbf{0_3} \tag{4.46}$$

and finally we have:

$$\frac{\partial \mathbf{g}(\boldsymbol{\omega}, \boldsymbol{\tau_{tot}})}{\partial \mathbf{m_{ctrl}}} = \begin{bmatrix} 0 & 0 & 0 \\ 0 & \frac{b_x}{J_{yy}} & 0 \\ 0 & 0 & -\frac{b_x}{J_{zz}} \end{bmatrix} \tag{4.47}$$

Now we also have all of the elements of matrix **B**, which can be expressed as:

$$\mathbf{B} = \begin{bmatrix} 0 & 0 & 0 \\ 0 & 0 & 0 \\ 0 & 0 & 0 \\ 0 & 0 & 0 \\ 0 & \frac{b_x}{J_{yy}} & 0 \\ 0 & 0 & -\frac{b_x}{J_{zz}} \end{bmatrix} \tag{4.48}$$

Once the Jacobian equations are solved, a 6×6 state matrix **A** is obtained, and it is noticed that the first and the fourth rows and columns are all zero. This is due to the fact that the control torque expressed by Eq. (4.1) is always perpendicular to the x axis of the satellite at the equilibrium point. Therefore, it has no components in the x axis of the B frame, and the rotational motion about this axis is allowed in the geomagnetic field tracking mode. Hence, a reduced dimension linearised system is given by

$$\dot{\mathbf{x}}_\mathbf{r} = \mathbf{A}_\mathbf{r}\mathbf{x}_\mathbf{r} + \mathbf{B}_\mathbf{r}(t)\mathbf{K}_\mathbf{r}\mathbf{x}_\mathbf{r} \tag{4.49}$$

where $\mathbf{K_r x_r}$ is a compact form of Eq. (4.10):

$$\mathbf{A_r} = \begin{bmatrix} 0 & -\omega_x & -1 & 0 \\ \omega_x & 0 & 0 & -1 \\ 0 & 0 & 0 & \sigma_2\omega_x \\ 0 & 0 & \sigma_3\omega_x & 0 \end{bmatrix} \tag{4.50}$$

$$\mathbf{B_r}(t) = \begin{bmatrix} 0 & 0 & 0 & \frac{-b_x}{J_{zz}} \\ 0 & 0 & \frac{b_x}{J_{yy}} & 0 \end{bmatrix}^T \tag{4.51}$$

$$\mathbf{K_r} = \begin{bmatrix} 0 & -k_1 & 0 & k_2 \\ k_1 & 0 & -k_2 & 0 \end{bmatrix} \tag{4.52}$$

$$\mathbf{x_r} = \begin{bmatrix} e_y & e_z & \omega_y & \omega_z \end{bmatrix}^T \tag{4.53}$$

The resultant closed-loop system can then be expressed as follows:

$$\dot{\mathbf{x}}_\mathbf{r} = \mathbf{A_{CL}}(t)\mathbf{x_r} \tag{4.54}$$

where

$$\mathbf{A_{CL}}(t) := \mathbf{A_r} + \mathbf{B_r}(t)\mathbf{K_r} \tag{4.55}$$

As the geomagnetic field is periodic along the orbit, the time-varying matrix $\mathbf{A_{CL}}(t)$ is also periodic as follows:

$$\mathbf{A_{CL}}(t) = \mathbf{A_{CL}}(t+T) \tag{4.56}$$

where T is the period of the system equal to the orbit period. Because the system is now expressed in linear periodic time-varying form, the Floquet theory can be used for the stability analysis. A brief summary of the Floquet theory is provided next, and more details can be found in (Khalil, 1996).

4.8 Floquet Theory

In this section, the fundamentals of Floquet Theory are discussed, and it is shown how it can be applied to prove the stability of our system. This summary is based in the work presented in (Kim *et al.*, 2006).

Consider an LPTV system of the following form:

$$\dot{\mathbf{x}}(t) = \mathbf{A}(t)\mathbf{x}(t), \tag{4.57a}$$

$$\mathbf{x}(t_0) = \mathbf{x_0}, \tag{4.57b}$$

for all $t \geq t_0$ where t and t_0 are non-negative real numbers, $\mathbf{x}(t)$ and $\mathbf{x_0}$ are column vectors of magnitude n, and the matrix $\mathbf{A}(t)$ has the dimensions $n \times n$. $\mathbf{A}(t)$ is piecewise continuous, bounded and periodic, as expressed in 4.56. The existence and the uniqueness of the solution are assumed for all $t \geq t_0$.

Consider the LPTV system expressed in 4.57, with the periodicity in $\mathbf{A}(t)$ described in 4.56. Then we can define a constant matrix $\mathbf{F}$ such that

$$e^{\mathbf{F}T} = \mathbf{\Phi}(t_0 + T, t_0) \tag{4.58}$$

where the following equations are to be satisfied:

$$\mathbf{\Phi}(t, \tau) = \mathbf{L}(t)e^{(t-\tau)\mathbf{F}}\mathbf{L^{-1}}(\tau) \tag{4.59}$$

$$\mathbf{L}(t + T) = \mathbf{L}(t) \tag{4.60}$$

$\mathbf{\Phi}(\cdot, \cdot)$ is the state transition matrix, and $\mathbf{L}(t)$ is the solution of the following two point boundary value problem:

$$\dot{\mathbf{L}}(t) = \mathbf{A_{CL}}(t)\mathbf{L}(t) - \mathbf{L}(t)\mathbf{F} \tag{4.61}$$

$$\dot{\mathbf{F}} = 0 \tag{4.62}$$

The boundary conditions are given as follows: $\mathbf{L}(t_0) = \mathbf{I_4}$ and $\mathbf{L}(t_0 + 2T) = \mathbf{I_4}$, and $\mathbf{I_4}$ is the 4 x 4 identity matrix. The LPTV system given by Eq. 4.57 is exponentially stable iff, $\mathbf{F}$ is Hurwitz, this is, the real parts of the eigenvalues are all negative.

Lyapunov transformation. Let an $n \times n$ matrix $\mathbf{L}(t)$, which is continuously differentiable and invertible at all t. Such matrix is called a Lyapunov transformation if there exists a positive constant ρ such that for all t

$$\left\|\mathbf{L}(t)\right\| \leq \rho, \quad \left\|\mathbf{L}^{-1}(t)\right\| \leq \rho \tag{4.63}$$

Lyapunov reducibility theorem. Let $\mathbf{L}(t)$ and $\mathbf{F}$ be the same matrices defined previously.

$$\mathbf{x}(t) = \mathbf{L}(t)\mathbf{y}(t) \tag{4.64}$$

then, the original periodic system, 4.57, is transformed into

$$\dot{\mathbf{y}}(t) = \mathbf{F}\mathbf{y}(t), \tag{4.65a}$$

$$\mathbf{y}(t_0) = \mathbf{x_0}, \tag{4.65b}$$

The eigenvalues of $\mathbf{F}$, λ_F, and the eigenvalues of $\mathbf{\Phi}(t_0 + T, t_0)$, λ_Φ, are related as follows

$$\lambda_\Phi = e^{\lambda_F T} \tag{4.66}$$

In consequence, the LPTV system is exponentially stable iff all the eigenvalues of $\mathbf{\Phi}(t_0 + T, t_0)$ have magnitudes less than one, that is to say, iff all the eigenvalues of $\mathbf{F}$ have negative real parts.

Based on the presented theory, Floquet analysis was performed for a range of ω_x values that went from -10 to 10 °/s. This range of angular velocities is considered realistic, since Fig. 4.9 and Fig. 4.15 show the spin rates around the x axis is very small, less than 0.4 °/s. Also, it can be seen that this is a reasonable range for spinning rates in CubeSats, according to available literature such as (Cheon *et al.*, 2010), (Steyn & Jordaan, 2015), (Schwartz *et al.*, 2020) and (Neilsen *et al.*, 2014), just to mention some works. Figure 4.24 shows the maximum real part of the eigenvalues of $\mathbf{F}$, which are always negative. Hence, the stability of the geomagnetic field tracking system for the given range of ω_x is verified.

4.9 Robustness Analysis

Finally, another critical aspect of the proposed controller is studied. The robustness of the system in the presence of model uncertainties is presented in this section. Robustness is defined by Slotine & Li (Slotine & Li, 1991) as the sensitivity to effects which are not considered in the design such as disturbances, measurement

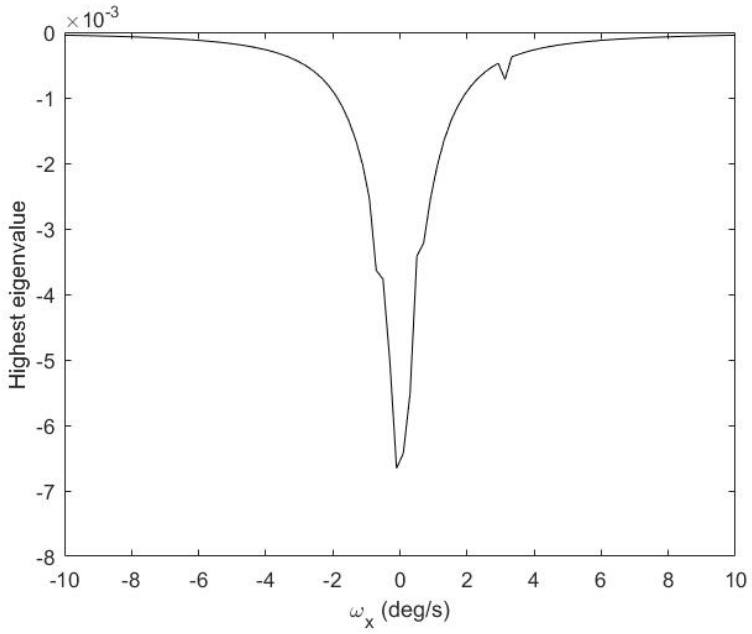

Figure 4.24: Floquet stability analysis results.

noise, unmodeled dynamics, etc. It is important to ensure that our system is able to perform correctly even in the presence of these uncertainties, in order to gain confidence that the deorbiting operation will be successful in a real life mission, where parameters may differ from ideal ones used for models. There are a number of tools in order to study the robustness of a system, such as singular perturbations (Kokotovic *et al.*, 1984), averaging (Meerkov, 1980), and Floquet analysis combined with lifting (Kim *et al.*, 2006).

A very practical method is the use of Monte Carlo simulations. It consists in defining an uncertainty vector and execute a number of simulations varying these parameters randomly within a defined range. If the system proves to be effective under all these variations, it is deemed to be robust for the given range of uncertainty.

In this work, full non-linear robustness analysis of the deorbiting algorithm was performed through Monte Carlo simulations. An uncertainty vector Δ was defined by considering realistic uncertainties in a number of parameters. Mass is varied within a 10%, same variation considered for inertia tensor in the y and z axis. As

for the inertia tensor in the x axis, an absolute value of 0.03 is considered, this helps to account for the variations caused for the engine's consumption of fuel. As for the non-diagonal elements of the inertia tensor, an absolute variation of 0.001, always negative, is considered realistic. The work of Cortiella et al. was taken as a reference for the values of the non diagonal elements of the inertia tensor (Cortiella *et al.*, 2016). Variations in the orbital parameters is also taken into consideration. A variation of 10% is considered for the initial conditions in all six elements: semi-major axis, eccentricity, inclination, argument of perigee, right ascension of the ascending node and mean anomaly. The initial attitude is considered to be completely random. The initial angular velocity vector is considered to be within ± 1 °/s. Finally, the residual magnetic dipole is also taken into consideration, the work of (Maessen *et al.*, 2007) was taken as a reference for the values of this metric, being between 0.0001 and 0.05 A·m^2. A summary of the Δ vector components is given in Table 4.2.

For the robustness analysis, the electrospray engine scenario was considered, for reasons of practicality, since these are the engines which provide a fastest rate of descent. The result of the Monte Carlo simulations are shown in Fig. 4.25.

It can be seen that, even in the presence of the already described parametric and model uncertainties, the deorbiting controller performs well, and is able to deorbit the CubeSat every time. A maximum deorbiting time of less than 21 days is achieved. We have to keep in mind that these deorbiting times correspond to the electrospray engine case. Even though these times can vary for the rest of types studied in this work, the robustness of the controller is being proved. These results give great confidence in the effectiveness and performance of the attitude control law and deorbiting algorithm presented in this chapter.

4.10 Summary and Discussions

In this chapter, an efficient and convenient attitude tracking control law, in conjunction with an algorithm for deorbiting a CubeSat, were presented. It proposes the use of electric engines as means of propulsion. Five electric propulsion technologies are suggested, namely: Electrospray, Micropulsed Plasma Thruster, Hall Effect Thruster, CubeSat Ambipolar Thruster, and Microcathode Arc Thruster.

Table 4.2: Uncertainties vector (Morales *et al.*, 2019)

Uncertainty	Parameter	Range	Formula
δm	Mass	± 0.1	$\tilde{m} = m(1 + \delta m)$
δJ_{xx}	Inertia tensor x axis	[0, 0.03]	$\tilde{J}_{xx} = J_{xx} + \delta J_{xx}$
δJ_{yy}	Inertia tensor y axis	± 0.1	$\tilde{J}_{yy} = J_{yy}(1 + \delta J_{yy})$
δJ_{zz}	Inertia tensor z axis	± 0.1	$\tilde{J}_{zz} = J_{zz}(1 + \delta J_{zz})$
δJ_{ij}	Inertia tensor non-diagonal elements	[-0.001, 0]	$\tilde{J}_{ij} = \delta J_{ij}$
δa	Semi-major axis	± 0.1	$\tilde{a} = a + \delta a \times 100000$
δe	Eccentricity	± 0.1	$\tilde{e} = e(1 + \delta e)$
δi	Inclination	± 0.1	$\tilde{i} = i(1 + \delta i)$
$\delta \omega_p$	Argument of perigee	± 0.1	$\tilde{\omega}_p = \omega_p(1 + \delta \omega_p)$
$\delta \Omega$	Right ascension of the ascending node	± 0.1	$\tilde{\Omega} = \Omega(1 + \delta \Omega)$
δM	Mean anomaly	± 0.1	$\tilde{M} = M(1 + \delta M)$
δq_0	Initial attitude quaternion		Uniform Random
$\delta \omega_0$	Initial angular velocity vector	± 0.017	$\tilde{\omega}_0 = \delta \omega_0$
δm_{yr}	Residual magnetic dipole ($+y$ axis)	[0.0001, 0.05]	$\tilde{\mathbf{m}}_{\mathbf{yr}} = \delta \mathbf{m}_{\mathbf{yr}}$

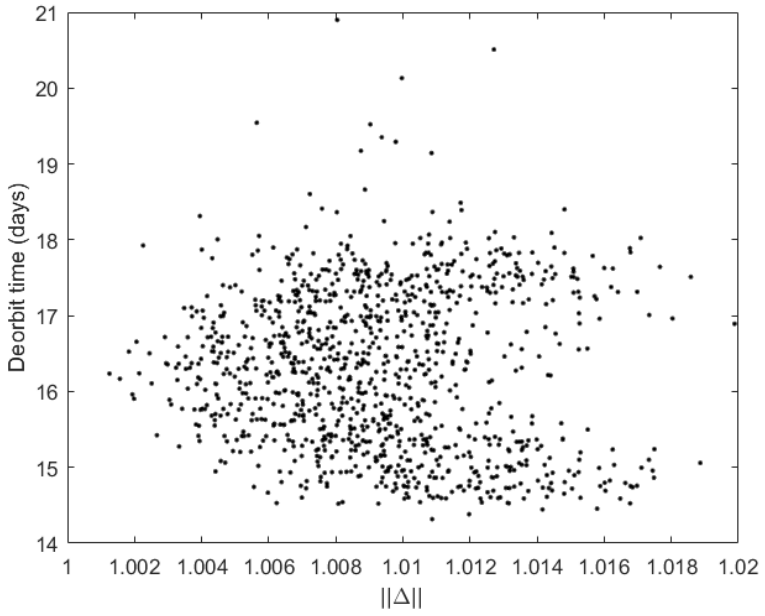

Figure 4.25: Robustness analysis with Monte Carlo simulations.

A deorbit scenario was designed and the performance of the five engines was put to the test via numerical simulations. The algorithm is proven to be effective, and the best performance is obtained with the electrospray thruster, achieving deorbit times in the order of 16 days for an initial orbital altitude of 900 km, and for a CubeSat of 3.5 kg. This performance represents a significant improvement with respect to alternative deorbiting methods such as sails, inflatables, and electric tethers, which offer deorbiting times in the order of months or even years for similar scenarios.

Important aspects of the control law and algorithm, such as stability and robustness were also given. Once linearised, the system can be expressed in linear periodic time-varying form. This fact allowed the analysis of its stability by the means of Floquet theory, proving the system stable for angular velocities in the x axis of $\|\omega_x\| \leq 10$ °/s. The robustness analysis of the deorbiting algorithm in the presence of uncertainties was shown through Monte Carlo simulations. A total of 1000 runs were executed, proving the system robust and giving deorbiting times between 14 and 21 days.

Future work include showing the efficiency of the algorithm for various CubeSat configurations, i.e., more units, and presence of deployable panels or antennas, factors that would affect the satellite's inertia tensor. In this work the control gains were defined by means of trial and error, future work may include the development of formal procedures in order to find optimal control gains, potentially improving the performance of the algorithm, decreasing the deorbiting times, and minimizing the usage of control energy.

The minimal requirements for sensors and actuators is one of the most important feature of this approach. It takes into account the limitations in hardware faced by nanosatellites. It allows this algorithm to be suitable for implementation in many CubeSats with the existing specifications.

Chapter 5

Spin Stabilization and Orbit Sampling

5.1 Introduction

Electric thrusters provide a new alternative for the nanosatellite deorbiting problem. If the CubeSat is equipped with full attitude determination and control capabilities, the implementation of a deorbiting system becomes trivial. However, it is often the case for this type of spacecraft, that they lack such capabilities. In these cases, methods that allow the effective application of thrust even without attitude knowledge are required. Furthermore, even in the cases where the satellite is provided with attitude determination and control capabilities, it might be advantageous to have a redundant deorbiting system.

This chapter presents a new approach that tackles the deorbitiing problem in two stages. First, to spin-stabilize the satellite, which inertially fixes the direction of the spinning axis. Second, an orbit sampling phase, with the aim of identifying the portions of the orbit when the thruster is pointed in the required direction for the application of thrust. A gyroless spin-stabilization scheme is proposed, using only magnetometers and magnetorquers as sensors and actuators respectively. As for the thrusting phase of the algorithm, only GPS receiver data is needed.

5.2 Spin-Stabilization Control Law

In this section, a new control law for CubeSat spin-stabilization is introduced, which is later applied to the CubeSat deorbiting problem. The proposed controller is inspired by the work of Avanzini and Giulietti (Avanzini & Giulietti, 2012), who develop their version of a B-dot detumbling control algorithm, originally proposed by Stickler and Alfriend (Stickler & Alfriend, 1976). The control law in (Avanzini & Giulietti, 2012) is given by

$$\mathbf{m} = -\frac{k}{\|\mathbf{b}\|^2}(\mathbf{b} \times \boldsymbol{\omega}) \tag{5.1}$$

The objective of the B-dot controller is to dissipate the angular velocities along all of the three main axes of a satellite. In our case, however, the objective is to dissipate the angular velocities only along two of the main axes of the CubeSat. The angular velocity of the remaining axis is set to a desired value greater than zero. This is in order to spin-stabilize this axis in the inertial frame. We therefore introduce the variable $\boldsymbol{\omega_d} = (\omega_{dx} \ 0 \ 0)^T$, which represents the desired angular velocity vector. It must be noted that the spinning axis must be the thruster carrying axis. Then, the following control law is proposed:

$$\mathbf{m} = -\frac{k}{\|\mathbf{b}\|^2}[\mathbf{b} \times (\boldsymbol{\omega} - \boldsymbol{\omega_d})] \tag{5.2}$$

The fundamental differences from this control law to the proposed by (Avanzini & Giulietti, 2012), are as follows. In the later work, the control law has the objective to bring the angular velocities in all three axis close to zero. Conversely, in the control law proposed in Eq. 5.2, the objective is to make the spacecraft spin around one of its main axis. As already mentioned, this is achieved by introducing the term $\boldsymbol{\omega_d} = (\omega_{dx} \ 0 \ 0)^T$, which is the desired angular velocity vector. A further difference is that the control law proposed by (Avanzini & Giulietti, 2012) requires the use of gyroscopes, whereas our proposed control law eliminates this dependency, as will be explained next.

Rearranging the terms for convenience, we have the following expression:

$$\mathbf{m} = -\frac{k}{\|\mathbf{b}\|^2}[\mathbf{b} \times \boldsymbol{\omega} - \mathbf{b} \times \boldsymbol{\omega_d}] \tag{5.3}$$

from a basic theorem of kinematics, known as the Transport Theorem (Junkins & Schaub, 2001) we have:

$$\frac{d}{dt}^{ECI}\mathbf{b} = \frac{d}{dt}^{B}\mathbf{b} + \boldsymbol{\omega} \times \mathbf{b} \tag{5.4}$$

since $\mathbf{b}$, as observed in the inertial axis, varies at an angular rate $2\omega_0$, where ω_0 is the orbit rate, we have for $\omega >> 2\omega_0$ (Stickler & Alfriend, 1974):

$$\mathbf{b} \times \boldsymbol{\omega} \approx \dot{\mathbf{b}} \tag{5.5}$$

therefore, the following expression can be derived:

$$\mathbf{m} = \frac{k}{\|\mathbf{b}\|^2}[(\mathbf{b} \times \boldsymbol{\omega_d}) - \dot{\mathbf{b}}] \tag{5.6}$$

where $\dot{\mathbf{b}}$ denotes the Earth's magnetic field time derivative in the body frame. It can immediately be seen that this control law does not require readings of the angular velocity, therefore there is no need for gyroscopes to be on board or operative in the CubeSat.

The magnetic field derivative can be obtained numerically as follows:

$$\dot{\mathbf{b}} \approx \frac{\mathbf{b}(t) - \mathbf{b}(t - \Delta t)}{\Delta t} \tag{5.7}$$

where Δt is a small time period to be chosen by design.

Note that this control law presents the same computational requirements of a B-dot controller, which is commonplace in CubeSat missions. This gives confidence that this new controller is perfectly suitable for its implementation in CubeSats and other types of nanosatellites.

This spin-stabilization controller will fix the orientation of the thrusting carrying axis of the CubeSat in the inertial frame, and it represents the first stage in the CubeSat deorbiting process.

5.3 Deorbiting Algorithm

This section describes the deorbiting phase of the mission. In this stage, the CubeSat is assumed to be spin-stabilized around its thruster carrying axis. The

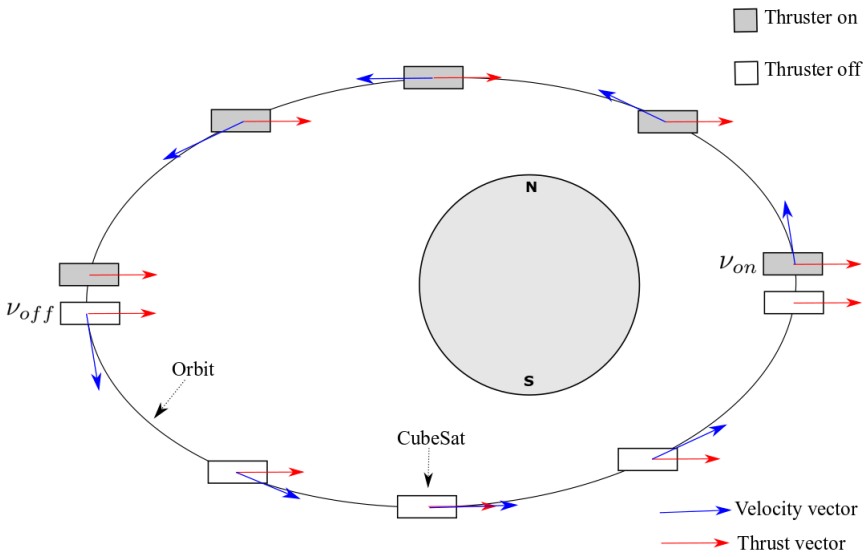

Figure 5.1: Optimal portion of the orbit to thrust (upper half)

algorithm presented in Section 5.2 is ideal in order to accomplish this goal. Unless the spinning axis is perpendicular to the orbital plane, the thruster must point in a suitable direction for deorbiting during half an orbit, as depicted in Fig. 5.1. In this figure, the blue arrows represent the velocity vector, whereas the red arrows represent the thrust vector. In this case, the upper half of the orbit will be the optimal region to activate the thrusters, because this is when the thrust vector opposes the velocity vector. The goal is therefore to find such portion of the orbit. We take an orbit sampling approach, an the steps of the proposed algorithm are listed next.

1. Define the values ν_{on} and ν_{off}, where $\nu_{off} = \nu_{on} + \pi$. These variables represent the true anomalies at which the thrusters will be turned on and off respectively, effectively thrusting during half an orbit. At the beginning of the execution of the algorithm, these values can be chosen arbitrarily.

2. Once ν_{on} is reached, turn the thrusters on. Keep track of the semi-major axis at the beginning of the thrusting phase, a_i.

3. Once ν_{off} is reached, turn the thrusters off, and keep them in that state for the remainder of the orbit. Keep track of the the semi-major axis at the end of the orbit, a_f.

4. At the end of the orbit, and once a_i and a_f are determined, compare their values.

5. If a_f presents a decrease with respect to a_i, this implies that, for the most part, we are thrusting in the correct portion of the orbit, and the orbit is descending. This scenario is depicted in Fig. 5.2 and Fig. 5.4 a). Retain values of ν_{on} and ν_{off} and go back to step 2.

6. If, in the other hand, a_f presents an increase with respect to a_i, this implies that, for the most part, we are thrusting in the wrong portion of the orbit, and the orbit is rising. This scenario is depicted in Fig. 5.3 and Fig. 5.4 b). In this case, ν_{on} and ν_{off} must be updated in the following manner: $\nu_{on\_new} = \nu_{on} + \pi/2$ and $\nu_{off\_new} = \nu_{off} + \pi/2$. Go back to step 2.

The pseudocode for the procedure described above is presented in Algorithm 1, where the function wrapTo2Pi ensures the value of the true anomaly is always between 0 and 2π radians.

The semi-major axis can be computed with the following formula:

$$a = \left(\frac{2}{r} - \frac{v^2}{\mu} \right)^{-1} \tag{5.8}$$

where a is the semi-major axis in m, r is the orbital radius magnitude in m, v is the velocity vector magnitude in m/s, and μ is Earth's gravitational constant. Both r and v vectors are available from GPS readings.

It is noted that, even once condition required by step 5 is met, as the deorbiting process continues, the orbital parameters will change over time, and condition in step 6 may arise again. However, it has been confirmed by simulations, that the algorithm is robust enough to update the values of ν_{on} and ν_{off}, such that the deorbiting maneuver is always successful.

Figure 5.2 shows both the application of thrust, in blue, together with the respective evolution of the semi-major axis, in red, both for one orbit. It is clearly

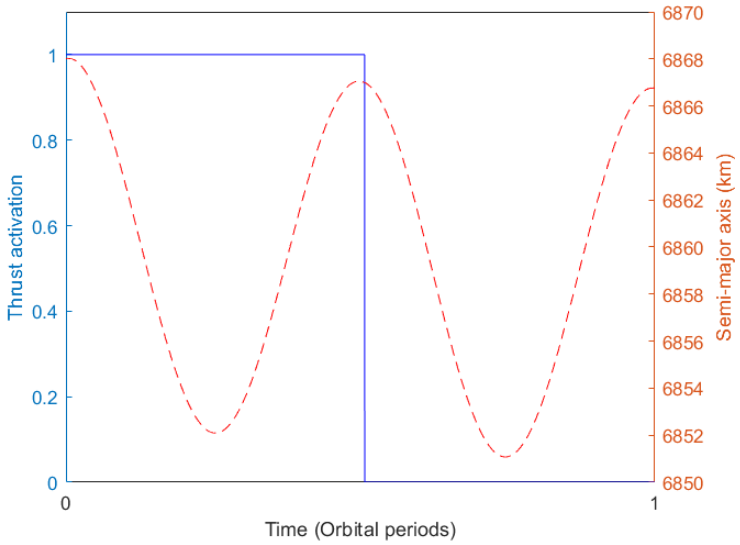

Figure 5.2: Sampling of the orbit. Orbit descending case, where $a_f < a_i$. Note the sinusoidal component in the semi-major axis caused by the J_2 term.

seen that thrust is applied just during the first half of the orbit. It is also evident that the initial semi-major axis a_i, has a bigger value than the final semi-major axis a_f, which coincides with the deactivation of the thrusters. It is clear therefore, that the application of thrust in this half of the orbit is causing the deorbiting of the CubeSat, and ν_{on} and ν_{off} must therefore keep their values while this condition is met.

In the other hand, Fig. 5.3 shows the opposite situation. It depicts how the initial semi-major axis a_i is minor than the final semi-major axis a_f, implying a rising orbit. This is the opposite situation to which is desired, therefore the values of ν_{on} and ν_{off} must be updated as explained in the algorithm above, and keep sampling the orbit in this manner until suitable values are found.

5.4 Deorbiting Scenario

In order to test the effectiveness of this deorbiting algorithm via numerical simulations, the following scenario is designed. A 3U CubeSat, equipped with three

Algorithm 1 Orbital sampling

Input: Semi-major axis a; True anomaly ν

Output: Thrust

$\nu_{\text{on}} \leftarrow \nu$
$\nu_{\text{off}} \leftarrow \text{wrapTo2Pi}(\nu_{\text{on}} + \pi)$
Thrust $\leftarrow$ **true**
$a_{\text{i}} \leftarrow a$
$\nu_{\text{updated}} \leftarrow$ **false**
loop
  if $(\nu_{\text{on}} > \nu_{\text{off}})$ **then**
    condition = $(\nu \geq \nu_{\text{off}}$ **and** $\nu \leq \nu_{\text{on}})$
  else
    condition = **not** $(\nu \geq \nu_{\text{on}}$ **and** $\nu \leq \nu_{\text{off}})$
  end if
  if (condition) **then**
    Thrust $\leftarrow$ **false**
  else
    if (Thrust = **false**) **then**
      if $(a > a_{\text{i}}$ **and** $\nu_{\text{updated}} =$ **false**$)$ **then**
        $\nu_{\text{on}} \leftarrow \text{wrapTo2Pi}(\nu_{\text{on}} + \pi/2)$
        $\nu_{\text{off}} \leftarrow \text{wrapTo2Pi}(\nu_{\text{on}} + \pi)$
        $\nu_{\text{updated}} \leftarrow$ **true**
      else
        Thrust $\leftarrow$ **true**
        $a_{\text{i}} \leftarrow a$
        $\nu_{\text{updated}} \leftarrow$ **false**
      end if
    end if
  end if
end loop

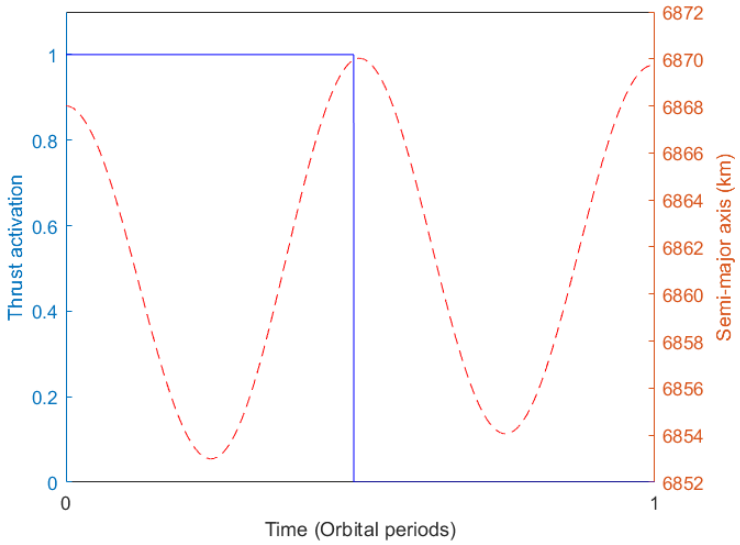

Figure 5.3: Sampling of the orbit. Orbit rising case, where $a_f > a_i$. Note the sinusoidal component in the semi-major axis caused by the J_2 term.

orthogonal magnetorquers, a three axis magnetometer, and a GPS receiver is considered. The CubeSat has a mass of 3.5 kg and the inertia tensor is equal to diag[0.01, 0.0506, 0.0506] kg·m^2, where diag[·,·,·] is the diagonal matrix whose diagonal terms are given in the arguments. Gain k is set to 1×10^{-4} by executing multiple simulations and identifying the best performance. It is deployed at an initial orbital altitude of 500 km, in a near circular orbit and with an inclination of 65°. The desired angular velocity is set to $\boldsymbol{\omega_d} = [10, 0, 0]^{\mathrm{T}}$ °/s, considering an electrospray thruster to be mounted in the x face of the CubeSat body frame. A duty cycle is implemented to allow the magnetometers an magnetorquers to work in conjunction. The magnetorquer is active for 4 seconds, and the magnetometer is active for 1 second at a time. This is the scenario considered for all simulations within this section. They were performed using Matlab/Simulink with the ODE4 numerical integration algorithm and the relative tolerance of 0.001.

Similar to the models in Chapter 4, these simulations do not take into account aerodynamic torques, gravitational pulls from celestial bodies other than the Earth, or solar pressure, as these forcers are orders of magnitude smaller than the

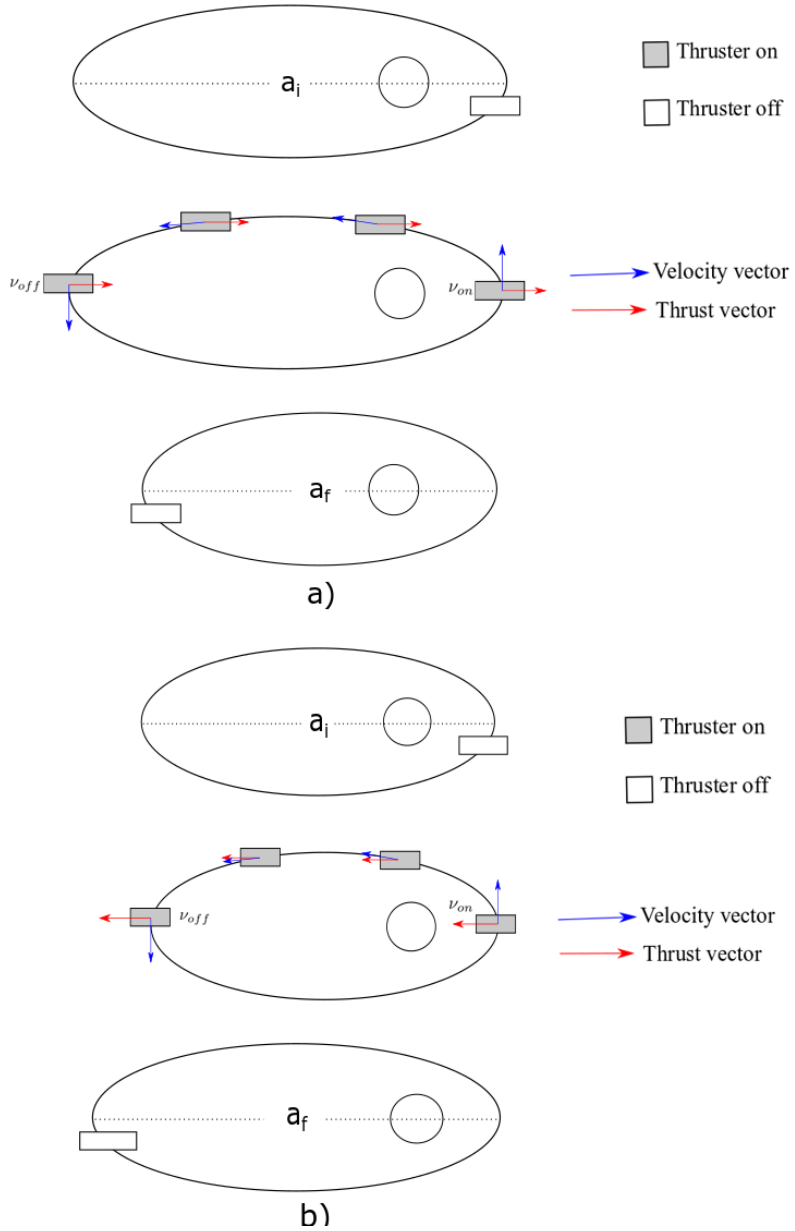

Figure 5.4: a) Falling orbit scenario. b)Rising orbit scenario.

dominating aerodynamic drag, as discussed in Chapter 3. Thus it is not expected that these factors can have a major impact in the performance of the algorithms. It is assumed that there are no failures in the sensors and actuators. It is also assumed that there is enough fuel during the deorbiting operation, as well as that the batteries are able to provide enough energy during eclipses.

5.5 Simulation Results

Both the spinning control law and the deorbiting algorithm were applied to the CubeSat system described in section 5.4, and the results are presented and discussed in this section.

Firstly, we engage with the results of the spinning algorithm. Figure 5.5 shows the evolution of the angular velocities for each axis. Observe that the desired angular velocities are acquired after around 67 minutes, or less than one orbital period. It can also be noted that ω_x attains a value slightly higher than the desired $10°/s$. This is a consequence of the duty cycle approach, which prevents the control dipole from being applied continuously. However, its value is stable. High level of accuracy for the spinning rate is not critical for the deorbit phase of the algorithm, so this is not considered as a problem.

Fig. 5.6 depicts the time history of the control magnetic dipoles applied during the execution of the algorithm. It is worth noticing that even when we are dealing with an scenario where no external disturbances are considered, continuous control dipoles are needed. This is also due to the use of a duty cycle approach, as well as the fact that the CubeSat is underactuated, since the magnetorquers cannot generate torques in arbitrary directions, thus an ideal torque can't be achieved. However, once the angular velocity vector is sufficiently close to the desired one, the magnetorquers can be turned off to save electric power and the deorbiting phase of the algorithm can be executed.

Now, we focus in the results for the deorbiting stage. The results of these simulations are shown in Fig. 5.7, and Fig. 5.8, which depict the evolution of the satellite orbital altitude and semi-major axis respectively. Fig. 5.7 shows how the perigee of the orbit is decreasing in a sustained way. Fig. 5.8 is very revealing. First of all, the effects of the J_2 perturbation are easily seen as they add a sinusoidal

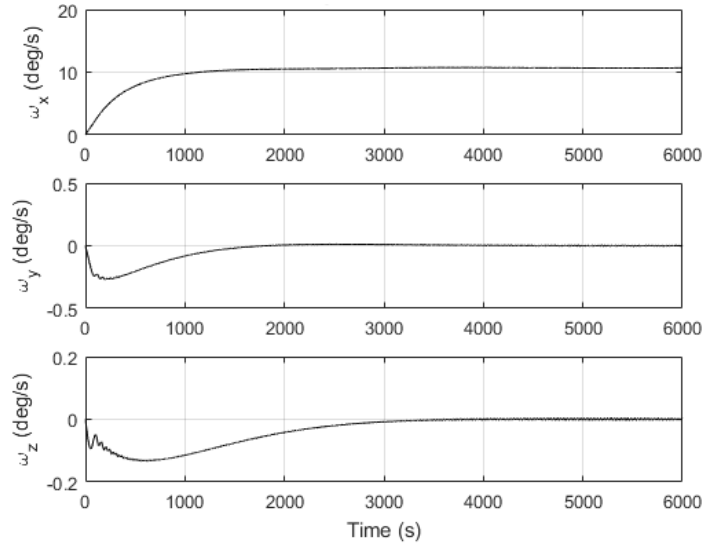

Figure 5.5: Angular velocities.

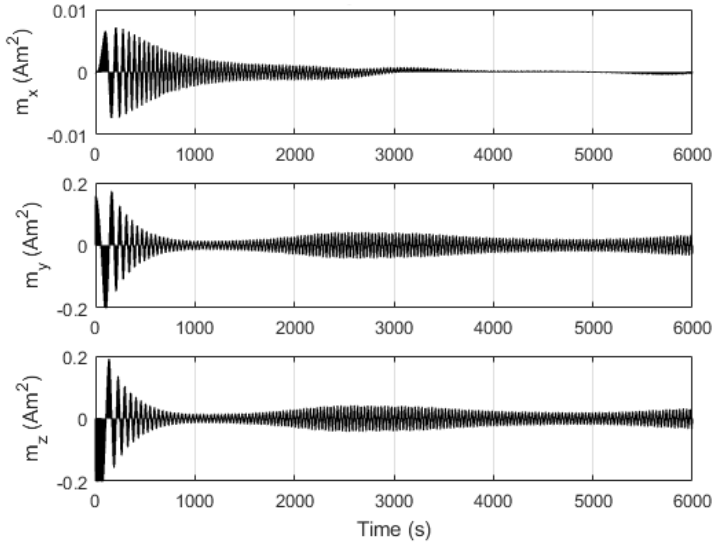

Figure 5.6: Magnetic dipoles.

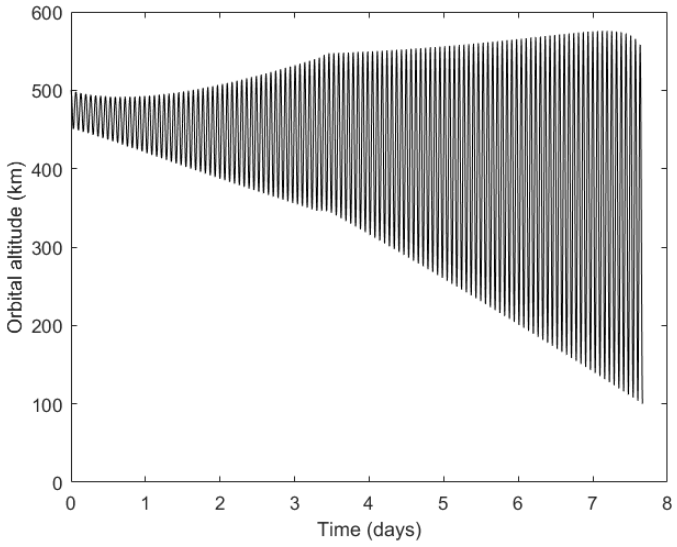

Figure 5.7: CubeSat altitude. Perigee of the CubeSat is continuously decreasing until reentering the atmosphere at an altitude of 100 km.

component to the semi-major axis. Also, a key feature of the deorbit algorithm can be observed. At around three and a half days into the deorbiting operation, it is observed that the semi-major axis starts to increase. The algorithm is able to correct this condition, and brings the satellite back to a steady altitude decrease. In this case, the deorbit operation is achieved within eight days. It is worth to stress the fact that the deorbiting time may vary from one scenario to another, as there is no control over the final orientation of the spinning axis. However, the algorithm is effective in deorbiting the CubeSat every time, which is demonstrated later when the results of the Monte Carlo simulations are presented.

An interesting parameter to look at, is the efficiency per orbit that this algorithm can achieve, this is, how much of the time the thrusters actual state - on/off - coincides with the desired state. This metric is dependent on initial conditions, and therefore, will be slightly different each time, however, Fig. 5.9 depicts the evolution of this value for the current scenario. In this case, initial efficiency is high. However, as the process continues, and orbital parameters evolve, this efficiency eventually drops to a value of around 50%. At this point, the algorithm

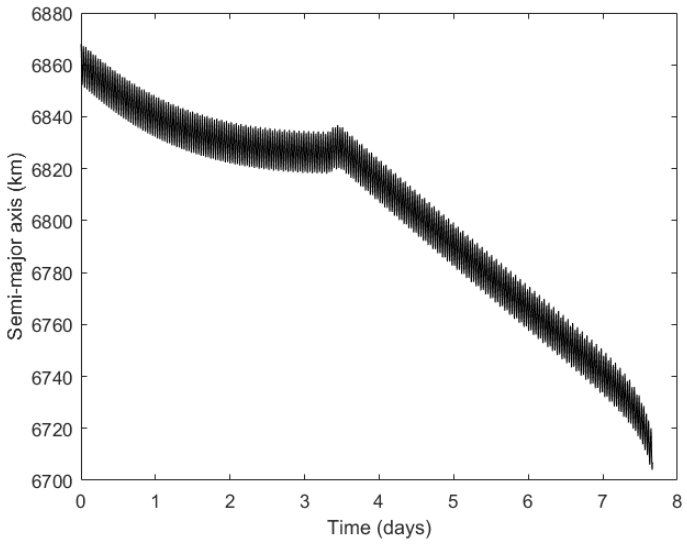

Figure 5.8: Semi-major axis. It can be seen that three and a half days into the deorbiting process, the algorithm has to perform a new sampling of the orbit to continue with the deorbiting process.

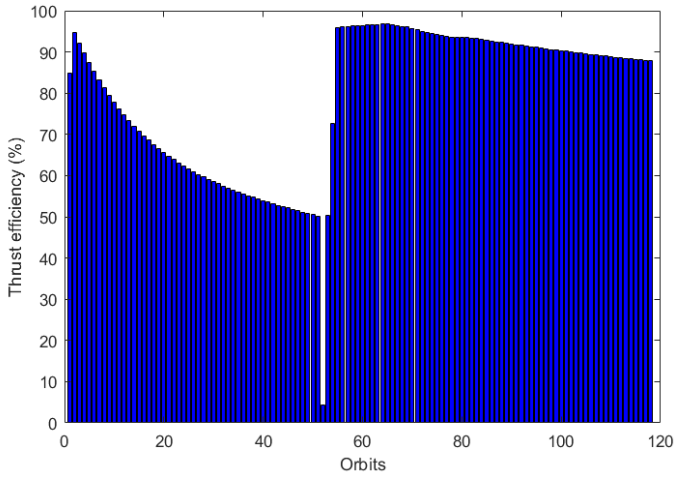

Figure 5.9: Deorbiting algorithm efficiency per orbit.

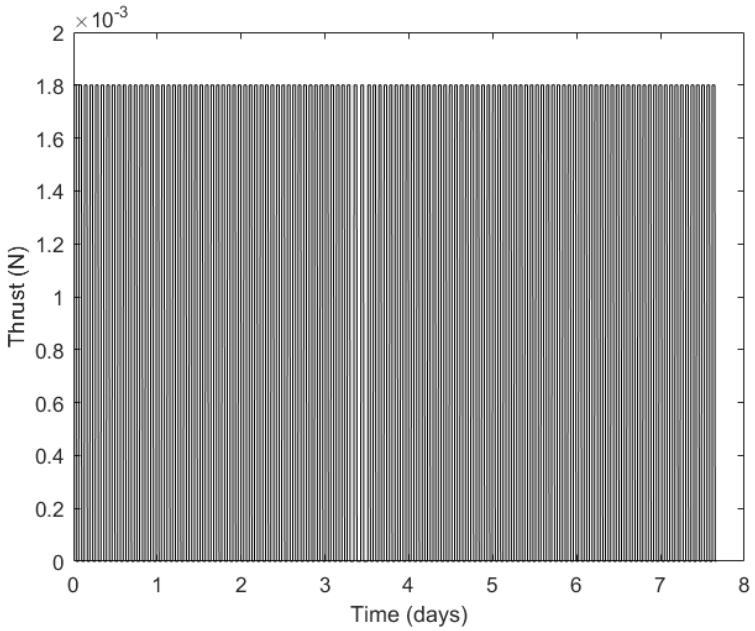

Figure 5.10: Applied thrust during deorbiting process.

detects that the values of ν_{on} and ν_{off} need to be updated, and starts sampling the orbit again. After four orbits, it converges to an efficiency of above 90%. Once this is achieved, the high efficiency remains for the rest of the deorbiting phase. Notice how the semi-major axis evolution shown in Fig. 5.8 is consistent with the efficiency depicted in Fig. 5.9.

Figure 5.10 shows the thrust history that is applied during the deorbiting process. Here the sampling operation that takes place between the 3^{rd} and 4^{th} day can also be seen. A zoom of this is presented in Fig. 5.11 for clarity. The effect can be noticed as an increase of the thrusting period, with a consequent reduction in the duty cycle of the thrusters.

Finally, Fig. 5.12 shows the variations in the orbital inclination of the spacecraft. This is as a result of the spinning axis not necessarily being aligned with the orbital plane. It can be seen that an oscillatory behaviour is induced, and also, the effect can be cumulative as the deorbiting progresses. The variation magnitude will be directly proportional to the angle between the spinning axis and the orbital plane. The largest this angle is, it will be more detrimental to the deorbit-

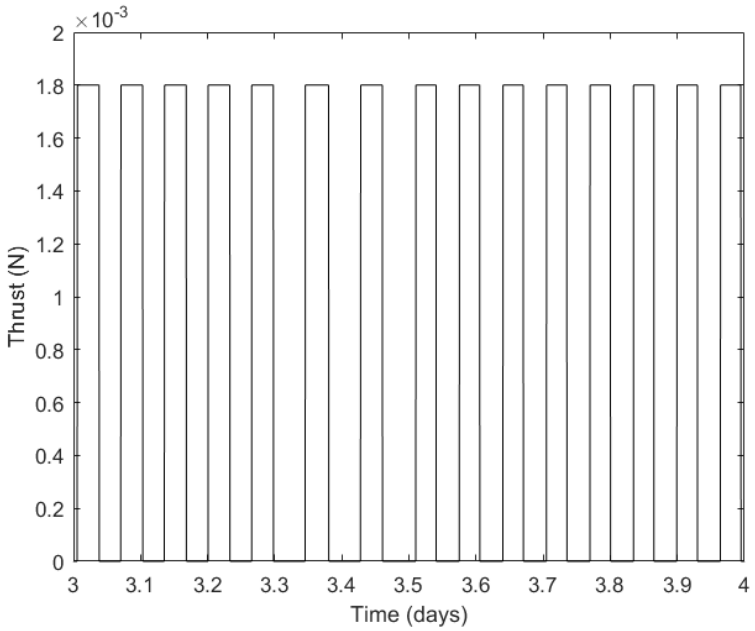

Figure 5.11: Applied thrust during sampling process.

ing performance, since it represents wasted energy from the thrusters. It must be noticed though, that the variations in inclination are very minute, as a result of the small force produced by the thrusters. Because of this, it is not expected that these variations in inclination could represent a major risk of invading the orbits of other operational spacecraft during the deorbiting operation.

5.6 Energy

Just as it was done for the geomagnetic tracking algorithm, we now engage with the analysis of the energy consumption for the algorithm presented in this chapter. Note that in this chapter, initial orbital altitude was about half of that of the scenario presented in Chapter 4. Nonetheless, the results should allow for a comparison of the energetic consumption of both algorithms. Considerations are the same as in Chapter 4, only the energy consumption of electric engines as well as magnetorquers are taken into account, i.e., the consumption of the rest of the subsystem is not considered in this analysis. Again, most of the subsystems are

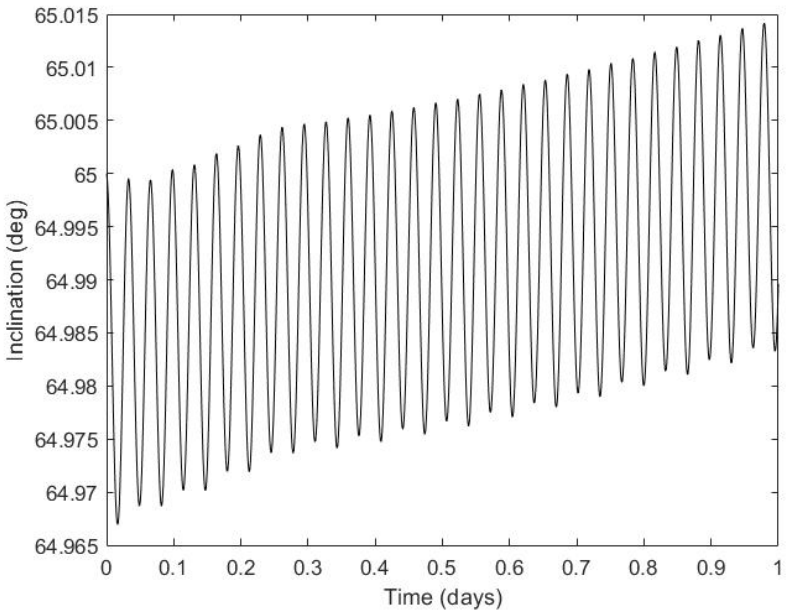

Figure 5.12: Effects on inclination due to spinning axis out of the orbital plane.

not expected to be operative in this stage of the mission, so their impact in energy consumption is expected to be minimal.

Magnetorquer energy consumption for the whole deorbiting phase in the depicted in Figure 5.13. It can be seen that the energy consumption is in the order of 2.3×10^{-4} kWh. It experiences a period of rapid energy consumption when the spinning algorithm is activated. After the required angular velocity vector is achieved, the magnetorquers are turned off, and consequently they do not consume more energy during the rest of the operation.

Figure 5.14 shows that the energy consumed by the thrusters is much more considerable, just as in the case of the geomagnetic tracking algorithm. In this case, reaching a value of around 2.3 kWh, which is similar to the consumption for the same period of time in the aforementioned algorithm. Figure 5.15 shows a zoom of the engine energy consumption. It is clearly seen how the thrusters only consume energy during half of each orbit, being turned off for the rest of it. Just as in the previous chapter, this level of consumption is considered feasible for a real life application.

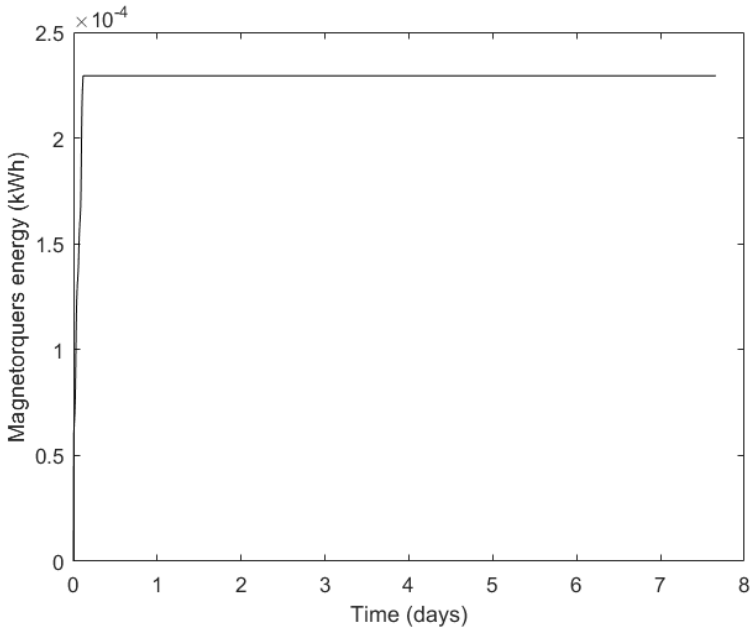

Figure 5.13: Energy consumed by magnetorquers.

Finally, Figure 5.16 shows the total energy consumption, of magnetorquers plus engines, where naturally the energy consumption of the engines dominates.

5.7 Stability Analysis

The stability proof of the spinning algorithm is provided by means of Lasalle's invariance principle (Khalil, 1996; Slotine & Li, 1991). This principle establishes that a controller is stable if it fulfils the following three conditions: 1) a scalar function $V(x)$, known as Lyapunov function, can be defined, such that it is positive definite, 2) its time derivative $\dot{V}$ is negative semi-definite, and 3) no trajectory can stay at points where $\dot{V}(x) = 0$, except at the origin.

Substituting Eq. 5.2 into Eq. 4.7, and defining the term $\boldsymbol{\omega_e} = (\boldsymbol{\omega} - \boldsymbol{\omega_d})$ the following expression is obtained:

$$\boldsymbol{\tau} = -\frac{k}{\|\mathbf{b}\|}(\hat{\mathbf{b}} \times \boldsymbol{\omega_e}) \times \mathbf{b} \tag{5.9}$$

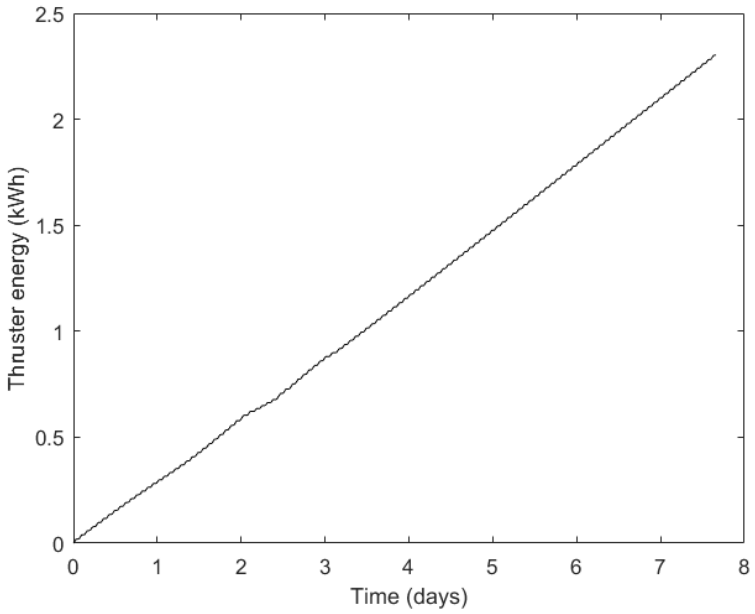

Figure 5.14: Energy consumed by engines.

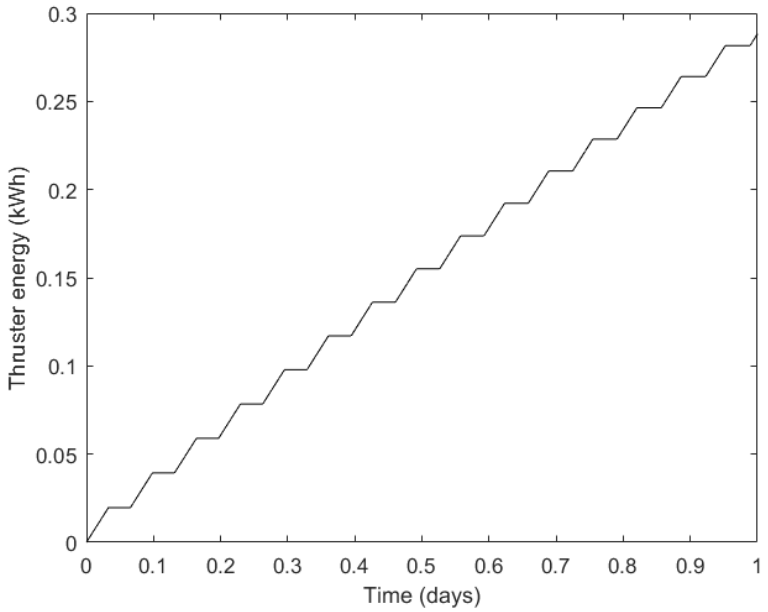

Figure 5.15: Energy consumed by engines zoom.

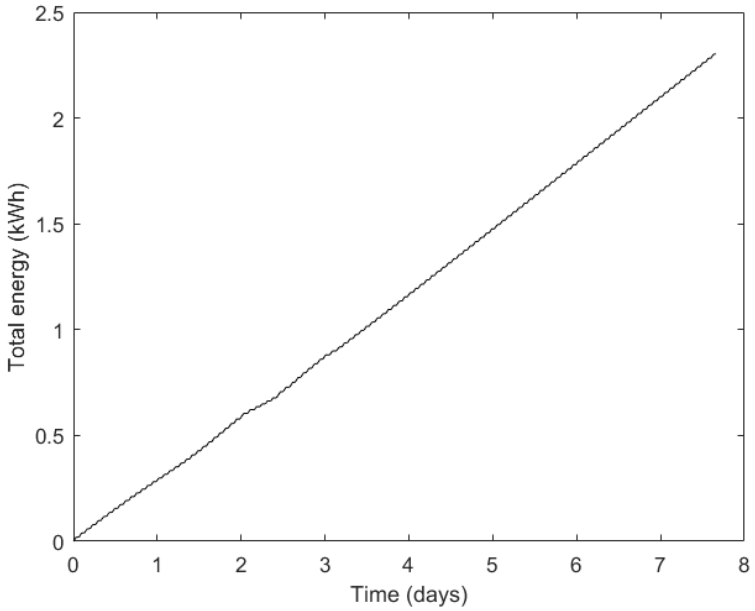

Figure 5.16: Total energy consumed during deorbiting operation.

developing:

$$\boldsymbol{\tau} = -k(\hat{\mathbf{b}} \times \boldsymbol{\omega_e}) \times \hat{\mathbf{b}} \tag{5.10}$$

$$\boldsymbol{\tau} = k[\hat{\mathbf{b}} \times (\hat{\mathbf{b}} \times \boldsymbol{\omega_e})] \tag{5.11}$$

$$\boldsymbol{\tau} = k[\hat{\mathbf{b}}(\hat{\mathbf{b}} \cdot \boldsymbol{\omega_e}) - \boldsymbol{\omega_e}(\hat{\mathbf{b}} \cdot \hat{\mathbf{b}})] \tag{5.12}$$

finally, we obtain the following expression for the applied torque:

$$\boldsymbol{\tau} = -k(I - \hat{\mathbf{b}}\hat{\mathbf{b}}^T)(\boldsymbol{\omega_e}) \tag{5.13}$$

where I is a 3×3 identity matrix, and $\hat{\mathbf{b}} = \mathbf{b}/\|\mathbf{b}\|$ is the normalized magnetic field vector in the B frame.

Notice that $\dot{\boldsymbol{\omega}}_{\boldsymbol{e}}$ is equal to $\dot{\boldsymbol{\omega}} - \dot{\boldsymbol{\omega}}_{\boldsymbol{d}}$, where $\dot{\boldsymbol{\omega}}_{\boldsymbol{d}} = 0$. Then, we propose the following Lyapunov function:

$$V = \frac{1}{2}\boldsymbol{\omega}_{\boldsymbol{e}}^T \mathbf{J} \boldsymbol{\omega}_{\boldsymbol{e}} \tag{5.14}$$

taking its time derivative, we have:

$$\dot{V} = \boldsymbol{\omega}_{\boldsymbol{e}}^T \mathbf{J} \dot{\boldsymbol{\omega}}_{\boldsymbol{e}} = \boldsymbol{\omega}_{\boldsymbol{e}}^T \mathbf{J} \dot{\boldsymbol{\omega}} \tag{5.15}$$

then,

$$\dot{V} = \boldsymbol{\omega}_{\boldsymbol{e}}^T \boldsymbol{\tau} \tag{5.16}$$

and finally we obtain

$$\dot{V} = -k \boldsymbol{\omega}_{\boldsymbol{e}}^T (I - \hat{\mathbf{b}}\hat{\mathbf{b}}^T) \boldsymbol{\omega}_{\boldsymbol{e}} \tag{5.17}$$

where $\dot{V}$ is negative semi-definite, since it can only take negative values or zero.

Finally, it can be observed that $\dot{V}(x) = 0$ in two scenarios: 1) at the origin $\boldsymbol{\omega}_{\boldsymbol{e}} = 0$, and 2) when the Earth's magnetic field $\mathbf{b}$ is parallel to $\boldsymbol{\omega}_{\boldsymbol{e}}$. It is clear, however, that the second scenario cannot be maintained in practice, since the magnetic field vector is time-varying, which would prevent $\boldsymbol{\omega}_{\boldsymbol{e}}$ from tracking it as the satellite orbits the Earth. Therefore the three conditions are met and the system is proven to be stable.

5.8 Robustness Analysis

Monte Carlo simulations were executed in order to prove the robustness of the algorithm. An uncertainties vector is defined as per Table 4.2, which includes reasonable levels of uncertainties for real life missions. The results of the Monte Carlo simulations are depicted in Fig. 5.17. Deorbiting times between 6 and 35 days are attained. Such wide range of deorbiting times comes from the fact that the algorithm is sensitive to the orientation of the spinning axis and there is no control over the latter. The more this spinning axis tends to lie in the orbital plane, less time it will take to deorbit the CubeSat, since thrust is being used more efficiently. Also, notice how these times are considerable shorter than those achievable with the alternative technologies mentioned in Chapter 2. The most important thing to highlight from these simulations however, is the fact that the

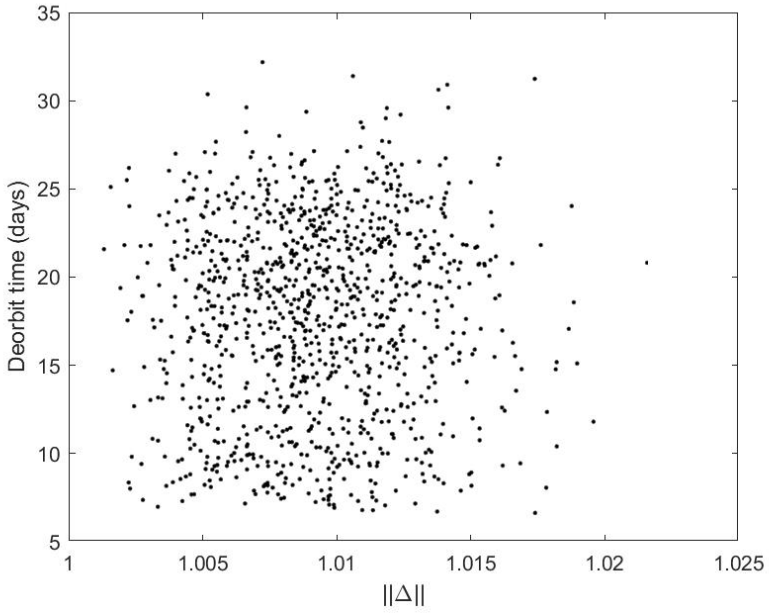

Figure 5.17: Robustness analysis through Monte Carlo simulations.

algorithm is successful in deorbiting the CubeSat every time, even in the presence of uncertainties.

It doesn't come as a big surprise that the system is robust against the variations in the first thirteen elements in table 4.2. However, it is interesting seeing that the a variation as big as 0.05 A·m^2 in the residual magnetic dipole doesn't cause the controller to fail. We have to remember that the CubeSat is spinning around its x axis. This causes the residual magnetic dipoles to be cancelled out with each revolution of the satellite, as shown in Fig. 5.18, which is a generalization of the satellite spinning.

In the sequence of figures, the local magnetic field vector is always pointing right. This is a reasonable simplification as the magnetic vector changes very slowly as the CubeSat orbits the Earth. Then in sequence a), the magnetic dipole is pointing outwards, which produces a torque vector pointing upwards. As the CubeSat continues spinning, we reach scenario b), where the residual magnetic dipole vector is aligned with Earth's magnetic field vector, thus, no torque is produced. By the time scenario c) is reached, the residual magnetic dipole vector

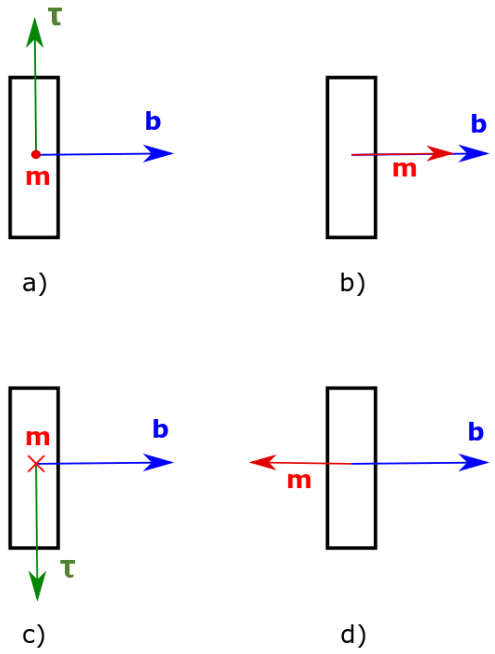

Figure 5.18: Residual magnetic dipole effects in spinning CubeSat.

is pointing inwards, with a resulting torque vector pointing downwards. Notice how this will effectively cancel out the torque first generated in scenario a). Finally, in scenario d), the residual magnetic dipole and the magnetic field vector are parallel once again, producing no torque. This general scenario can be translated to different orientations of the CubeSat with respect to the magnetic field vector, as it continues its orbit around the Earth.

5.9 Summary and Discussions

In this chapter, both a spin-stabilization controller and a deorbiting algorithm for CubeSats have been presented. They can be used in conjunction to achieve the deorbiting of a nanosatellite when full attitude information is not available. Both are ideal for application in CubeSats, as they take into account hardware and software limitations present in this type of satellites.

The spin-stabilization controller is inspired in the popular B-dot algorithm. Its novelty is the fact that it doesn't require gyroscopes readings to operate, as it only requires the magnetic field measurement as an input. In the case of the deorbiting algorithm, it only requires information such as true anomaly and semi-major axis. This information can be obtained from GPS receivers, which can be easily integrated in CubeSat platforms.

A mission scenario is defined and the effectiveness of both the spinning controller as well as the orbit sampling algorithm is proven through numerical simulations. Electrospray features were used for the simulations in this chapter. Nonetheless, the effectiveness of the deorbiting algorithm is independent from the type of electric engine being used. This makes it a very versatile option for this application.

Energy consumption analysis was also performed. When compared with the results of Chapter 4, it can be seen that both algorithms consume similar amounts of energy. Such levels of energy consumptions make these algorithms feasible for CubeSat implementation.

Stability of the spinning algorithm is provided by the means of Lasalle's invariance principle. Robustness against model uncertainties is proven through Monte Carlo simulations. Deorbit times between 6 and 35 days are obtained, which

represent a substantial improvement with respect to the performance of other approaches such as sails, inflatables, and electric tethers. These algorithms can be applied as part of the efforts to tackle the space junk problem.

Future work includes research on how to align the spinning axis with the orbital plane, as this will optimize the use of the thrusters and minimize the amount of deorbiting time.

Chapter 6

Drag Sail Scenario

6.1 Introduction

The effectiveness, efficiency, and robustness of two different deorbiting systems have been the focus of study in Chapters 4 and 5. These systems consist of an attitude stabilization controller, namely a geomagnetic field tracker or a gyroless spin-stabilization, together with an algorithm for the application of thrust. The practicality of the application of these controllers in conjunction with electric thrusters has been demonstrated. The attitude control laws are flexible in terms of deorbiting actuators. The possibility of applying them in conjunction with non propulsive actuators, specifically drag sails, is explored in this chapter.

There is a rich literature discussing mechanisms to deploy sails in CubeSats such as in (Harkness *et al.*, 2014), (Steyn & Lappas, 2011), (Adeli & Lappas, 2010), and (Biddy & Svitek, 2012) just to mention some. Some of them even highlight the difficulties of the deploying process (Reichenbach *et al.*, 2018). However, there is a gap in the literature as to how to stabilize the sails once they are deployed. A tumbling sail does increase the drag and ensures a faster CubeSat deorbiting process, however, it is not an optimal way. In this chapter, an evaluation of how the controllers previously introduced can work together with drag sails in order to achieve fast deorbiting is presented.

Five scenarios are discussed, namely: 1) natural decay, i.e., no drag sail, 2) tumbling sail, 3) sail stabilized with geomagnetic field tracker controller in a polar

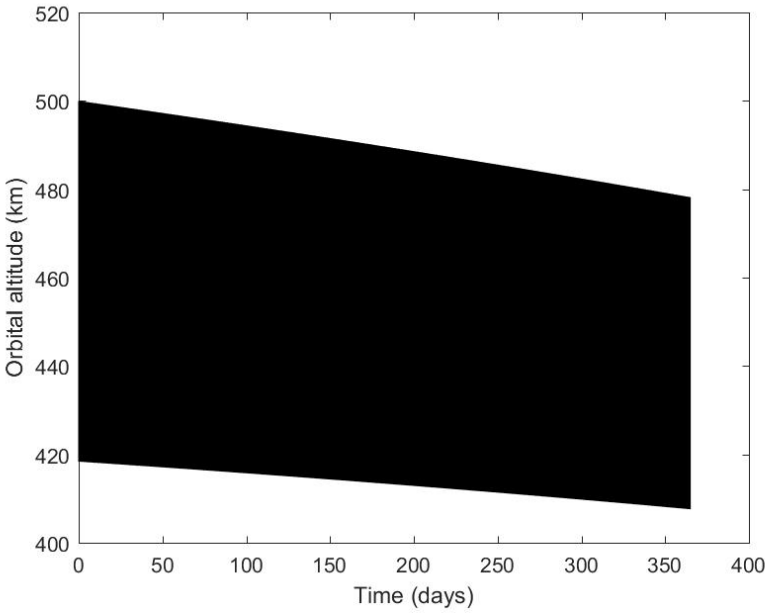

Figure 6.1: Altitude evolution during no-sail scenario.

orbit, 4) sail stabilized with geomagnetic field tracker controller at an inclined orbit, and finally, 5) the gyroless spin-stabilized drag sail. Simulation and results are presented and analysed for each case.

6.2 Tumbling CubeSat

6.2.1 CubeSat without Drag Sail

The first scenario explored in this chapter is the case when the CubeSat is left to natural orbital decay, with no aid from drag sails or any other method. In this scenario, a 3U CubeSat, with a mass of 3.5 kg, with an inertia tensor of diag[0.01, 0.0506, 0.0506] kg·m^2, in an initial quasi-circular orbit with an apogee of 500 km, at an orbital inclination of 90° is considered. The CubeSat is left to tumble freely with an initial angular velocity vector of $\boldsymbol{\omega} = (1\ 1\ 1)^T$ °/s. Only the atmospheric drag is considered as orbital perturbation. One year of the deorbiting process is simulated. The results of the simulations are presented next.

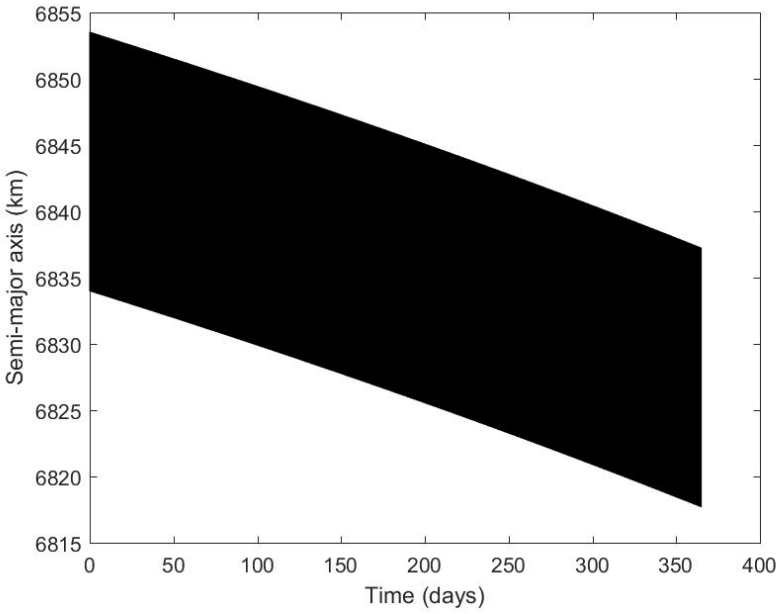

Figure 6.2: Semi-major axis evolution during the no-sail scenario.

Figure 6.1 shows the evolution of the altitude over a period of one year. It can be seen that the decrease in both apogee and perigee is very little over this time span. Apogee only decreases about 20 km, coming from 500 km to 480 km. In the case of perigee, the decrease is even minor, coming from 420 km to 408 km. This agrees with the predictions that one CubeSat in this initial orbit can take several years for it to deorbit by natural decay (Oltrogge & Leveque, 2011).

The evolution of the semi-major axis is presented in Fig. 6.2. Similarly to Fig. 6.1, very little decrease in this metric is observed, given the thin atmospheric density presented at these altitudes.

6.2.2 CubeSat with Drag Sail

An initial benchmark in order to compare how the integration of a drag sail affects the deorbiting rate of a CubeSat is established. In this scenario, a CubeSat equipped with a 5 m^2 drag sail is considered. The mass of the satellite is considered to be 4 kg, with an inertia tensor with the deployed drag sail of diag[1.376,

0.703, 0.703] kg·m^2, and a centre of pressure to centre of mass vector of [-0.075, 0, 0]$^{\mathrm{T}}$ m, according to the work presented in (Steyn & Lappas, 2011). The initial altitude is 500 km, and the inclination of the orbit is 90°.

It is assumed that the drag sail is successfully deployed. Other than that, the same set of assumptions presented in Chapters 4 and 5 are made, except for one. This is due to a substantial difference with all the previous simulations presented in this thesis. The aerodynamic torques cannot longer be neglected, as the inclusion of a drag sail will make their magnitude considerable. Therefore, it is necessary to introduce a couple of mathematical expressions that allows for the computing of this torques.

The aerodynamic torque $\boldsymbol{\tau_a}$ can be computed with Eq. 6.1, as expressed in works such as (Clark *et al.*, 1971) and (Stone & Witzgall, 2006).

$$\boldsymbol{\tau_a} = \mathbf{R_{pm}} \times \mathbf{F_D} \tag{6.1}$$

where $\mathbf{R_{pm}}$ is the centre of pressure to centre of mass vector and $\mathbf{F_D}$ is the drag force defined in Eq. 2.1.

Remember that in order to compute $\mathbf{F_D}$, the cross sectional area of the spacecraft facing the velocity vector relative to the atmosphere is needed. In all the previous simulations this was simplified to the worst case scenario, when the x face of the CubeSat was aligned with this vector. This simplification is no longer valid since the variations in cross sectional area will be much larger with the inclusion of a drag sail. Equation 6.2 can be used in order to compute this area, also expressed in works such as (Clark *et al.*, 1971) and (Stone & Witzgall, 2006).

$$A = abs(\hat{\mathbf{v}}_{\mathbf{rel}} \cdot \hat{\mathbf{n}}) A_d \tag{6.2}$$

where $abs()$ denotes the absolute value, $\hat{\mathbf{v}}_{\mathbf{rel}}$ is the unitary velocity vector relative to the atmosphere, $\hat{\mathbf{n}}$ is the drag sail normal vector, and A_d is the total area of the drag sail.

This satellite configuration and initial conditions are used in the remaining of this chapter. The results of this scenario are presented next.

The first metric to be presented is the orbital altitude. Figure 6.3 shows how the inclusion of a drag sail dramatically decreases the deorbit time, which passes

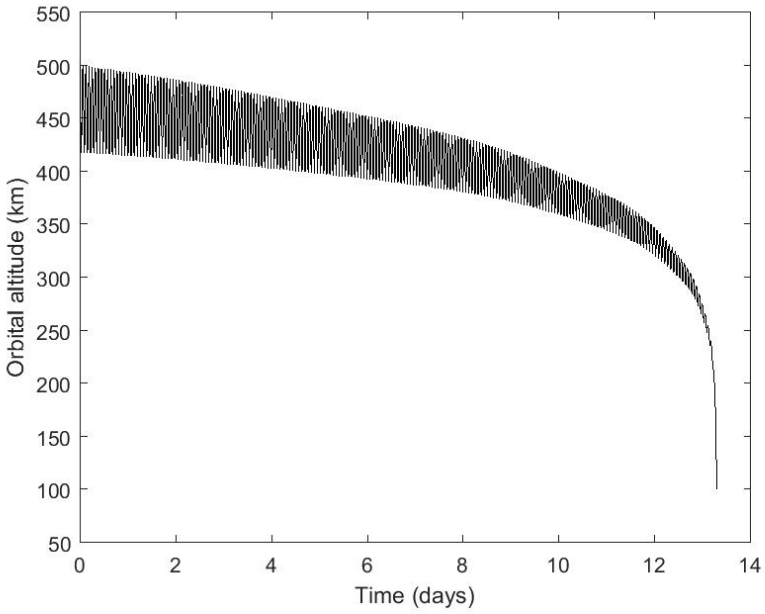

Figure 6.3: Altitude evolution during the tumbling scenario.

from the order of years to the roughly 13 days. It can be seen that the satellite reaches a critical altitude at around 300 km where the atmospheric drag takes over and the deorbit is completed shortly after the CubeSat reaches this region.

The evolution of the semi-major axis of the orbit is presented for completeness in Fig. 6.4. Its correspondence with the orbit altitude presented in Fig. 6.3 is evident, with the satellite reaching a critical geocentric altitude of around 6700 km and quickly falling after this.

6.3 Drag Sail with Geomagnetic Field Tracker

6.3.1 Polar Orbit

In this section, the effects of using the geomagnetic field tracker controller in conjunction with a drag sail are explored. The results of the previous section will be used as a benchmark to analyse the improvement that can be obtained by applying this controller.

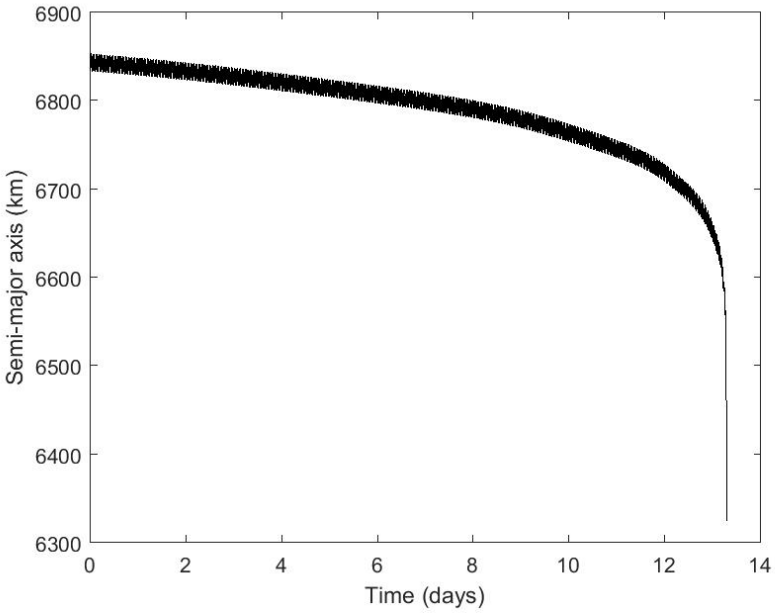

Figure 6.4: Semi-major axis evolution during the tumbling scenario.

Figure 6.5 depicts the evolution of the CubeSat's altitude over the full deorbiting period. It can be seen that the deorbit time in this case is roughly 9 days, an improvement of around 30% with the respect to the tumbling scenario.

Figure 6.6 clearly shows how in this case the attitude controller algorithm has to apply a larger level of control magnetic dipole in order to keep the satellite oriented. This effect can be attributed to the increase in mass and change of the inertia tensor as well as the aerodynamic torques induced by the drag sail. Even though the gains were tuned to acquire the best performance in terms of magnetic field tracking, saturation can be observed in the magnetorquers.

Figure 6.7 show the tracking error between the magnetic field vector and the x axis of the CubeSat. It also gives a sense of how the controller struggles a bit more to control the pointing of the satellite, specially when this starts to lose altitude and reaches denser layers of the atmosphere, where aerodynamic torques become gradually stronger.

The angular rates of the CubeSat during the deorbit process are shown in Fig. 6.8. Even when the controller struggles to stabilize the satellite, the angular rates

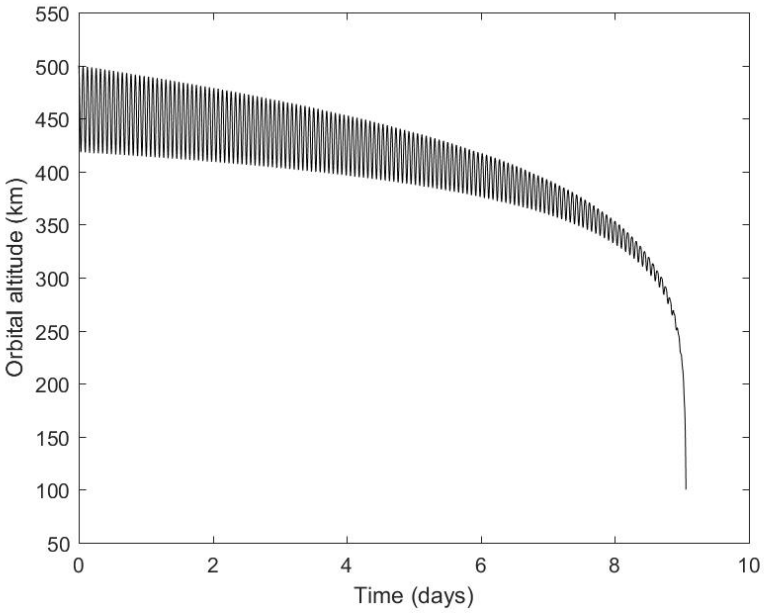

Figure 6.5: Altitude evolution with geomagnetic field tracker in polar orbit scenario.

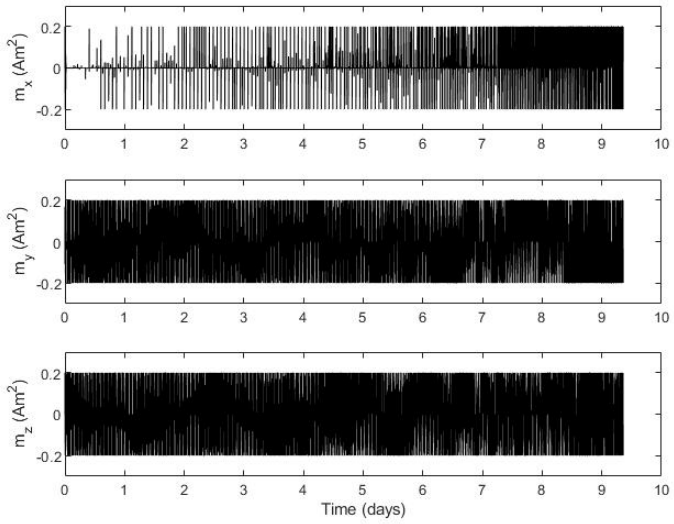

Figure 6.6: Magnetic dipole evolution with geomagnetic field tracker in polar orbit scenario.

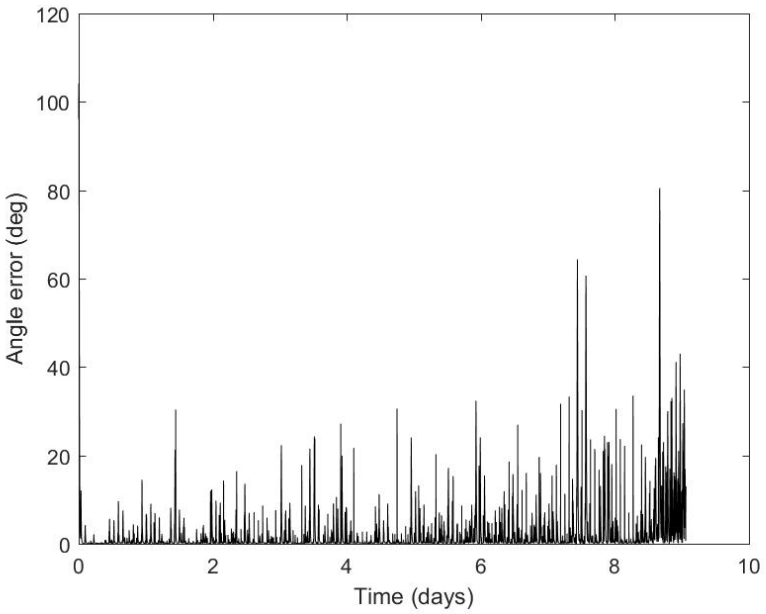

Figure 6.7: Geomagnetic field tracking error in polar orbit scenario.

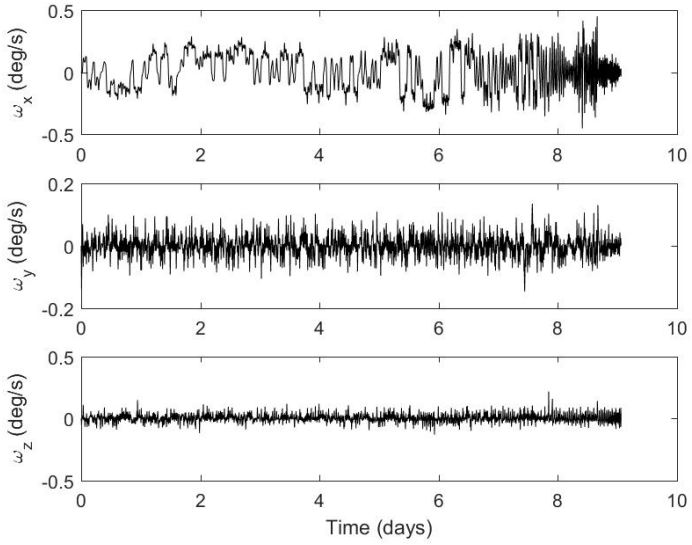

Figure 6.8: Angular velocity evolution with geomagnetic field tracker in polar orbit scenario.

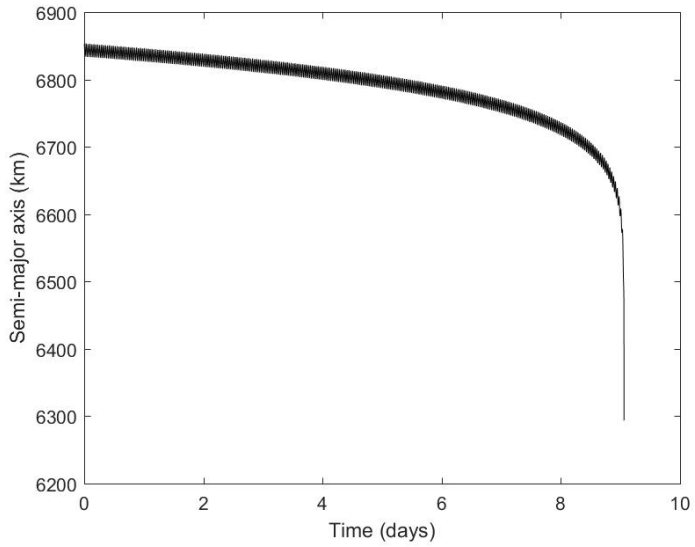

Figure 6.9: Semi-major axis evolution with geomagnetic field tracker in polar orbit scenario.

are kept within relatively low ranges. The magnitude of ω_x doesn't surpass $\pm$ 0.5 °/s, while ω_y and ω_z are kept between $\pm$ 0.2 °/s. Finally, the semi-major axis evolution is presented in Fig. 6.9. Again, it resembles the altitude plot and shows very clearly how the critical geocentric altitude for a drag sail of this area is around 6700 km.

Figure 6.10 makes clear why this controller offers a performance improvement in the polar orbit case. It can be seen that during the majority of the orbit, the normal of the drag sail tends to be aligned with the velocity vector. This generates the maximum drag, since the whole area of the sail is pointing in the direction of travel. The exception occurs over the poles, where the sail normal is perpendicular to the direction of travel.

6.3.2 Inclined Orbit

It is expected for the drag sail with the geomagnetic field tracker controller to have the best performance in the case of a polar orbit. For purposes of comparison of efficiency at different inclinations, another scenario is executed, where only

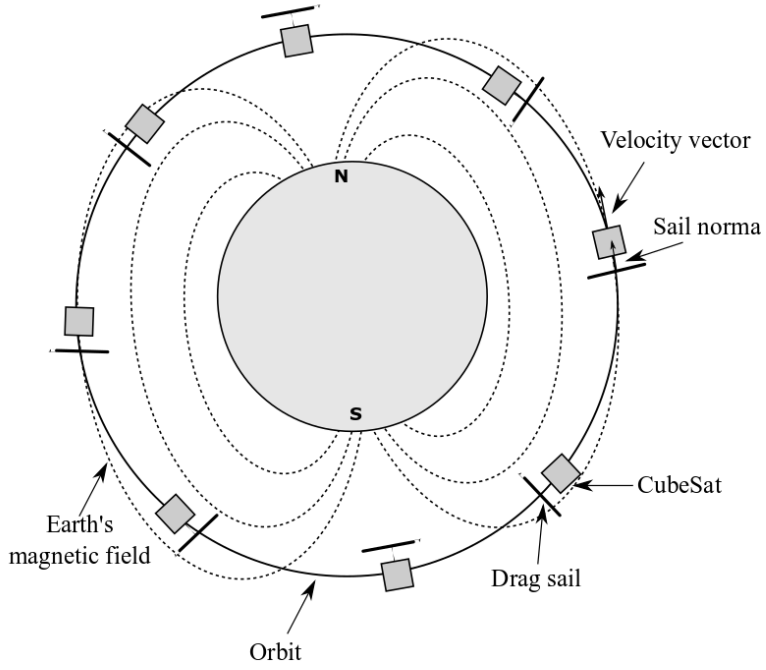

Figure 6.10: Drag sail in a polar orbit.

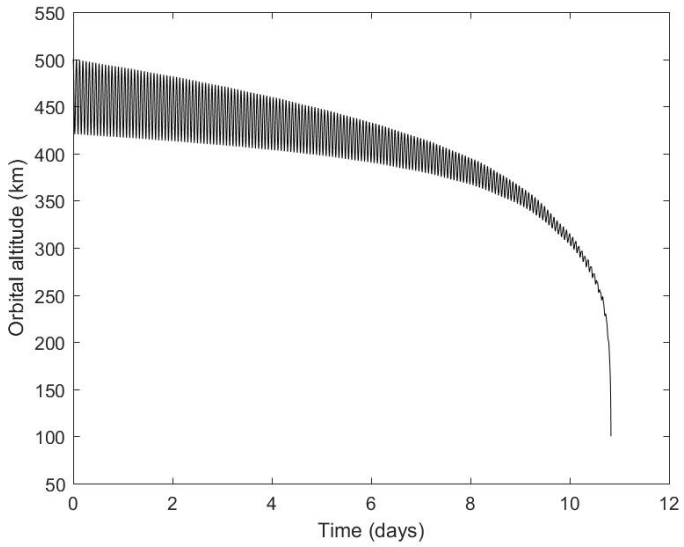

Figure 6.11: Altitude evolution with the geomagnetic field tracker inclined scenario.

the inclination is modified with respect to the scenario presented in the previous subsection. In this case, an orbit of 65° of inclination is considered.

The first metric we can look at is the evolution of the orbital altitude, depicted in Figure 6.11. The deorbiting time is around 11 days, a little bit longer than the 9 days obtained in the polar orbit scenario. The deorbit time is however still very reasonable, even in comparison with the polar case.

The tracking error is shown in Fig. 6.12, where it can be seen that the effectiveness of the algorithm is very good during most part of the deorbiting operation. It is only when the CubeSat reaches ever more dense portions of the atmosphere that the resultant torques become too strong for the actuators to counteract, and the error gradually increases. This is not problematic precisely due to the fact that the CubeSat is already back in the atmosphere and practically deorbited.

Fig. 6.13 shows the evolution of the semi-major axis for the geomagnetic field tracker in the inclined scenario. The critical geocentric altitude is still around 6700 km, after which the altitude of the CubeSat rapidly decreases.

Looking at Fig. 6.14 it is clear why the geomagnetic field tracker is less efficient

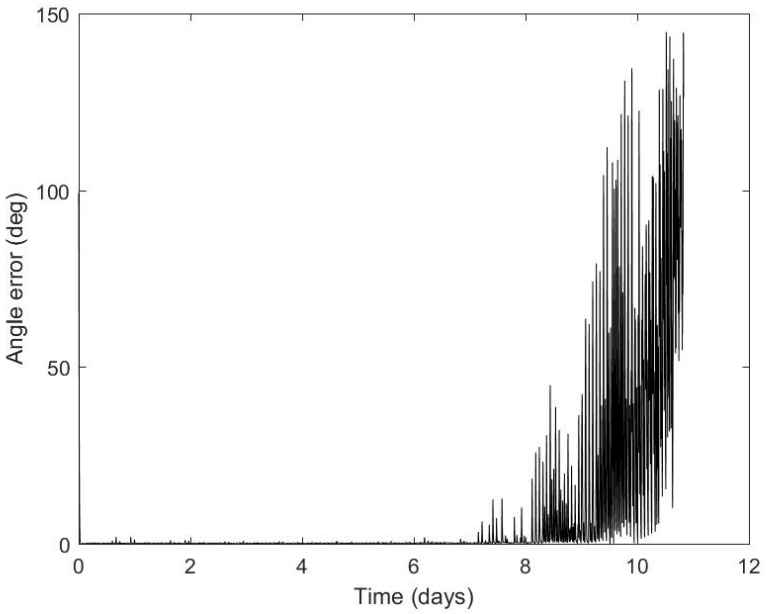

Figure 6.12: Geomagnetic field tracking error with the inclined scenario.

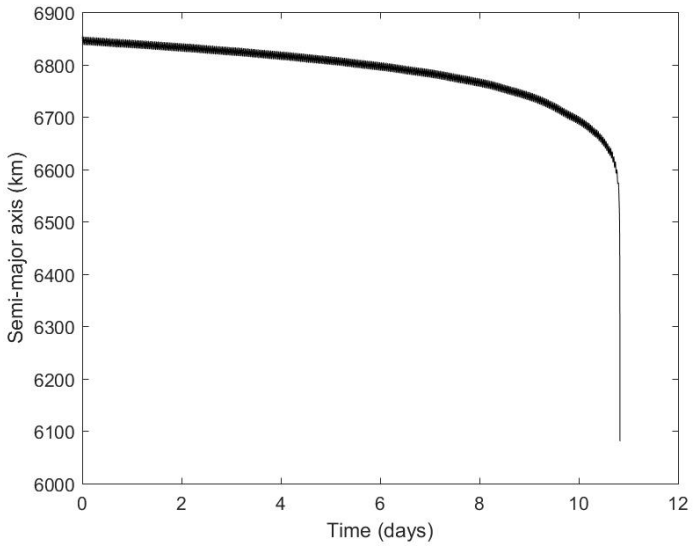

Figure 6.13: Semi-major axis evolution with the geomagnetic field tracker inclined scenario.

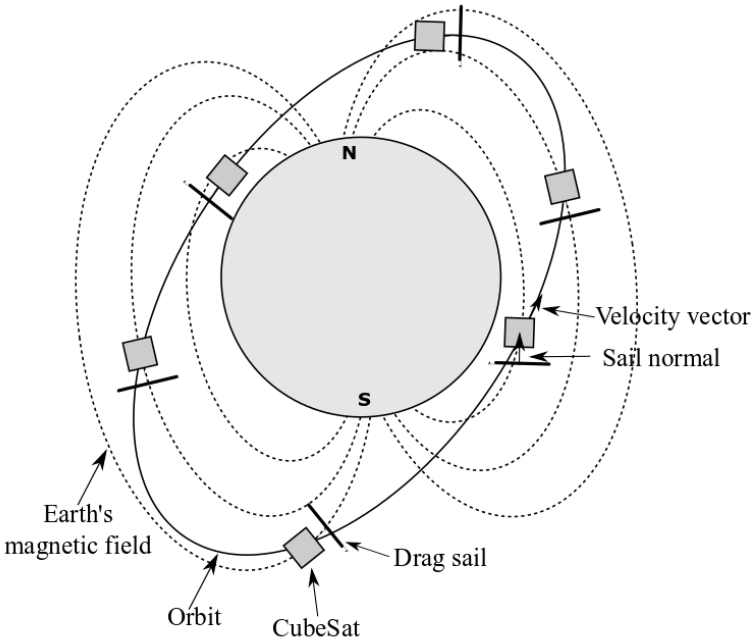

Figure 6.14: Drag sail in an inclined orbit.

in the inclined orbit case. Contrary to the polar orbit, the normal of the drag sail is not necessarily aligned with the velocity vector during most of the orbit. Because of this, the drag generated by the sail is not the maximum possible.

6.4 Spin-Stabilization

The spin-stabilization controller introduced in Chapter 5 is also applied to the drag sail scenario, in order to explore possible improvements in deorbiting times. It is worth reminding that this controller only makes the satellite spin around one of its axes, however it can't control its final orientation. Because of this, the deorbit time will be slightly different from one simulation to another. In this chapter one simulation with characteristic results is presented. This fact also makes the inclination of the orbit to have little effect in the deorbiting times, however it must be recalled that the attitude controllers are magnetorquers, and they perform better at higher inclinations.

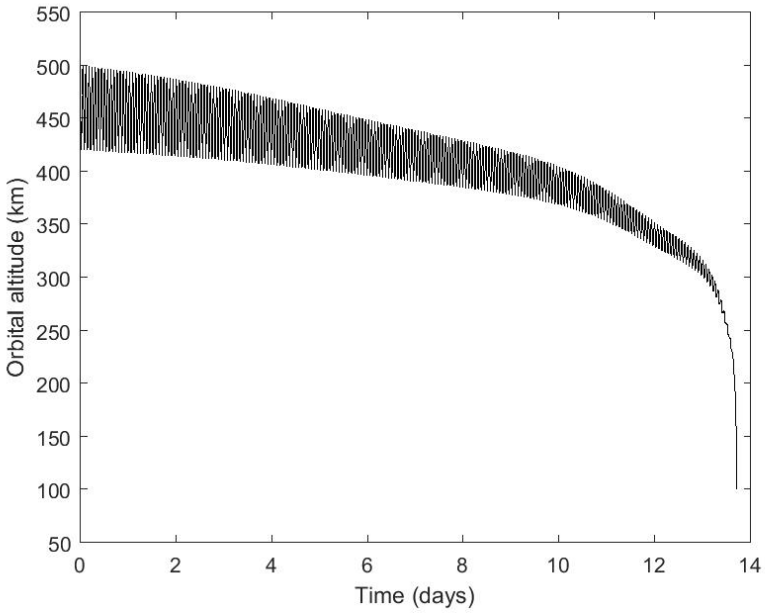

Figure 6.15: Altitude evolution with the spin-stabilized scenario.

The orbital altitude is presented in Fig. 6.15, where it can be seen that the CubeSat is deorbited in a little less than 14 days. In this scenario the performance is slightly poorer than in the tumbling sail case.

The magnetic dipole evolution is shown in Fig. 6.16. It shows the application of the control dipoles during 10 hours, before they are turned off. This period of time was determined after executing some trial simulations, and observing that this time was enough to make the satellite spin at the desired rate.

Figure 6.17 shows how the controller is able to maintain the desired angular rates during practically the whole deorbiting process. So even though the deorbiting time is not necessarily improved by this scheme, the controller achieves its objective. This approach might be subject to further work in order to find out ways to improve its efficiency.

The semi-major axis evolution is presented in Fig. 6.18, whereas the magnetorquer energy consumption is shown in Fig. 6.19, where it can be seen that this consumption is around 0.018 kWh. This is a very low consumption and solar panels are expected to be able to fulfil this energy demand.

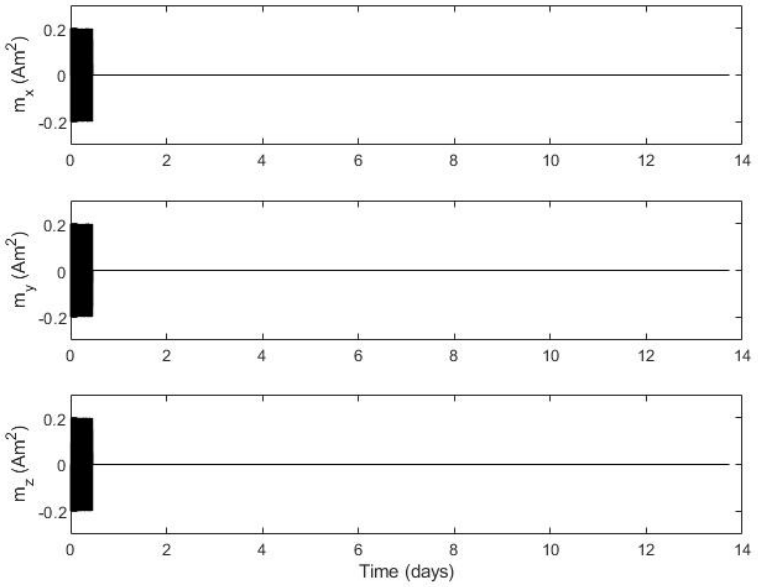

Figure 6.16: Magnetic dipole evolution with the spin-stabilized scenario.

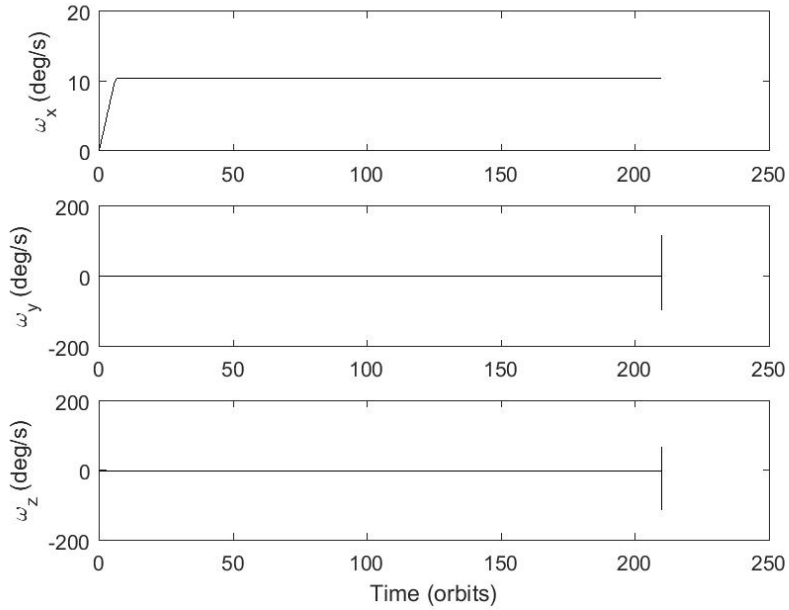

Figure 6.17: Angular velocities evolution with the spin-stabilized scenario.

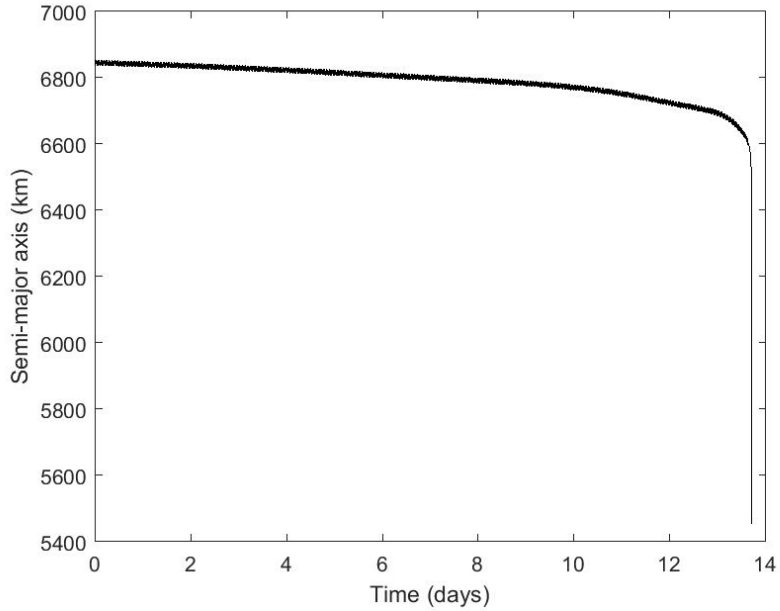

Figure 6.18: Semi-major axis evolution with the spin-stabilized scenario.

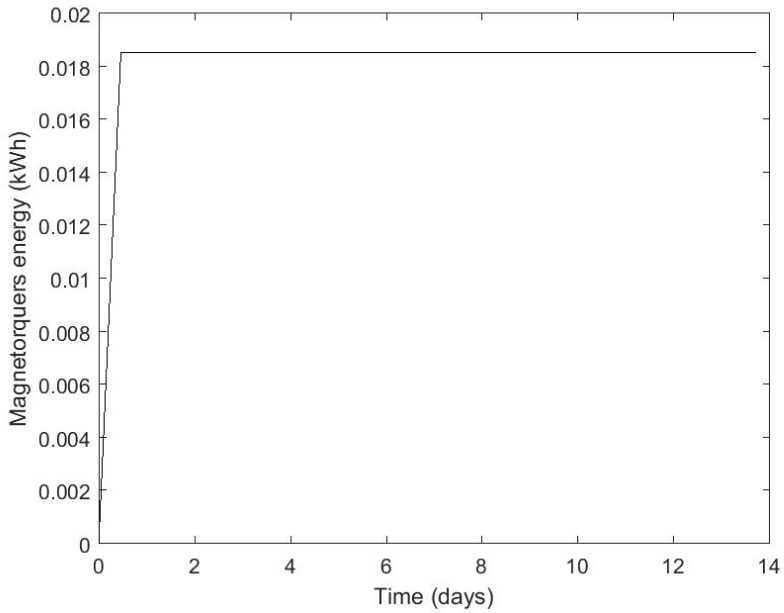

Figure 6.19: Magnetorquer energy consumption with the spin-stabilized scenario.

The spin-stabilization controller proves to be effective in stabilizing the drag sail, however, not much improvement is observed in terms of deorbiting times. Specifically, it is seen to be surpassed in performance by the geomagnetic tracker approach in a polar orbit. Still, one advantage of the spinning approach over the latter is that it has less attitude determination requirements, since it doesn't require gyroscopes. This fact can simplify the overall design of the CubeSat and represent savings in mass and energy budgets, and consequently bring down the mission costs. Furthermore, if further work is successful in controlling the final spinning attitude, and align it with the orbital plane, this approach has the potential of matching the performance of the geomagnetic tracking case, even for orbits that are not polar, hence the relevance of this case of study.

6.5 Robustness Analysis

Similarly to the previous chapters, Monte Carlo simulations were executed in order to test the robustness of the deorbiting algorithms, in this case, with the drag sail scenario. The uncertainty vector Δ is defined in table 4.2, where all of the relevant parameters are varied within realistic ranges. A total of 1000 simulations are executed for every scenario, i.e., the geomagnetic tracker and the gyroless spinning controllers. The results of these simulations are shown in figures 6.20 and 6.21.

As shown in figure 6.20, the geomagnetic field tracking algorithm is effective 100% of the time, and the deorbiting times vary from 7 to 13 days. This is an excellent result, as it proves the algorithm is robust against model uncertainties. It can be concluded that the geomagnetic tracking algorithm in conjunction with drag sails, delivers excellent results in terms of deorbiting times. As explained before, the performance of this method decreases with reduction of inclination.

Figure 6.21 depicts the results of the Monte Carlo simulations in the case of the gyroless spin-stabilization controller with drag sail. It can be seen that the deorbiting times ranges are considerable longer when compared to the results presented in 6.20. These deorbiting times vary from around 10 to close to 30 days. Robustness is still proven and this is also a good improvement over the natural orbital decay case.

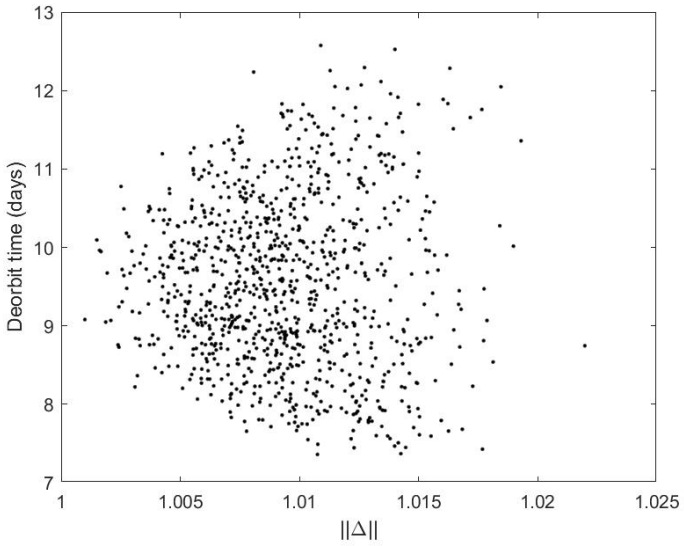

Figure 6.20: Robustness analysis through Monte Carlo simulations, field tracking case.

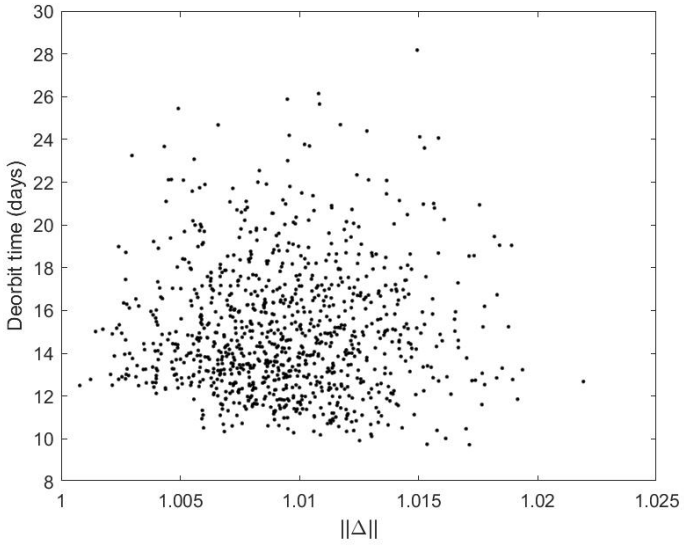

Figure 6.21: Robustness analysis through Monte Carlo simulations, spinning case.

6.6 Summary and Discussions

In this chapter, the possibility of applying the controllers first described in Chapters 4 and 5 to the drag sail scenario was explored.

Five scenarios are examined: 1) passive deorbit with no sail, 2) tumbling scenario with drag sail, 3) geomagnetic field tracker in polar orbit with sail, 4) geomagnetic field tracker in inclined orbit with sail, and 5) spin-stabilization with sail.

One year of deorbiting simulation was executed for the passive deorbit with no sail, with very little orbital altitude loss. This is consistent with the predictions that a CubeSat in an initial orbit of 500 km or more will take years before passively deorbiting.

In the case of the tumbling scenario with sail, a deorbiting time of roughly 13 days was achieved. This performance served as a benchmark for the rest of the scenarios presented in this chapter.

The best performance was obtained for the geomagnetic field tracker in polar orbit with sail, achieving a deorbiting time of 9 days, which represents an improvement of around 30% with respect to the tumbling case. This is due to the fact that the normal of the sail is more or less aligned with the velocity vector for the vast majority of each orbit, with the exception being over the poles.

The performance of the geomagnetic field tracker in inclined orbit with sail was also better than the benchmark. It deorbited the CubeSat in roughly 11 days, which represents an improvement of around 15% in deorbiting time with respect to the tumbling case. This scenario is less effective than the one in the polar orbit since the sail's normal is not aligned with the direction of travel during each orbit.

The spin-stabilization controller was applied to the sail scenario. The deorbiting time was of almost 14 days. Although this time may moderately vary between simulations, it shows the fact that further work is required for this scenario in order to make it more efficient. The main disadvantage at the moment is that there is no control over the final orientation of the CubeSat, which means the sail's normal is oriented randomly, and therefore doesn't generate drag optimally. Finally, proof of the robustness of the algorithms with drag sails is given through Monte Carlo simulations.

Chapter 7

Conclusions and Future Work

7.1 Conclusions

The purpose of this thesis is to explore new solutions that can be applied to the CubeSat deorbiting problem. This topic is particularly challenging due to the common hardware limitations that these nanosatellites face.

In Chapter 2, a literature review is given, where current approaches, whether conceptual or already flown in space are discussed. Three main approaches are discussed in this literature review: deorbit sails, inflatables, and electric tethers. It is shown that these approaches face a series of drawbacks inherent to their designs. Also, the deorbit times that they can offer are still in the orders of years, depending in the initial orbital altitude.

Recent developments in electric propulsion is then introduced as an alternative, having a series of advantages over the previously mentioned approaches. Although there are several variants for electric propulsion technologies, focus is given to five of them, due to their potential in the CubeSat field. They are: Electrospray, Micro Pulsed Plasma Thruster, Hall Effect Thruster, CubeSat Ambipolar Thruster, and Micro Cathode Arc Thruster. Principles of operation of each technology are provided in the literature review. In the past few years, a great deal of literature regarding electric propulsion has been published. While CubeSat deorbiting is recurrently suggested as one its applications, little or no literature is available on methods to enable this objective. This thesis is an effort to fill this gap in

literature.

In Chapter 3, a mathematical background is presented. Equations of orbital motion are given, as well as the satellite's kinematics and dynamics. Different attitude notations are discussed, such as Euler angles, Direct Cosine Matrix, as well as quaternions. Finally, environmental factors such as geomagnetic field and atmospheric models are discussed.

In Chapter 4, a geomagnetic field tracking algorithm is derived. Its principle of operation is as follows. It aligns the thruster carrying axis of the CubeSat with the local magnetic field vector as the satellite orbits the Earth. The measurements of the magnetic field vector are only available in the body frame and no full attitude information is available. If the CubeSat is provided with a model of the Earth's magnetic field, in combination with knowledge of its orbital position, the magnetic field vector can be obtained in LVLH frame. There is a relationship between the orbital velocity vector and the x unit vector of the LVLH frame. Because of this relationship, it can be determined when to activate the thrusters, as well as when to turn them off. In this manner, propulsion will be applied to the CubeSat during half of each orbit, eventually causing it to re-enter Earth's atmosphere.

The control magnetic dipole consists of both a proportional component as well as a derivative one. The proportional term causes the satellite to align the required axis with the magnetic field vector, while the derivative term introduces a damping effect.

A deorbiting mission scenario is designed in order to test the effectiveness of the algorithm. A 3U CubeSat is considered, with realistic physical parameters, and taking into account disturbances such as atmospheric drag and J_2 term effects. The results prove the algorithm not only is effective, but is superior in terms of deorbiting time compared to those attainable with drag sails, inflatables, and electric tethers.

Energy consumption analysis is executed in order to assess the feasibility of the implementation of this algorithm in real life missions. It is observed that the levels of energy used are within the budget commonly available in CubeSats.

Another very important aspect to look at is the stability of the controller. This analysis was done through the application of Floquet theory, proving the stability

of the system for a wide range of angular velocities around the axis aligned with the magnetic field.

Finally, a robustness analysis was executed by means of Monte Carlo simulations, in order to test the tolerance of the controller against model uncertainties. A vector of uncertainties was defined, including aspects such as physical parameters of the CubeSat, and initial conditions such as orbital parameters and angular velocities. One thousand simulations were executed, and the algorithm is always successful in deorbiting the satellite, proving the robustness of the controller.

Because of all of these factors, it is concluded that this algorithm is a good option to be applied to the CubeSat deorbiting problem.

A second algorithm for CubeSat deorbiting is introduced in Chapter 5. This time the deorbiting operation is divided in two phases: 1) gyroless spin-stabilization and, 2) orbit sampling and deorbiting. The spin-stabilization phase has the objective of fixing the thrusting carrying axis of the satellite, which is a precondition for the orbit sampling phase to work. Together, they provide a practical way for CubeSat deorbiting with minimum sensing and actuator capabilities.

The spin-stabilization algorithm is inspired in the B-dot controller, and inherits its ease of implementation. It doesn't require angular velocities readings as an input, therefore, gyroscopes are not necessary. This is the main advantage in comparison with other spin-up algorithms. Just as the geomagnetic tracking algorithm, this approach also uses only magnetometers and magnetorquers as sensors and actuators. Since these two components can't be activated at the same time, a duty cycle has to be implemented. This, and the fact that the magnetorquers cannot generate torques in arbitrary directions, causes the final angular velocity to slightly differ from the desired angular velocity vector. However, the attained accuracy is good enough to proceed with the orbital sampling.

Once the CubeSat has been successfully spin-stabilized, it is necessary to find the portion of the orbit where the thrusters must be activated in order accelerate the orbital decay process. This is not a trivial task in the realistic scenario where there is no attitude information available. An algorithm is described, that only takes the semi-major axis and true anomaly as inputs, which can be obtained from GPS readings. It makes periodic firings of the thrusters until it finds a portion of the orbit where thrusting causes the CubeSat to be de-orbited. The orbital

portion may not be the optimal, but it is demonstrated through simulations that it is always enough in order to successfully deorbit the satellite.

Just as it was done in Chapter 4, a deorbit scenario was designed in order to demonstrate the effectiveness of this two phased deorbiting algorithm. Realistic CubeSat physical features and orbital parameters are defined. The numerical simulations were then executed in a Matlab/Simulink model, which confirmed the effectiveness and efficiency of this algorithm.

The two main variables that affect the deorbit times in this case, are 1) the convergence of the sampling algorithm to the optimal orbital portion, and 2) the orientation of the spinning axis with respect to the orbital plane. The more the spinning axis lays in the orbital plane, the more efficiently thrust is used and shorter deorbiting times are achieved. Energy consumption analysis is also performed, with positive results, as in the case of those in Chapter 4.

For the stability analysis, in this case the Lasalle's invariance principle is used. Robustness analysis is executed also by means of Monte Carlo simulations, proving the system robust to system uncertainties, and showing deorbiting times between 5 and 35 days.

The attitude controllers developed for their application with electric thrusters, are conveniently flexible, such that they can be applied to other actuators. Drag sails are often proposed as methods of deorbiting, but literature on how to stabilize them in orbit is scarce. The attitude control algorithms presented in Chapters 4 and 5 are then applied to the drag sail scenario in Chapter 6.

In order to test their effectiveness of this approach, five scenarios are simulated: 1) natural orbital decay, 2) tumbling case, 3) geomagnetic field tracker in polar orbit, 4) geomagnetic field tracker inclined orbit and 5) spin-stabilization.

It is observed that in the natural orbital decay scenario it would take years for the CubeSat to be deorbited. In the tumbling case, a drag sail of 5 m^2 is added to the model, and as a result the deorbiting time is drastically reduced to a few days. Then, the effectiveness of the geomagnetic field tracking algorithm with drag sail is tested. As expected, the best efficiency of the system is reached in polar orbits, since in this case, the normal of the sail is aligned with the direction of travel during the major part of the orbit, which is not the case for orbits with less inclination.

Finally, the effectiveness of the spin-stabilization algorithm is tested. In this case it can be seen that there are no significant improvement in comparison with the thumbling case. This comes from the fact that the final attitude of the sail is random, therefore, it doesn't even matter the inclination of the orbit.

Since the stability, and the consumption energy of the attitude control algorithms were already discussed in previous chapters, the only thing left was to perform the robustness analysis through Monte Carlo simulations. The analysis shows that the algorithms in conjunction with the drag sail are also robust against model uncertainties.

All the results presented in this thesis were obtained from simulations based in highly accurate numerical models, and such results are very promising. Of course, the performance of the described algorithms has yet to be proved in a real life mission. This mission was out of the scope of this project. Factors that would be faced in a real life mission and were not accounted for in these models include: solar radiation pressure, gravitational pulls from the Moon, the Sun, and other planets, mainly Jupiter, as well as the albedo effect. As it was discussed in Chapter 3, in Low Earth Orbit environment, all these forces are orders of magnitude smaller than the atmospheric drag and the J_2 term, which are accounted for in the models. Therefore, it is not expected that these forces would have a major impact in the performance of the deorbiting systems. Finally, a set of assumptions are made as follows. Even though the energy consumption analysis is provided and it is in good agreement with current CubeSat capabilities, it is assumed that the on board batteries can provide enough energy during eclipse. It is also assumed that solar panels, as well as magnetorquers, magnetometers, gyroscopes - if required - and propulsion engines, function without anomalies. In Chapters 4 and 5 it is assumed that there is enough fuel on board for the entire deorbiting operation. In the case of Chapter 6, it is assumed that the drag sail is successfully deployed.

The deorbiting approaches presented and discussed in this thesis, are aimed to contribute to the efforts of space debris mitigation. The last is already a major concern within the scientific community and must be addressed in a promptly and efficient manner. This work also recognizes the great potential that CubeSat have and the role they are going to play in the future of space exploration. Therefore,

it looks for ways to enable their use in a sustainable way, trying to minimize the impact they have in the space junk problem.

7.2 Future Work

The following are aspects that can be further improved or studied, in order to complement and extend the work presented in this thesis.

While atmospheric drag was considered in all the numerical simulations, the effects of atmospheric torques was not introduced in the models of Chapters 4 and 5. Although it is not expected that atmospheric torques could affect in a major degree the effectiveness of the algorithms, it would be interesting to include this perturbation in the models in order to execute more realistic scenarios, which would allow to further study their robustness.

The gains for the controllers are tuned in a trial-and-error fashion. No optimal tuning formula or procedure was obtained. This requires the execution of multiple simulations, which is time consuming. It would be ideal to have available a more formal procedure, such that the design times can be decreased, and optimal performances guaranteed.

While effective, the control approaches presented in this thesis are not optimal in terms of either deorbiting times, nor energy or fuel consumption. These are aspects in which the presented algorithms can be improved. Because of the constraints in energy and fuel budgets, these two aspects could be prioritized over the deorbiting times, which are already in very acceptable ranges.

In the case of the orbit sampling algorithm present in Chapter 5, there is no control over the final spinning axis orientation. This is a disadvantage. The ideal scenario is for this axis to be aligned with the orbital plane, in which case most of the thrust would be used to effectively decrease the orbit. If the axis is not in the orbital plane, some of the thrust is wasted in changes of orbital inclination. In the most extreme case, the spinning axis could be perpendicular to the orbital plane. In such case all thrust would be wasted, and the deorbit operation wouldn't be possible. This is a very unlikely scenario, however, it would be interesting to look for ways to overcome this disadvantage. This same limitation is inherited by the drag sail scenario presented in Chapter 6.

Electric thrusters were studied and considered for the simulations in Chapters 4 and 5. However, the algorithms proposed are quite flexible, such that their effectiveness with other type of propulsion can be further studied.

As presented in the results of Chapter 5, the efficiency of the orbital sampling algorithm can vary during the deorbiting process. It would be ideal to explore ways in which this efficiency can be maintained above certain threshold during the whole operation. If this can be achieved, it would further reduce the deorbiting times that can be achieved.

The ultimate goal of this research work would be to have it implemented and tested in a CubeSat in a real life mission. More conclusions and further improvements could be developed if this milestone can be achieved in the future.

References

Adeli, S.N. & Lappas, V. (2010). Deployment System for the CubeSail nano-Solar Sail Mission 2 The CubeSail Mission. In *Small Satellite Conference*, Logan, Utah. 11, 121

Andrews, J., Watry, K. & Brown, K. (2011). Nanosat deorbit and recovery system to enable new missions. *25th Annual AIAA/USU Conference on Small Satellites*. xi, 14, 15

Avanzini, G. & Giulietti, F. (2012). Magnetic detumbling of a rigid spacecraft. *Journal of Guidance, Control, and Dynamics*, **35**. 98

Barbashin, E.A. & Krasovskii, N.N. (1952). On Global Stability of Motion. *Doklady Akademii Nauk SSSR*, 453–456. 40

Bering, E.A., Pinsky, L.S., Li, L., Jackson, D. & Chen, J. (2016). MarsCAT : Mars Array of ionospheric Research Satellites using the CubeSat Ambipolar Thruster. In *54th AIAA Aerospace Sciences Meeting*, 1–23. 26

Biddy, C. & Svitek, T. (2012). LightSail-1 Solar Sail Design and Qualification. In *Proceedings of the 41st Aerospace Mechanisms Symposium*, 451–463, Pasadena, California. 13, 121

Blandino, J.J., Martinez, N., Demetriou, M.A. & Gatsonis, N.A. (2016). Feasibility for Orbital Life Extension of a CubeSat Flying in the Lower Thermosphere. 1–18. 20

Carandente, V. & Savino, R. (2014). New concepts of deployable de-orbit and re-entry systems for cubesat miniaturized satellites. *Recent Patents on Engineering*, **8**, 2–12. 14

Chen, S. (2011). The space debris problem. *Asian Perspective*, **35**, 537–558. 9

Chen, T. & Qiu, L. (1997). Linear periodically time-varying discrete-time systems: Aliasing and LTI approximations. *Systems and Control Letters*, **30**, 225–235. 41

Chen, X. (2006). Decomposition and Noncausal Realization of Unstable LPTV System. In *International Conference on Control, Automation, Robotics and Vision*. 41

Cheon, Y.J., Lee, S.H. & Kim, J.H. (2010). Fully magnetic devices-based control for gyroless target pointing of a spinning spacecraft. *IEEE Transactions on Aerospace and Electronic Systems*, **46**, 1484–1491. 91

Chetaev, N.G. (1961). *The Stability of Motion*. Pergamon Press, Oxford-New York-Paris. 40

Clark, J.P., DeBra, D., Dobrotin, B.M., Fischell, E.R., Fleig, A.J., Fosht, D.C., Gatlin, J.A., Perkel, H., Roberson, R.E., Sabroff, A.E., Scott, E.D., Tinling, B.E. & Wheeler, P.C. (1971). Spacecraft Aerodynamic Torques. 124

Coletti, M., Guarducci, F. & Gabriel, S.B. (2011). A micro PPT for Cubesat application : Design and preliminary experimental results. *Acta Astronautica*, **69**, 200–208. xi, 18, 22

Collard, T.A. & Sheehan, J.P. (2016). Preliminary Measurements of an Integrated Prototype of the CubeSat Ambipolar Thruster. 1–11. 18, 25

Comte de Buffon, G. (1777). *Essai d'arithmetique morale*. Supplement a l'Histoire Naturelle, Paris. 40

Cortiella, A., Vidal, D., Jané, J., Juan, E., Olivé, R., Amézaga, A., Munoz, J.F., Carreno-Luengo, P.V.H. & Camps, A. (2016). 3CAT-2: Attitude determination and control system for a GNSS-R earth observation 6U cubesat mission. *European Journal of Remote Sensing*, **49**, 759–776. 93

Cosmo, M.L. & Lorenzini, E.C. (1997). *Tethers in Space Handbook*. 3rd edn. 15

Courant, R., Friedrichs, K.O. & Lewy, H. (1928). *On the partial difference equations of mathematical physics*. Mathematische Annalen. 40

Courtney, D., Dandavino, S., Shea, H., Courtney, D.G., Dandavino, S. & Shea, H. (2015a). Comparing Direct and Indirect Thrust Measurements from Passively Fed and Highly Ionic Electrospray Thrusters. 22

Courtney, D.G., Dandavino, S. & Shea, H. (2015b). Performance and Applications of Ionic Electrospray Micro-Propulsion Prototypes. 1–10. 20

Dandavino, S., Ataman, C., Ryan, C., Chakraborty, S., Courtne, D., Stark, J. & Shea, H. (2014). Microfabricated electrospray emitter arrays with integrated extractor and accelerator electrodes for the propulsion of small spacecraft. *Journal of Micromechanics and Microengineering*. 20

Dankanich, J.W., Polzin, K.A., Calvert, D., Kamhawi, H., Introduction, I., Manager, P., Development, T., Engineer, L.S., Systems, F., Division, E. & Branch, P. (2013). The iodine satellite (iSAT) Hall thruster demonstration mission concept and development. 1–13. 18

David, L. (2017). Sweating the small stuff: CubeSats swarm Earth orbit. 8

Davis, J. & Tech, V. (2004). Mathematical modeling of Earth's magnetic field. 56

Donkster, M.C. & Kac, M. (1950). The Monte Carlo method and its applications. In *Seminar on Scientific Computation*, 74–81, International Business Machines Corporation, New York. 41

Forward, R.L., Hoyt, R.P. & Uphoff, C. (1998). Application of the Terminator Tether Electrodynamic Drag Technology to the Deorbit of Constellation Spacecraft. *American Institute of Aeronautics and Astronautics*. 15

Gandhi, R. & Mitra, S.K. (1997). ALIASING CANCELATION IN BLOCK FILTERS AND PERIODICALLY TIME VARYING SYSTEMS: A TIME-DOMAIN APPROACH. In *IEEE International Symposium on Circuits and Systems*, 2, 2421–2424, Hong Kong. 41

Hagiwara, T. & Umeda, H. (2007). Robust Stability Analysis of Sampled-Data Systems with Noncausal Periodically Time-Varying Scaling : Optimization of Scaling via Approximate Discretization and Error Bound Analysis I . Introduction II . Review on the Robust Stability Anal- ysis with Nonca. 450–457. 41

Hahn, W. (1963). *Theory and Application of Liapunov's Direct Method*. Prentice-Hall, Englewood Cliffs, NJ. 40

Harkness, P., McRobb, M., Lützkendorf, P., Milligan, R., Feeney, A. & Clark, C. (2014). Development status of AEOLDOS - A deorbit module for small satellites. *Advances in Space Research*. 11, 121

Hodges, R.E., Hoppe, D.J., Radway, M.J. & Chahat, N.E. (2015). Novel deployable reflectarray antennas for CubeSat communications. *2015 IEEE MTT-S International Microwave Symposium, IMS 2015*, 4–7. 7

Hodges, R.E., Chahat, N.E., Hoppe, D.J. & Vacchione, J.D. (2016). The Mars Cube One Deployable High Gain Antenna.pdf. In *2016 IEEE International Symposium on Antennas and Propagation (APSURSI)*. 8

Householder, A.S., Forsythe, G.E. & Germond, H.H. (1951). Monte Carlo Methods. *National Bureau of Standards Applied Mathematics Series*, **12**. 41

Hoyt, R.P., Barnes, I.M., Voronka, N.R. & Slostad, J.T. (2009). The Terminator Tape™: A Cost-Effective De-Orbit module for End-of-Life Disposal of LEO Satellites. In *AIAA Space 2009 Conference and Exposition*, Pasadena, California. xi, 15, 16

Jan, Y.W. & Tsai, J.R. (2005). Active control for initial attitude acquisition using magnetic torquers. *Acta Astronautica*, **57**, 754–759. 61

Janhunen, P. (2014). Simulation study of the plasma-brake effect. *Annales Geophysicae*, 1207–1216. 17

Johnson, L., Whorton, M., Heaton, A., Pinson, R., Laue, G. & Adams, C. (2011). NanoSail-D : A solar sail demonstration mission. *Acta Astronautica*, **68**, 571–575. 11

Junkins, J.L. & Schaub, H. (2001). *Analytical Mechanics of Aerospace Systems*. AIAA Education Series, Reston, VA, 2nd edn. xii, xiii, 50, 51, 52, 53, 58, 99

Kahn, H. (1950). Modifications of the Monte Carlo method. In *Seminar on Scientific Computation*, 20–27, International Business Machines Corporation, New York. 41

Keidar, M. (2016). Micro - Cathode Arc Thruster for Small Satellite Propulsion. In *2016 IEEE Aerospace Conference*, Big Sky, Montana. xii, 18, 28, 29, 69

Kelvin, L. (1901). Nineteenth century clouds over the dynamical theory of heat and light. *Philosophical Magazine.*. 40

Kessler, D.J. & Cour-Palais, B.G. (1978). Collision frequency of artificial satellites: The creation of a debris belt. *Journal of Geophysical Research*. 10

Khalil, H.K. (1996). *Nonlinear Systems*. Prentice-Hall, New Jersey, 3rd edn. 40, 62, 89, 113

Khurshid, O., Tikka, T., Praks, J. & Hallikainen, M. (2014). Accommodating the plasma brake experiment on-board the Aalto-1 satellite. *Proceedings of the Estonian Academy of Sciences*. 17

Kim, J., Bates, D.G. & Postlethwaite, I. (2006). Robustness analysis of linear periodic time-varying systems subject to structured uncertainty. *Systems and Control Letters*, **55**, 719–725. 41, 89, 92

Klinkrad, H. (2004). The ESA Space Debris Mitigation Handbook 2002. *Advances in Space Research*, **34**, 1251–1259. 9

Kokotovic, P.V., Khalil, H.K. & O'Reilly, J. (1984). *Singular Perturbation Methods in Control: Analysis and Design*. Academic Press. 92

Kolosa, D., Spangelo, S., Lemmer, K. & Hudson, J. (2014). Mission Analysis for a Micro RF Ion Thruster for CubeSat Orbital Maneuvers. 1–24. 20

Kramer, H.J. (2019). Planet - Flock Imaging Constellation. 8

Krejci, D. & Lozano, P. (2018). Space Propulsion Technology for Small Spacecraft. In *Proceedings of the IEEE*, vol. 106. xi, 23, 24, 25

Krejci, D., Seifert, B. & Scharlemann, C. (2013). Endurance testing of a pulsed plasma thruster for nanosatellites. *Acta Astronautica*, **91**, 187–193. xi, 22, 23

Krejci, D., Mier-hicks, F., Fucetola, C., Lozano, P., Schouten, A.H. & Martel, F. (2015). Design and characterization of a scalable ion electrospray propulsion system. In *30th International Symposium on Space Technology and Science*, 1–11, Hyogo-Kobe, Japan. xi, 21

Lagrange, J.L. (1788). *Mecanique Analytique*. Chez la Veuve Desaint, Paris. 40

Lanoix, E.L. (1999). *A Mathematical Model for the Long-Term Dynamics of Tethered Spacecraft*. Ph.D. thesis, McGill University. 17

Lanoix, E.L.M., Misra, A.K., Modi, V.J. & Tyc, G. (2005). Effect of electromagnetic forces on the orbital dynamics of tethered satellites. *Advances in the Astronautical Sciences*, 1309–1315. 15, 17

Laplace, M. (1886). *Theorie analytiue des probabilites, livre 2, Oeuvres Compleetes de Laplace, Vol 7*. Paris. 40

Lasalle, J.P. (1968). Stability Theory for Ordinary Differential Equations. **65**, 57–65. 40

Lasalle, J.P. & Lefschetz, S. (1962). *Stability by Liapunovs's Direct Method and Applications*. Mathematics in Science and Engineering, New York. 40

Lokcu, E. & Ash, R.L. (2011). A de-orbit system design for CubeSat payloads. In *RAST 2011 - Proceedings of 5th International Conference on Recent Advances in Space Technologies*, Istanbul. 14

Lozano, P. & Martínez-sánchez, M. (2005). Ionic liquid ion sources : characterization of externally wetted emitters. *Journal of Colloid and Interface Science*, **282**, 415–421. 18

Lozano, P.C., Wardle, B.L. & Moloney, P. (2015). Nanoengineered thrusters for the next giant leap in space exploration. *MRS Bulletin*, **40**, 842–849. 19

Lyapunov, A.M. (1892). *The General Problem of the Stability of Motion*. Kharkov, Ukraine. 40

Maessen, D., van Breukelen, E., Zandbergen, B. & Bergsma, O. (2007). Development of a generic inflatable de-orbit device for CubeSats. In *Proceedings of the 58th International Astronnautical Congress*, Hyderabad, India. 13, 93

Maxwell, J.C. (1868). On Governors. *Proceedings of the Royal Society of London*, **16**, 270–283. 40

Meerkov, S.M. (1980). Principle of Vibrational Control Theory and Applications. *IEEE Transactions on Automatic Control*, **25**, 755–762. 92

Messier, D. (2017). SpaceX wants to launch 12,000 satellites. 8, 9

Metropolis, N. & Ulam, S. (1949). The Monte Carlo Method. *Journal of the American Statistical Association*, **44**, 335–341. 41

Metropolis, N., Rosenbluth, A.W., Rosenbluth, M.N. & Teller, A.H. (1953). Equation of State Calculations by Fast Computing Machines. *The Journal of Chemical Physics*. 41

Mier-hicks, F. & Lozano, P.C. (2017). Electrospray Thrusters as Precise Attitude Control Actuators for Small Satellites. *Journal of Guidance, Control, and Dynamics*, **40**, 642–649. xi, 19, 20

Morales, J.E., Kim, J. & Richardson, R.R. (2019). Geomagnetic field tracker for deorbiting a CubeSat using electric thrusters. *Journal of Guidance, Control, and Dynamics*. 94

Nakasuka, S., Senda, K., Watanabe, A., Yajima, T. & Sahara, H. (2009). Simple and small de-orbiting package for nano-satellites using an inflatable balloon. In *Trans. JSASS Space Tech. Japan*. 14

NASA (1976). U.S Standard Atmosphere, 1976. Tech. rep., NASA, Washington, D.C. 58, 60

NASA (2009). The Threat of Orbital Debris and Protecting NASA Space Assets from Satellite Collisions. 69

Nascetti, A., Pittella, E., Teofilatto, P. & Pisa, S. (2015). High-gain S-band patch antenna system for Earth-observation CubeSat satellites. *IEEE Antennas and Wireless Propagation Letters*, **14**, 434–437. 7

Neilsen, T., Weston, C., Fish, C., Bingham, B., Neilsen, T.., Weston, C.. & Fish, C.. (2014). Dice: Challenges of Spinning Cubesats. 91

Oltrogge, D.L. & Leveque, K. (2011). An evaluation of CubeSat orbital decay. In *25th Annual AIAA/USU Conference on Small Satellites*. 9, 123

Park, J.P., Park, S.y., Lee, K., Oh, H.J., Choi, K.Y., Song, Y.B., Yim, J.C., Lee, E., Hwang, S.H., Kim, S., Kang, S.J., Kim, M.S., Jin, S., Lee, S.H., Kwon, S.H., Lee, D.S., Cho, W.H., Park, J.H., Yeo, S.W., Seo, J.W., Lee, K.B., Lee, S.h., Yang, J.H., nam Kim, G., Lee, J., Kim, Y.W. & Kim, T.H. (2016). Mission analysis and CubeSat design for CANYVAL-X mission. In *SpaceOps 2016 Conference*, Daejeon, Korea. xi, 7, 8

Poghosyan, A. & Golkar, A. (2017). CubeSat evolution: Analyzing CubeSat capabilities for conducting science missions. *Progress in Aerospace Sciences*, **88**, 59–83. 81

Rajawat, K., Wang, T. & Giannakis, G.B. (2009). AN ALGEBRAIC POLYPHASE APPROACH TO WIRELESS NETWORK CODING. *2009 IEEE International Conference on Acoustics, Speech and Signal Processing*, 2441–2444. 41

Reichenbach, N., Sinn, T., Schimmerohn, M. & Langer, M. (2018). LESSONS LEARNT ON THE DEVELOPMENT OF A DE-ORBIT SUB-SYSTEM FOR THE 12U-CUBESAT ERNST LESSONS LEARNT ON THE DEVELOPMENT OF A DE-ORBIT SUBSYSTEM FOR THE. In *Advanced Lightweight Structures and Reflector Antennas*, October, Tbilisi, Georgia. 12, 121

Sanmartin, J.R., Charro, M., Chen, X., Lorenzini, E.C., Colombatti, G., Zanutto, D., Williams, J.D., Xie, K., Metz, G.E., Carrasco, J.A., Garcia-de quiros, F., Lasa, J. & Marcos, J. (2012). A Universal System To De-Orbit Satellites At End of Life. *The Journal of Space Technology and Science*, 21–32. 15

Sastry, S.S. (1999). *Nonlinear Systems: Analysis, Stability and Control*. Springer-Verlag, New York-Heidelberg-Berlin. 40

Schwartz, S., Asphaug, E. & Thangavelautham, J. (2020). ADVANCING ASTEROID SPACECRAFT GNC TECHNOLOGY USING STUDENT BUILT CUBESAT CENTRIFUGE LABORATORIES. 1–19. 91

Shaw, P.V. (2011). *Pulsed Plasma Thrusters for Small Satellites*. Ph.D. thesis. 23

Sheehan, J.P., Collard, T.A., Ebersohn, F.H. & Longmier, B.W. (2015). Initial operation of the CubeSat ambipolar thruster. In *30th International Symposium on Space Technology and Science*, 1–12, Hyogo-Kobe, Japan. xii, 18, 25, 27, 28, 69

Shuster, M.D. & Oh, S.D. (1981). Three-axis attitude determination from vector observations. *Journal of Guidance, Control, and Dynamics*, **4**, 70–77. 34

Sidi, M.J. (1997). *Spacecraft Dynamics and Control: A Practical Engineering Approach*. Cambridge Univ. Press, New York. 50

Slotine, J.J.E. & Li, W. (1991). *Applied Nonlinear Control*. Prentice-Hall, New Jersey, 3rd edn. 91, 113

Spangelo, S. & Longmier, B.W. (2015). Optimization of CubeSat System-Level Design and Propulsion Systems for Earth-Escape Missions. *Journal of Spacecraft and Rockets*, **52**. xii, 27

Steyn, W.H. & Jordaan, H.W. (2015). An active attitude control system for a drag sail satellite. *Proceedings of the International Astronautical Congress, IAC*, **6**, 4557–4565. 91

Steyn, W.H. & Lappas, V. (2011). Cubesat solar sail 3-axis stabilization using panel translation and magnetic torquing. *Aerospace Science and Technology*, **15**, 476–485. xi, 12, 13, 121, 124

Stickler, A.C. & Alfriend, K.T. (1974). An Elementary Magnetic Attitude Control System. In *Mechanics and Control of Flight Conference*. 65, 99

Stickler, A.C. & Alfriend, K.T. (1976). Elementary magnetic attitude control system. *Journal of Spacecraft and Rockets*, **13**, 282–287. 98

Stohlman, O.R.O., Schenk, M. & Lappas, V. (2014). Development of the Deorbitsail flight model. In *Spacecraft Structures Conference*, National Harbor, Maryland, USA. 11

Stone, W.C. & Witzgall, C. (2006). Evaluation of Aerodynamic Drag and Torque for External Tanks in Low Earth Orbit. *Journal of Research of the National Institute of Standards and Technology*, **111**, 143. 124

Thomson, W. & Tait, P.G. (1867). *Teatrise on Natural Philosophy*. Oxford University, Walton Street, Oxford. 40

Tsuda, Y., Yamaguchi, T., Ikeda, H., Mimasu, Y., Saiki, T., Takeuchi, H. & Nakamiya, M. (2013). 79 JSTS Vol. 27, No. 1. *The Journal of Space Technology and Science*, **27**, 79–89. 13

Tummala, A.R. & Dutta, A. (2017). An Overview of Cube-Satellite Propulsion Technologies and Trends. *Aerospace*, 1–30. 24

Vaidyanathan, P.P. (1988). Polyphase Networks , Block Digital Filtering , LPTV Systems , and Alias-Free QMF Banks : A Unified Approach Based on Pseudocirculants. **36**. 41

Viquerat, A., Schenk, M., Sanders, B. & Lappas, V. (2014). Inflatable rigidisable mast for End-Of-Life deorbiting system. In *European Conference on Spacecraft Structures, Materials and Environmental Testing (SSMET)*, Braunschweig, Germany. 14

Voronka, N.R., Hoyt, R.P., Slostad, J.T., Barnes, I., S, N.C.P., B, S., Klumpar, D. & Solomon, D. (2005). Technology demonstrator of a standardized deorbit module designed for CubeSat and RocketPod applications. In *19th Annual AIAA/USU Conference on Small Satellites*. 17

Walter, U. (2012). *Astronautics: The Physics of Space Flight*. Wiley-VCH, Weinheim, Germany, 2nd edn. xii, xiii, 44, 47, 49, 55, 69

Wenberg, D., Hanlon, E., Keegan, B., Kolbeck, J., Teel, G. & Keidar, M. (2017). BRICSat-D Flight Experiment : Demonstrating the Feasibility of Low Cost Diagnostic Missions. In *AIAA SciTech Forum*, January, 1–14, Grapevine, Texas. xii, 30

Xia, X., Sun, G., Zhang, K., Wu, S., Wang, T., Xia, L. & Liu, S. (2017). Nanosat/Cubesat ADCS Survey. In *29th Chinese Control And Decision Conference*, 5151–5158, IEEE. xii, 33, 34, 35, 36, 37, 38, 39

Yin, W. (2009). *Identification of Linear Periodically Time Varying Systems*. Ph.D. thesis, University of Saskatchewan. 41

Yoo, Y., Kim, S., Suk, J. & Kim, J. (2016). Attitude Control System Design & Verification for CNUSAIL-1 with Solar / Drag Sail. *International Journal of Aerospace and Space Sciences*, **17**, 579–592. 12

Zhang, J., Zhang, C., Norrie, W., Signal, S., Processing, I. & Adelaide, T.P. (1996). Robustness of Discrete Periodically Time Varying Control Under Different Model Perturbations *. 3984–3989. 41

Zhong, R. & Zhu, Z. (2014a). Optimal control of nanosatellite fast deorbit using electrodynamic tether. *Journal of Guidance, Control, and Dynamics*, 1182–1194. 17

Zhong, R. & Zhu, Z.H. (2014b). Optimal current switching control of electrodynamic tethers for fast deorbit. *Journal of Guidance, Control, and Dynamics*, 1501–1511. 17

Zhuang, T., Shashurin, A., Chiu, D., Teel, G. & Washington, A.E. (2011). Micro-cathode arc thruster development and characterization. In *International Electric Propulsion Conference*, vol. 1, 1–7, Wiesbaden, Germany. 18